DTIC FILE COPY

①

AD-A196 402

REPORT DOCUMENTATION PAGE		READ INSTRUCTIONS BEFORE COMPLETING FORM
1. REPORT NUMBER AFIT/CI/NR 88-131	2. GOVT ACCESSION NO.	3. RECIPIENT'S CATALOG NUMBER
4. TITLE (and Subtitle) SYNTHESIS OF RESISTIVE TAPERS TO CONTROL SCATTERING PATTERNS OF STRIPS		5. TYPE OF REPORT & PERIOD COVERED MS THESIS
		6. PERFORMING ORG. REPORT NUMBER
7. AUTHOR(s) RANDY LARRY HAUPT		8. CONTRACT OR GRANT NUMBER(s)
9. PERFORMING ORGANIZATION NAME AND ADDRESS AFIT STUDENT AT: UNIVERSITY OF MICHIGAN		10. PROGRAM ELEMENT, PROJECT, TASK AREA & WORK UNIT NUMBERS
CONTROLLING OFFICE NAME AND ADDRESS		12. REPORT DATE 1988
		13. NUMBER OF PAGES 161
14. MONITORING AGENCY NAME & ADDRESS(if different from Controlling Office) AFIT/NR Wright-Patterson AFB OH 45433-6583		15. SECURITY CLASS. (of this report) UNCLASSIFIED
		15a. DECLASSIFICATION/DOWNGRADING SCHEDULE

16. DISTRIBUTION STATEMENT (of this Report)

DISTRIBUTED UNLIMITED: APPROVED FOR PUBLIC RELEASE

DTIC
ELECTE
S
AUG 0 2 1988
D

17. DISTRIBUTION STATEMENT (of the abstract entered in Block 20, if different from Report)

SAME AS REPORT

18. SUPPLEMENTARY NOTES

Approved for Public Release: IAW AFR 190-1
LYNN E. WOLAVER
Dean for Research and Professional Development
Air Force Institute of Technology
Wright-Patterson AFB OH 45433-6583

19. KEY WORDS (Continue on reverse side if necessary and identify by block number)

20. ABSTRACT (Continue on reverse side if necessary and identify by block number)

ATTACHED

SYNTHESIS OF RESISTIVE TAPERS TO CONTROL SCATTERING PATTERNS OF STRIPS

by
Randy Larry Haupt

A dissertation submitted in partial fulfillment
of the requirements for the degree of
Doctor of Philosophy
(Electrical Engineering)
in The University of Michigan
1987

Doctoral Committee:

Associate Professor Valdis V. Liepa, Chairman
Associate Professor John P. Boyd
Professor Dipak L. Sengupta, University of Detroit
Professor Emeritus Chen-To Tai
Professor Fawwaz T. Ulaby

To my wife Sue and daughter Bonny

ACKNOWLEDGEMENTS

This dissertation represents the pinnacle of my formal education and involves the help of many people. I'd like to thank my friends and colleagues at RADC/EE, Hanscom AFB, MA for their help and support and the use of their bistatic measurement facility. In particular, I'd like to thank Dr. J. Leon Poirrier for his encouragement and help, Marc Cote for his help with the bistatic measurements, and Dr. Arthur Yaghein for reviewing the first half of my thesis. Several of the ideas in this thesis are based on the work of Dr. Robert Mailloux, Dr. Robert Shore, Dr. Hans Steyskal, and Lt. Col. Michael O'Brien. I am truely indebted to my many friends at RADC.

I am grateful to Southwall Technologies for donating the resistive sheets.

All the members of my committee have taken an active part in helping me with my dissertation. I am forever grateful. Prof. Liepa has been particularly understanding and encouraging throughout the past few years. I would also like to thank Prof. Wen-Jei Yang of Mechanical Engineering for his help with the iterative numerical methods, and Prof. Leslie Olsen and Dr. Fay Edwards for their expert editing of parts of the dissertation.

I owe many thanks to my friends Dr. Martin Herman and Leland Pierce for their commiseration and help.

In the past year my father-in-law, Charles Slagle, my high school math teacher, Jeanne Napolitan, and my pastor, Rev Donald Thompson, passed away. Their profound influence on my life will never be forgotten.

Finally, I want to thank my family for their love and patience. My parents; my brother Rick and his family Donna, Ricky, and Brvan; and my wife Sue and daughter Bonny are the greatest source of joy and encouragement in my life. Sue has also been an expert technical consultant on various aspects of my thesis.

TABLE OF CONTENTS

LIST OF FIGURES

Figure

viii

LIST OF TABLES

CHAPTER I

INTRODUCTION

1.1 Motivation

Scattering occurs when an electromagnetic wave impinges on an object and creates currents in that object which reradiate other electromagnetic waves. The electromagnetic wave may be of any frequency, but most of our every day encounters with scattering involve light. As technology advances, however, scattering from the invisible spectrum, particularly microwaves, becomes more and more important. Already words such as microwave dish, radar, and stealth airplane have become part of our everyday vocabulary. Microwaves have invaded our lives by helping us cook, watch television, talk on the telephone, and detect the launch of submarine ballistic missiles. Public concerns involving the impact of microwaves on the environment and health, and military concerns involving very low sidelobe antennas and targets with a low radar cross section (RCS) point to a need for controlling the scattering of electromagnetic waves at microwave frequencies.

Currently, three primary methods exist to reduce microwave scattering from an object: covering it with absorber, changing its shape, and detuning it through impedance loading. Absorbers convert unwanted electromagnetic energy into heat. An example is lining an anechoic chamber with absorbers. Changing its shape channels energy from one direction to another, changes dominant scattering centers, or causes returns from various parts to coherently add and cancel the total return. Examples include rounding sharp edges, making an antenna conformal to the surface of an airplane, and serating the edges of a compact range reflector. Impedance loading alters the resonant frequency of an object. Examples include making a radome transparent to signals in the frequency band of the antenna and detuning

the support wires of a broadcast antenna. Often, a combination of these techniques is necessary to reduce the scattering to an acceptable level. Although many scientific theories are available for analyzing scattering from objects, the process of reducing the scattering is presently as much an art as a science.

Of the three techniques, absorbers have the most attractive features. They have a broad bandwidth, attenuate the return in many directions, and may be used to reduce scattering from an object after the object is designed. In contrast, shaping an object does not reduce the scattering in all directions, may not even be possible once the object is past the design stage, and may not reduce the scattering to desired levels. Impedance loading is inferior because it has a narrow bandwidth, is not usually feasible past the design stage, and is not practical for large reflecting surfaces.

Absorbers have low scattering levels because they convert most of the incident electromagnetic energy into heat and only a small percentage is reflected or transmitted. In the absorber the amount of energy converted into heat (absorbed) depends on the size of the imaginary part of the index of refraction. The higher the imaginary part, the more energy the material absorbs.

An excellent example of absorption occurs in the heating of food in a microwave oven. The incident microwave energy is absorbed by the water molecules in the food, and the food gets hot. Water absorbs the energy, because its permittivity has a large imaginary part at microwave frequencies. Frozen food, however, heats slowly because the permittivity of ice has a small imaginary part at microwave frequencies. [1]

1.2 Problem Statement

Before trying to control scattering from complex shapes, such as an antenna or airplane, one should try to develop methods to control scattering from simple objects. A very simple object is a two dimensional strip. It is infinitely thin, has a finite width, and an infinite length. The scattering pattern of the strip depends upon its width and material composition. Varying these two factors provides a means for controlling the radar cross-section (RCS) of the strip. The goal of this thesis is to synthesize resistive tapers for the strip that produce desired bistatic scattering and backscattering patterns.

---

[1] For a molecular description of how a microwave oven works, see the article by Walker [1987].

1.3 Background

Many references report a variety of techniques for calculating the currents induced in strips by incident plane waves and the corresponding scattered fields. Morse and Feshbach[1953] express the scattered field of a perfectly conducting strip in terms of a Mathieu eigenfunction expansion. A similar eigenfunction expansion is not available for resistive strips, however. Senior[1979a] derives asymptotic expressions for the field scattered by a strip with uniform resistivity. More recently, Richmond[1985] solves for the currents induced in a thin dielectric strip using a Galerkin method. Unlike Senior's approach, this approach numerically solves for the currents in a strip that has a finite thickness. Butler[1985] approaches the problem by expanding the current in the integral equation using Chebychev polynomials as basis functions, then solving the integral analytically.

Controlling the scattering patterns of strips has its roots in earlier studies of impedance loading of objects. Chen and Liepa [1964] showed that a zero broadside return of a cylinder less than two wavelengths long can be achieved by proper choice of a central impedance load. Schindler, et al. [1965] extended this work to longer cylinders. They found that getting zero backscattering from dipoles greater than one half wavelength long or at angles other than broadside requires multiple passive loads. Harrington and Mautz [1972] take one step further by describing a reactive loading synthesis procedure for obtaining a current that produces a far field pattern that is the least mean-square approximation to a desired pattern. Resistive and impedance loading is also important in reducing the scattering from the edges of reflector antennas to get low sidelobes [Bucci and Giorgio, 1980; Yazgan, 1987]. Finally, Ray and Mittra have shown scattering results from conductive strips with resistive loads [1983].

Attempts have been made to alter the scattering patterns of a strip by smoothly varying its resistivity, rather than edge loading. Senior[1979b] discusses the possibility of reducing the backscattering of a resistive strip at edge-on incidence. He states that the return at edge-on incidence gets smaller as the strip's resistivity gets larger. The return approaches zero only when the strip resistivity approaches ∞ . When the strip resistivity equals 1885 Ω/square, the edge-on return from the strip is 26.6dB below the value for a perfectly conducting strip . Senior mentions that the return may be minimized by optimally tapering

the resistivity of the strip from a maximum value at the front edge to perfectly at the rear edge. He does not suggest any possible resistive tapers for controlling scattering from the strip, though. Ray and Mittra[1983] find that a resistive load on the edges of a metallic strip reduces the induced edge currents for E-polarization, but causes current spikes at the junction between the metal and resistive sections of the strip. They suggest eliminating the discontinuity by smoothly tapering the current from a maximum at the metal to a minimum at the highly resistive edges. Senior and Liepa[1984] show that a parabolic taper on a resistive half plane significantly reduces edge scattering. This same principle may be applied to both edges of a strip. Wang and Liepa[1985] use a parabolic resistive taper on the ground plane of a monopole antenna to reduce the effects of the ground plane edge on the antenna pattern. The resulting radiation pattern and antenna impedance approaches those of a monopole above a large ground plane. Haupt and Liepa [1987] describe the physical optics (PO) resistivity synthesis technique presented in Chapter 3.

1.4 Overview

In order to improve upon these previous efforts of "guessing" a resistive taper that will reduce the scattering pattern's sidelobes, this thesis goes a step beyond by developing and experimentally verifying synthesis techniques for specifying the level of the backscattering and bistatic scattering patterns of a strip over a desired angular sector. The specifications include relative sidelobe level, specular level, and nulls at designated locations.

Chapter 2 presents the necessary definitions and mathematical and numerical techniques for analyzing the strip current density and scattering patterns of a strip due to an incident plane wave. The integral and physical optics (PO) equations for the strip current density are derived. Agreement between these two techniques increases as the strip resistivity increases. A large part of the chapter concerns choosing an appropriate numerical method for solving the integral equation approach. For the purposes of this thesis, collocation with pulse basis functions and PLU decomposition and back-substitution combine to give accurate, yet computationally fast results.

Chapter 3 describes how to synthesize a resistive taper that produces a desired strip current density that in turn produces a desired scattering pattern in the far field. The

resistive taper is derived from a given desired current distribution by substituting the desired current distribution into either the integral equation or PO equation and solving for the strip resistivity. Many current distributions have already been developed in antenna theory to get desired far field antenna patterns. One of these current distributions can be substituted for the strip current density in either the integral or PO equation to find the strip resistivity. The strip resistivity derived in this manner does result in the desired bistatic scattering or backscattering pattern. Low sidelobes are demonstrated via the Taylor current distribution and nulling is demonstrated via the Shore-Steyskal null synthesis technique. The low sidelobe resistive taper derived through the integral equation approach has real and imaginary parts, while the resistive taper derived through the PO approach is real. Since PO also produces the desired low sidelobe scattering pattern with excellent accuracy, the PO taper is more desirable. The integral equation approach is needed to produce the proper complex resistive taper for nulling, though.

Chapter 4 describes the four-point probe technique used to measure the resistivity of a sheet. Expressions are derived for calculating the dc voltage and current density on the sheet due to the outer current probes of a four-point probe. These equations are solved numerically using finite elements and Successive Over Relaxation, and the results for a constant resistive sheet are compared with analytical results. Since the analytical results are confined to measuring the resistivity of a constant resistive sheet near the center of the sheet, the numerical approach is used to investigate measuring tapered resistive sheets.

Chapter 5 describes the impact of errors in the resistive taper on the induced strip current density and the scattering patterns. Resistive errors are assumed to be random and/or correlated. These errors give rise to perturbations in the strip current density, which inturn give rise to perturbations in the resulting scattering patterns. Expressions for the current and scattering pattern perturbations are derived. The impact of the errors is described in terms of the average rms error between the error and no-error current and scattering patterns quantities and in terms of sidelobe level deviation between the error and no-error scattering patterns.

Chapter 6 gives the experimental bistatic scattering measurement results on a tapered resistive sheet. The experimental set-up, calibration, and measurement procedures are

described. The experimental results are compared with numerical results and show good agreement for the metal plate and a reasonably good agreement for the tapered sheet. The discrepancies in the low sidelobe scattering measurements are due to a number of sources.

CHAPTER II

CALCULATING THE FIELDS SCATTERED BY RESISTIVE STRIPS

This chapter presents several methods for calculating the strip current density and scattered fields of a resistive strip due to plane wave incidence. These methods may be divided into two approaches: 1) integral equation and 2) Physical Optics (PO). The integral equation approach is the more accurate; however, PO has several attractive features. First, it is simple to calculate compared to the integral equation approach. Second, it gives excellent results for highly resistive or tapered resistive strips. Third, it is a possible seed for iterative methods. Unfortunately, this application proved fruitless in the present study. Fourth, it serves as a synthesis method for low sidelobe real valued resistive tapers as shown in Chapter 3.

A large portion of this chapter concerns the numerical solution of the integral equations. The first step is to convert the integral equations into matrix equations via the method of collocation, then solve the matrix equation for the strip current density. Pulses and Chebychev polynomials are the two types of basis functions used in the collocation technique. Pulses proved faster and more accurate than Chebychev polynomials for the applications in this thesis. Three matrix solving techniques for finding the coefficients of the basis functions are presented: 1) PLU decomposition and back-substitution, which turned out to be the best method for the problems in this thesis; 2) iterative methods including relaxation, secant, and Steffensen's; and 3) conjugate gradient. The advantages and disadvantages of each method are presented.

The final step in the analysis involves calculating the two-dimensional bistatic scattering and backscattering far field patterns.

7

2.1 Derivation of the Scattering Equations for a Resistive Strip

This section derives the field equations for calculating the strip current density induced on a resistive strip by an incident plane wave. Two methods are considered. First, an integral formulation in terms of the current induced on a strip is derived from magnetic vector potentials. This method is the more accurate and traditional approach to the problem. Second, A PO formulation for the current is derived from Geometrical Optics. Although less accurate than the integral equation approach, it serves as a seed for iterative methods, gives very accurate results for resistive strips, and is simple to compute compared to the integral equation approach.

2.1.1 Integral Equation Formulation

In scattering problems, the total electric field is the sum of the incident and scattered electric fields.

$$\overline{E}^i = \overline{E}^T - \overline{E}^s \tag{2.1-1}$$

Superscripts indicate total field (T), incident field (i), and scattered field (s). Each term in (2.1-1) is considered separately in the following pages.

The incident field is a plane wave of either E-polarization [2]

$$\overline{E}^i = \hat{z} E_o e^{jk(x\cos\,\phi_o + y\sin\,\phi_o)} \tag{2.1-2a}$$

$$\overline{H}^i = (-\hat{x}\sin\phi_o + \hat{y}\cos\phi_o) H_o e^{jk(x\cos\,\phi_o + y\sin\,\phi_o)} \tag{2.1-2b}$$

or H-polarization

$$\overline{E}^i = (\hat{x}\sin\phi_o - \hat{y}\cos\phi_o) E_o e^{jk(x\cos\,\phi_o + y\sin\,\phi_o)} \tag{2.1-3a}$$

$$\overline{H}^i = \hat{z} H_o e^{jk(x\cos\,\phi_o + y\sin\,\phi_o)} \tag{2.1-3b}$$

where

---

[2] An $e^{j\omega t}$ time dependence is assumed and suppressed.

ϕ_o = direction of incident plane wave relative to the x-axis

k = wave number = $\omega\sqrt{\mu_o\epsilon_o} = \dfrac{2\pi}{\lambda}$

ω = radial frequency = $2\pi f$

f = frequency of incident wave

λ = wavelength of incident wave

μ_o = permeability of free space

ϵ_o = permittivity of free space

E_o = constant amplitude of incident electric field

H_o = constant amplitude of incident magnetic field

$Z_o = \dfrac{E_o}{H_o} = \sqrt{\dfrac{\mu_o}{\epsilon_o}}$

= characteristic impedance of free space

An E-polarized plane wave has $\overline{E}$ perpendicular to the plane containing the propagation vector and the normal to the interface (the x-y plane). Likewise, an H-polarized plane wave has $\overline{H}$ perpendicular to the x-y plane. Figure 2.1 shows an E-polarized plane wave incident at an angle ϕ_o on a strip of width $2a$, where a is expressed in units of λ.

Within a thin strip the total electric field is related to the total strip current density[3] (J in amps/meter) by [Harrington and Mautz, 1975]

$$E^T_{tangent} = \dfrac{J_s}{[\sigma + j\omega(\epsilon' - \epsilon_o)]\iota} \qquad (2.1\text{-}4)$$

where

---

[3] The strip is assumed to be made of materials that have the same permeability as free space ($\mu = \mu_o$). Otherwise, a magnetic current density term ($\nabla \times \overline{M}$) should be included in the total current.
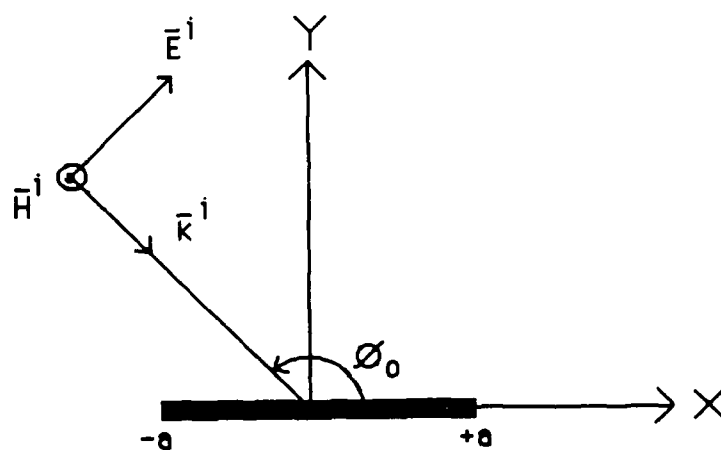
Figure 2.1 — Model of a resistive strip 2a wide with an E-polarized plane wave incident at an angle of ϕ_o

$$\overline{E}^{s} = -j\omega\overline{A} - \nabla\nabla \cdot \overline{A} \qquad (2.1\text{-}8)$$

$$\overline{A} = \mu_{o} \int_{-a}^{a} \overline{J}_{s}(\overline{x}')G(\overline{\rho}/\overline{x}')dx' \qquad (2.1\text{-}9)$$

where

$$\overline{J}_{s} = \begin{cases} J_{x}\widehat{x}, & \text{H-polarization} \\ J_{z}\widehat{z}, & \text{E-polarization} \end{cases}$$

$$\overline{x}' = x'\widehat{x} = \text{direction to source point on strip}$$

$$G(\overline{\rho}/\overline{x}') = \text{Green function} = \frac{1}{4j}H_{o}^{(2)}(k|\overline{\rho} - \overline{x}'|)$$

$$\overline{\rho} = \text{direction to observation point} = x\widehat{x} + y\widehat{y}$$

For E-polarization, $\nabla \cdot A_{z}\widehat{z} = 0$ leaving

$$E^{s} = \frac{-\omega\mu_{o}}{4} \int_{-a}^{a} J_{z}(\overline{x}')H_{o}^{(2)}(k|\overline{\rho} - \overline{x}'|)dx' \qquad (2.1\text{-}10)$$

Now, all the E-polarization components of (2.1-1) have been derived. Assembling (2.1-2), (2.1-5), and (2.1-10) to make (2.1-1) produces

$$H_{o}e^{jkx\cos\phi_{o}} = \eta(x)J_{z}(x) + \frac{k}{4} \int_{-a}^{a} J_{z}(x')H_{o}^{(2)}(k|x - x'|)dx' \qquad (2.1\text{-}11)$$

Turning to H-polarization, the second term in (2.1-8) does not equal 0. Instead,

$$\nabla \cdot A_{z}\widehat{z} = -\frac{1}{4j} \int_{-a}^{a} J_{x}(x')\frac{\partial\rho}{\partial x}H_{1}^{(2)}(k|\rho - x'|)dx' \qquad (2.1\text{-}12)$$

and

$$\nabla\nabla \cdot \overline{A} = \frac{-k^{2}\widehat{x}}{4j} \int J_{x}(x')H_{o}^{(2)}(k|\rho - x'|)dx'$$
$$+ \frac{-k\widehat{x}}{4j} \int J_{x}(x')H_{1}^{(2)}(k|\rho - x'|)\frac{1}{(k|\rho - x'|)}dx' \qquad (2.1\text{-}13)$$

Substituting (2.1-9) and (2.1-13) into (2.1-8) and solving for the scattered field gives

$$\overline{E}^s = \frac{\widehat{x} Z_o}{4} \int_{-a}^{a} J_x(x') \frac{1}{|\rho - x'|} H_1^{(2)}(k|\rho - x'|) dx' \qquad (2.1\text{-}14)$$

Next, substitute the tangential components of (2.1-2), (2.1-5), and (2.1-14) into (2.1-1) to get

$$H_o \sin \phi_o e^{jkx\cos \phi_o} = \eta(x) J_x(x) + \frac{k}{4} \int_{-a}^{a} J_x(x') \frac{1}{k|x - x'|} H_1^{(2)}(k|x - x'|) dx' \qquad (2.1\text{-}15)$$

Equations (2.1-11) and (2.1-15) relate the incident electric field to the induced strip current density. These equations are exact only when $\eta = 0$, since the resistive boundary condition, $E^T = RJ$, is only an approximation.[5] Finding an accurate representation of J depends upon a judicial choice of the numerical solution.

2.1.2 Physical Optics Formulation

Instead of numerically solving (2.1-11) and (2.1-15) for the strip current density, the strip current density may be approximated with a PO formulation. The PO current expressions are derived using geometric optics and relating the total tangential electric field to the strip current density via the strip resistivity. Starting with E-polarization, the reflected fields above the strip are

$$\overline{E}^r = \rho_\tau \widehat{z} E_o e^{jk(x\cos\phi_o - y\sin\phi_o)} \qquad (2.1\text{-}16)$$

$$\overline{H}^r = \rho_\tau (\widehat{x}\sin\phi_o + \widehat{y}\cos\phi_o) H_o e^{jk(x\cos\phi_o - y\sin\phi_o)} \qquad (2.1\text{-}17)$$

and the transmitted fields below the strip are

$$\overline{E}^t = \tau \widehat{z} E_o e^{jk(x\cos\phi_o + y\sin\phi_o)} \qquad (2.1\text{-}18)$$

$$\overline{H}^t = \tau (-\widehat{x}\sin\phi_o + \widehat{y}\cos\phi_o) H_o e^{jk(x\cos\phi_o + y\sin\phi_o)} \qquad (2.1\text{-}19)$$

where the superscripts i, r, and t stand for incident, reflected, and transmitted fields respectively, and ρ_τ and τ are the reflection and transmission coefficients. The incident electric and magnetic fields are given by (2.1-2) and (2.1-3).

---

[5] The approximation assumes that R approaches a finite value as $t \to 0$ and as $\sigma \to \infty$.

Three field equations relate the three unknowns, ρ, τ, and J. The first equation says that the tangential components of the electric field are zero at the interface.

$$\hat{y} \times (\overline{E}^i + \overline{E}^r - \overline{E}^t) = 0 \qquad (2.1\text{-}20)$$

Substituting (2.1-2), (2.1-16), and (2.1-18) into (2.1-20) gives the transmission coefficient in terms or the reflection coefficient.

$$\tau = 1 + \rho_r \qquad (2.1\text{-}21)$$

The next equation says that the tangential magnetic fields are discontinuous at the interface by the strip current density.

$$\hat{y} \times (\overline{H}^i + \overline{H}^r - \overline{H}^t) = \overline{J}_z \qquad (2.1\text{-}22)$$

Substituting the magnetic field quantities into this equation relates J_z, ρ_r, and τ.

$$(1 - \rho_r - \tau)sin\phi_o H_o e^{jkxcos\phi_o} = J_z \qquad (2.1\text{-}23)$$

Substituting (2.1-21) into (2.1-23) and solving for J_z leaves

$$J_z = -2\rho_r sin\phi_o H_o e^{jkxcos\phi_o} \qquad (2.1\text{-}24)$$

The final equation says that the total tangential electric field equals the strip current density times the strip resistivity.

$$E^i + E^r = RJ_z \qquad (2.1\text{-}25)$$

$$E_o e^{jkxcos\phi_o} + \rho_r E_o e^{jkxcos\phi_o} = RJ_z \qquad (2.1\text{-}26)$$

Solving this equation for ρ_r gives

$$\rho_r = \frac{-1}{1 + 2\eta sin\phi_o} \qquad (2.12\text{-}27)$$

Substituting (2.1-27) into (2.1-24) produces the final result with J in terms of the known quantities η, ϕ_o, H_o, and k.

$$J_z(x) = \frac{sin\phi_o}{.5 + \eta \sin\phi_o} H_o e^{jkx\cos\phi_o} \qquad (2.1\text{-}28)$$

A similar procedure for H-polarization gives

$$J_x(x) = \frac{sin\phi_o}{\eta + .5 \sin\phi_o} H_o e^{jkx\cos\phi_o} \qquad (2.1\text{-}29)$$

Equations (2.1-28) and (2.1-29) provide simple, but powerful relationships between J and η. These relationships are the key to synthesizing low sidelobe resistive tapers to control the scattering patterns of strips in Chapter III.

2.1.3 Comparison of the Integral Equation and Physical Optics Approaches

The PO derivation makes two approximations. First, the resistive sheet is assumed to be infinite in the x-y plane. Therefore, all edges are ignored. Second, (2.1-25) applies to an infinitely thin strip, just as in the integral equation approach. One can conclude that the integral equation and PO approaches agree very well under any conditions when the edge contribution is small compared to the total strip current. Examples of such conditions include

1. Scattering angles near broadside of a large strip

2. Highly resistive strips

3. Tapered resistive strips

A major goal of this thesis is to emphasize the excellent agreement between the PO and integral equation approaches under the above conditions [Haupt and Liepa, 1986].

Table 2.1 compares the two approaches for several types of resistive strips by listing the computed average rms error between the integral equation and PO approaches. As expected, the rms errors of the perfectly conducting strip are much higher than that of the resistive strip. The level of the errors change very little with increasing N (the number of points on the strip at which the current is calculated), but a much smaller value of N for a resistive strip will produce the same level of errors as a higher value of N for a perfectly conducting strip of the same width. Another observation is that increasing the width of

the strip decreases the level of the errors. This result is also expected, since the interaction between the edges gets less the farther apart they are. Graphs of the resistive tapers, currents, and scattering patterns similar to the examples in Table 2.1 appear in Chapter 3.

2.2 Solving the Integral Equations Using Collocation

One numerical method for solving (2.1-11) and (2.1-15) is collocation. The first step in the method is to expand the strip current density as a sum of complete, orthogonal basis functions.

$$J_s(x) = \sum_{n=1}^{\infty} \alpha_n J_n(x) \tag{2.2-1}$$

where

$$\int_{-a}^{a} w(x) J_n(x) J_m(x) dx = \delta_{mn}$$

$$w(x) = \text{weighting function}$$

$$J_n = \text{set of orthogonal basis functions}$$

$$\delta_{mn} = \text{Kronecker delta}$$

$$\alpha_n = \text{weighting coefficient}$$

The infinite summation in (2.2-1) may be approximated by N terms.

$$J_s(x) = \sum_{n=1}^{N} \alpha_n J_n(x) + r(x) \tag{2.2-2}$$

The residual error, $r(x)$, approaches zero as N approaches ∞ when $J_s(x)$ is a piecewise continuous function.

After substituting the approximation of J_z into (2.1-11) and matching the boundary conditions at N collocation points on the surface of the strip, the following series of equations results:

$$H_o e^{jkx_m \cos\phi_o} = \sum_{n=1}^{N} \alpha_n \left[\eta(x_m) J_n(x_m) + \frac{k}{4} \int_{-a}^{a} J_n(x') H_o^{(2)}(k|x_m - x'|) dx' \right], m = 1, 2, .., N$$

$$\tag{2.2-3}$$

COMPARISON OF PO AND INTEGRAL EQUATION APPROACHES								

$2a=4\lambda$		E-polarization				H-polarization			
η	N	σ_{curam}	σ_{curph}	σ_{bi}	σ_{bk}	σ_{curam}	σ_{curph}	σ_{bi}	σ_{bk}
0.0	40	0.191	8.309	0.105	0.119	0.335	15.757	0.104	0.106
	60	0.266	7.865	0.085	0.095	0.382	15.085	0.088	0.091
2.0	40	0.098	2.021	0.018	0.015	0.050	2.677	0.009	0.007
	60	0.031	1.912	0.014	0.011	0.025	3.278	0.007	0.005
$3(\frac{x}{a})^2$	40	0.037	1.504	0.048	0.016	0.031	1.901	0.005	0.004
	60	0.036	1.339	0.039	0.013	0.025	2.379	0.003	0.003
40dB Taylor $\bar{n}=12$	40	0.026	1.689	0.018	0.014	0.029	2.091	0.025	0.014
	60	0.023	1.312	0.014	0.011	0.022	1.835	0.013	0.007

$2a=6\lambda$		E-polarization				H-polarization			
η	N	σ_{curam}	σ_{curph}	σ_{bi}	σ_{bk}	σ_{curam}	σ_{curph}	σ_{bi}	σ_{bk}
0.0	60	0.152	6.831	0.081	0.091	0.270	13.685	0.088	0.081
	90	0.216	6.439	0.066	0.073	0.319	12.910	0.073	0.070
2.0	60	0.073	1.643	0.015	0.012	0.036	2.190	0.007	0.006
	90	0.022	1.558	0.012	0.010	0.018	2.674	0.005	0.004
$3(\frac{x}{a})^2$	60	0.022	1.308	0.022	0.011	0.019	1.551	0.004	0.003
	90	0.020	1.123	0.018	0.008	0.015	1.93	0.003	0.002
40dB Taylor $\bar{n}=12$	60	0.018	1.311	0.014	0.011	0.019	1.835	0.013	0.007
	90	0.017	1.064	0.011	0.008	0.016	1.952	0.009	0.004

N = number of points at which the current is calculated

η = normalized strip resistivity

σ_{curam} = average rms current amplitude error

σ_{curph} = average rms current phase error

σ_{bi} = average rms bistatic scattering error

σ_{bi} = average rms backscattering error

Table 2.1 — Comparison of the integral equation and PO optics approaches.

When (2.2-3) is put into the matrix form $A\alpha = V$ it is written as

$$
\begin{pmatrix}
a_{11} & a_{12} & \ldots & a_{1N} \\
a_{21} & a_{22} & \ldots & a_{2N} \\
\vdots & \vdots & \ddots & \vdots \\
a_{N1} & a_{N2} & \ldots & a_{NN}
\end{pmatrix}
\begin{pmatrix}
\alpha_1 \\
\alpha_2 \\
\vdots \\
\alpha_N
\end{pmatrix}
=
\begin{pmatrix}
v_1 \\
v_2 \\
\vdots \\
v_N
\end{pmatrix}
\tag{2.2-4}
$$

where

$$
v_m = e^{jkx_m\cos\phi_o}
$$

$$
a_{mn} = \eta(x_m)J_n(x_m) + \frac{k}{4}\int_{-a}^{a} J_n(x')H_o^{(2)}(k|x_m - x'|)dx'
\tag{2.2-5}
$$

The matrix equation is solved for the unknown coefficients, α_n, which are then substituted into (2.2-1) to get an approximation of the current on the strip.

A similar equation for H-polarization is

$$
H_o e^{jkx_m\cos\phi_o} = \sum_{n=1}^{N} \alpha_n\left[\eta(x_m)J_n(x_m) + \frac{k}{4}\int_{-a}^{a} \frac{H_o^{(2)}(k|x_m - x'|)}{k|x_m - x'|}J_n(x')dx'\right], m = 1, 2, .., N
\tag{2.2-6}
$$

When (2.2-6) is put into the matrix form of (2.2-4), the matrix elements are given by

$$
v_m = e^{jkx_m\cos\phi_o}\sin\phi_o
$$

$$
a_{mn} = \eta(x_m)J_n(x_m) + \frac{k}{4}\int_{-a}^{a} J_n(x')\frac{H_o^{(2)}(k|x_m - x'|)}{k|x_m - x'|}dx'
\tag{2.2-7}
$$

For the best results, the basis functions should be orthogonal, complete, easy to compute, and be able to match the boundary conditions. The list of possible basis functions is huge, and many trade-offs exist in selecting "the best ones" to use for a given problem. The two basis functions chosen for this application are pulses and Chebychev polynomials. They represent two extremely different types of basis functions. The pulse basis functions simplify the problem tremendously, are local (do not extend over the entire width of the strip), and do not allow accurate interpolation between collocation points. On the other hand, the Chebychev polynomial basis functions require more difficult numerical computations, are global (extend from -a to a), and allow very accurate interpolation between collocation points.

2.2.1 Collocation with Pulse Basis Functions

Pulse basis functions are commonly used for solving collocation problems in electromagnetics because of their simplicity. The strip is divided into N segments of equal size with the collocation points at the center of each segment. A pulse exists only over one of these segments and is represented by

$$J_n(x_m) = \begin{cases} 1, & |x_m - x_n| < \frac{\Delta}{2} \\ 0, & \text{otherwise} \end{cases} \qquad (2.2\text{-}8)$$

where $\Delta = x_{m+1} - x_m$. Substituting the pulses into (2.2-3) results in

$$H_o e^{jkx_m \cos\phi_o} = \sum_{n=1}^{N} \alpha_m \left[\delta_{mn} \eta(x_m) J_n(x_m) \right.$$
$$\left. + \frac{k}{4} \int_{-a+(n-1)\Delta}^{-a+n\Delta} H_o^{(2)}(k|x_m - x'|) dx' \right], m = 1, 2, .., N \qquad (2.2\text{-}9)$$

where

$$\delta_{mn} = \begin{cases} 1, & m = n \\ 0, & \text{otherwise} \end{cases}$$

The integral in (2.2-9) is straight-forward to evaluate except at x=x'. At this point Hankel function has a weak (logarithmic) singularity that requires a special integration procedure.

The off-diagonal elements of (2.2-4)are found using Gauss Chebychev Quadrature[6]

$$a_{Emn} = \frac{k\Delta\pi}{8L} \sum_{i=1}^{L} \sqrt{1 - y_i^2} H_0^{(2)}\left(k \left| x_m + a - n\Delta + \frac{\Delta}{2}[1 - y_i] \right| \right), \quad m \neq n \qquad (2.2\text{-}10a)$$

This equation is valid for diagonal and off-diagonal elements of the matrix as long as one of the quadrature points does not fall on one of the collocation points.

---

[6] The Gauss Chebychev Quadrature integration formula is [Pearson, 1983]

$$\int_a^b \frac{f(y) dy}{\sqrt{(1 - y^2)}} = \frac{\pi}{L} \frac{(b - a)}{2} \sum_{i=1}^{L} f(\frac{b + a}{2} + \frac{b - a}{2} z_i)$$

where z_i are the zeros of the Lth order Chebychev polynomial given by

$$z_i = \cos\left[\frac{\pi(i - 0.5)}{L} \right], \quad m = 1, 2, ..., L$$

The diagonal elements of (2.2-10a) are very slowly convergent because of the singularity in the integration interval. This singularity may be avoided by splitting the Hankel function into its real and imaginary parts and making a simple transformation of variables [Boyd, 1986] for the Neumann function:

$$e^z = \begin{cases} k(x_m - x'), & x_m > x' \\ k(x' - x_m), & x' \geq x_m \end{cases} \qquad (2.2\text{-}11)$$

The diagonal elements now become

$$a_{Enn} = \eta(x_n) + \frac{\pi}{2} \int_{-a+(n-1)\Delta}^{-a+n\Delta} J_o(k|x_m - x'|)dx' + j\frac{k}{4} \int_{LL}^{ln(x_m+a-n\Delta)} Y_o(e^z)e^z dz \quad (2.2\text{-}12a)$$

where

$$J_o = \text{zero}^{th} \text{ order Bessel function}$$

$$Y_o = \text{zero}^{th} \text{ order Neumann function}$$

The exact transformation for the Neumann function integral has LL equal to $-\infty$; however, a much smaller negative value will produce excellent results. This form of the integral converges much faster when evaluating the singularity than the integral (2.2-10a). If the spacing between collocation points is $\leq \frac{\lambda}{10}$ and the lower limit is approximated by -8, then this integral is accurate to four decimal places when evaluated with a 10 point Gauss Chebychev Quadrature rule.

When the incident field is H-polarized, the matrix elements are given by Off-diagonal:

$$\begin{aligned} a_{Hmn}(x_m) = &\frac{x_m + a - (n-1)\Delta}{4|x_m + a - (n-1)\Delta|} H_1^{(2)}(2\pi|x_m + a - (n-1)\Delta|) - \\ &\frac{x_m + a - n\Delta}{4|x_m + a - n\Delta|} H_1^{(2)}(2\pi|x_m + a - n\Delta|) + \\ &\frac{k\Delta\pi}{8L} \sum_{i=1}^{L} \sqrt{1 - y_i^2} H_0^{(2)}\left(k\left|x_m + a - n\Delta + \frac{\Delta}{2}[1 - y_i]\right|\right), \\ &m \neq n \quad m \neq n \end{aligned} \qquad (2.2\text{-}13a)$$

Diagonal:

$$a_{Hnn} = \eta(x_n) + \frac{\pi}{2} \int_{-a+(n-1)\Delta}^{-a+n\Delta} J_1(k|x_m - x'|)dx' + j\frac{1}{2} \int_{LL}^{ln(x_m+a-n\Delta)} Y_1(e^z)e^z dz \quad (2.2\text{-}14a)$$

Midpoint integration gives a cruder approximation to the integrals, but is accurate enough for the applications considered. It assumes that the current and the Hankel function are constant over the interval of integration. The Gauss-Chebychev quadrature integration assumes that the current is constant over the interval, but not the Hankel function. Since the Hankel function varies faster over the interval than the current, this method is more accurate than midpoint integration.

Midpoint integration is attractive, though, because of its simplicity. It requires far fewer function evaluations than the Gauss-Chebychev quadrature formula, which makes it considerably faster. The midpoint integration formulas are given by

$$a_{Emm} = \eta(x_m) + \frac{k}{4}\Delta[1 - j\frac{2}{\pi}(0.0287983 + ln\Delta)] \quad (2.2\text{-}10b)$$

$$a_{Emn} = \frac{k}{4}\Delta H_o^{(2)}(k|x_m - x_n|) \quad (2.2\text{-}12b)$$

$$a_{Hmm} = \eta(x_m) + \frac{k}{4}\Delta[.5 - j\frac{1}{\pi}(0.0287983 + ln\Delta + \frac{1}{2\pi^2\Delta^2} - \frac{1}{2}) \quad (2.2\text{-}13b)$$

$$a_{Hmn} = \frac{x_m - x_n - .5\Delta}{4|x_m - x_n - .5\Delta|}\left[H_1^{(2)}(k|x_m - x_n - .5\Delta|) + H_1^{(2)}(k|x_m - x_n - .5\Delta|)\right] +$$

$$\frac{k}{4}\Delta H_o^{(2)}(k|x_m - x_n|) \quad (2.2\text{-}14b)$$

A comparison of the two integration methods appears in Table 2.2. Generally, agreement between the two integration techniques increases as the number of collocation points increases, because the Hankel function variations are less for a smaller interval. Thus, assuming the Hankel function is constant over the interval is a better approximation as the interval gets smaller, and midpoint integration gets more accurate. The agreement also increases as the strip resistivity increases, because the integral contribution in (2.2-11) and (2.2-15) decreases relative to the contribution from the resistive term. Since the two methods produce very similar results, midpoint integration is the best choice because it is computationally much faster.

2.2.2 Collocation with Chebychev Polynomial Basis Functions

		$\phi_o = 90°$			$\phi_o = 30°$			
η	N	σ_{curamp}	σ_{curph}	σ_{bi}	σ_{curamp}	σ_{curph}	σ_{bi}	σ_{bk}
0.0	20	0.02745	0.67735	0.03354	0.05728	1.12111	0.03046	0.03627
	40	0.02297	0.60610	0.01014	0.02624	0.51957	0.00346	0.00830
	60	0.02311	0.45290	0.00749	0.02369	0.37244	0.00225	0.00582
2.0	20	0.00065	0.23010	0.00199	0.00542	0.36435	0.00177	0.00177
	40	0.00023	0.12972	0.00047	0.00111	0.13954	0.00026	0.00038
	60	0.00021	0.08735	0.00032	0.00032	0.07776	0.00009	0.00024
$3(\frac{z}{a})^2$	20	0.00175	0.36399	0.00405	0.02513	0.82835	0.00121	0.00201
	40	0.00185	0.30643	0.00323	0.00472	0.29316	0.00017	0.00250
	60	0.00218	0.21998	0.00311	0.00118	0.16022	0.00008	0.00230
40dB	20	0.00136	0.42698	0.00359	0.02875	0.84281	0.00073	0.00336
Taylor	40	0.00254	0.35564	0.00446	0.00548	0.30659	0.00011	0.00341
$\bar{n}=12$	60	0.00284	0.25493	0.00405	0.00141	0.17236	0.00004	0.00299

AVERAGE RMS ERRORS BETWEEN INTEGRATING THE MATRIX ELEMENTS WITH MIDPOINT INTEGRATION VS. GAUSS-CHEBYCHEV QUADRATURE INTEGRATION

N = number of points at which the current is calculated
η = normalized strip resistivity
σ_{curam} = average rms current amplitude error
σ_{curph} = average rms current phase error
σ_{bi} = average rms bistatic scattering error
σ_{bi} = average rms backscattering error

Table 2.2 — Comparison of the midpoint and Gauss-Chebychev quadrature integration schemes for finding the elements in the collocation matrix.

Another alternative to the basis functions in (2.2-1) is Chebychev polynomials:

$$J_n(x) = T_{n-1}(\frac{x}{a}) = cos[(n-1)cos^{-1}(\frac{x}{a})] \qquad (2.2\text{-}15)$$

In this case, the optimum spacing of the collocation points are given by the zeros of the Nth order Chebychev polynomial:

$$x_i == cos\left[\frac{\pi(i-0.5)}{N}\right] \qquad (2.2\text{-}16)$$

the following equations result upon substituting (2.2-15) into (2.2-3) and (2.2-6):

E-polarization

$$
\begin{aligned}
H_o e^{jkx_m cos\phi_o} = \sum_{n=1}^{N} \alpha_n \Bigl[& \eta(x_m)T_{n-1}(\frac{x_m}{a}) + \frac{k}{4}\int_{-a}^{a} T_{n-1}(\frac{x'}{a})J_o(k|x_m - x'|)dx' \\
& - j\frac{k}{4}\int_{-a}^{x_m^-} T_{n-1}(\frac{x'}{a})Y_o(k|x_m - x'|)dx' \\
& - j\frac{k}{4}\int_{x_m^-}^{x_m^+} T_{n-1}(\frac{x'}{a})Y_o(k|x_m - x'|)dx' \\
& - j\frac{k}{4}\int_{x_m^+}^{a} T_{n-1}(\frac{x'}{a})Y_o(k|x_m - x'|)dx' \Bigr], m = 1,2,..,N \qquad (2.2\text{-}17)
\end{aligned}
$$

H-polarization

$$
\begin{aligned}
H_o e^{jkx_m cos\phi_o} = \sum_{n=1}^{N} \alpha_n \Bigl[& \eta(x_m)T_{n-1}(\frac{x_m}{a}) + \frac{k}{4}\int_{-a}^{a} \frac{J_1(k|x_m - x'|)}{k|x_m - x'|}T_{n-1}(\frac{x'}{a})dx' \\
& - j\frac{k}{4}\int_{-a}^{x_{m-}} \frac{Y_1(k|x_m - x'|)}{k|x_m - x'|}T_{n-1}(\frac{x'}{a})dx' \\
& - j\frac{k}{4}\int_{x_{m-}}^{x_{m+}} \frac{Y_1(k|x_m - x'|)}{k|x_m - x'|}T_{n-1}(\frac{x'}{a})dx' \\
& - j\frac{k}{4}\int_{x_{m+}}^{a} \frac{Y_1(k|x_m - x'|)}{k|x_m - x'|}T_{n-1}(\frac{x'}{a})dx' \Bigr], m = 1,2,..,N \qquad (2.2\text{-}18)
\end{aligned}
$$

The integrals involving only the J_o term are computed with an adaptive quadrature integrator that uses 10-point Gauss-Legendre and 21-point Kronrod formulas on both halves of a subinterval. This integration subroutine (QKSQ) may be found in the NAAS library.

Before solving the Y_o integral, however, it is split into three integrals. The two end integrals do not contain any singularity and may be evaluated with the adaptive quadrature

routine. On the other hand, the center integral does contain a singularity. When the interval from x_m^- to x_m^+ is small, then certain approximations aid in accurately evaluating the integral over that interval. The first approximation replaces Y_o and Y_1 with their small argument representation.

$$Y_o(z) = \frac{2}{\pi}[ln(\frac{z}{2}) + \gamma]$$
(2.2-19)

$$Y_1(z) = \frac{z}{\pi}[ln(\frac{z}{2}) + \gamma - \frac{1}{\pi}] - \frac{2}{\pi z}$$
(2.2-20)

Next, the Chebychev polynomial is assumed to be constant over that interval. Now, a simple transformation of variables and the formula $\int_0^1 ln(x)dx = 1$ results in

E-polarization:

$$-j\frac{k}{4}\int_{x_m^-}^{x_m^+} T_{n-1}(\frac{x'}{a})Y_o(k|x_m - x'|)dx' = \frac{k}{4}\Delta T_{n-1}(\frac{x_m}{a})\left[1 - j\frac{2}{\pi}(0.0287983 + ln\,\Delta)\right]$$
(2.2-21)

H-polarization:

$$-j\frac{k}{4}\int_{x_{m^-}}^{x_{m^+}} T_{n-1}(\frac{x'}{a})\frac{Y_o(k|x_m - x'|)}{k|x_m - x'|}dx' = \frac{k}{4}\Delta T_{n-1}(\frac{x_m}{a})\left[\Delta + j\frac{2}{\pi}(0.41712017 - ln\,\Delta - \frac{1}{\pi^2\Delta})\right]$$
(2.2-22)

One must be careful to choose a sufficiently small interval where this approximation holds. When N is large the Chebychev polynomial oscillates very rapidly and the interval should be quite small. A good size for the interval is twice the distance from the edge of the strip to the first collocation point. This interval has the advantage of getting smaller in size as N increases, and when m=n=1 or N, only two of the integrals over the Neumann functions in (2.2-17) or (2.2-18) need to be performed.

2.2.3 _A Comparison of Collocation with Pulse and Chebychev Basis Functions_

In the applications considered in this thesis, pulse basis functions produce better results than the Chebychev basis functions for several reasons. First, the Chebychev polynomials must be integrated over the entire interval length of 2a for each matrix element, whereas the pulses are integrated over a length of $\frac{2a}{N}$. In addition, as N increases, the Chebychev

polynomials require more integration points because of the higher oscillation frequency. The integration is very time consuming due to the many function calls for the Hankel function. Thus, the major time factor when using Chebychev polynomials is not solving the matrix equation, but setting-up the A matrix. Second, Chebychev basis functions promise exponential convergence only when there are no singularities on the interval. The Hankel function singularity when the source and observation points coincide slow down the convergence speed of these basis functions. Third, the pulse basis function's A matrix becomes diagonally dominant as the strip resistivity of the strip increases, whereas the Chebychev basis function's A matrix does not. The diagonal dominance speeds the convergence of iterative techniques. Fourth, the ultimate goal is to find the far field scattering patterns and not the strip current. The Fourier Transform from the current to the far field tends to smooth the errors. Hence, the calculation of the strip current does not require the accuracy given by more sophisticated methods such as using chebychev polynomial basis functions.

As a result of the above discussion, pulse basis functions are used in this thesis and the integral is evaluated with midpoint integration. This combination produces excellent results while conserving computer time.

2.2.4 Choosing the Number of Basis Functions

It is important to choose enough basis functions to get an accurate result. However, minimizing the number of basis functions reduces the amount of computer time. Is there a good value for N so that computer time is minimized without sacrificing accuracy?

An answer to this question depends upon the desired output. An accurate representation of the strip current density requires more basis functions than an accurate representation of the scattering patterns. The far field calculations tend to average current errors, so they have less of an impact on the scattering patterns.

Table 2.3 shows some interesting results with regards to choosing N. The average rms bistatic scattering errors (σ_{bi}) and backscattering errors (σ_{bi}) are calculated by comparing t he scattering patterns when N=20, 40, and 60 with the scattering patterns when N=100. One striking observation is that far fewer basis functions are necessary to obtain an accurate answer for a resistive strip than for a perfectly conducting strip. The resistive strip errors when N=20 are at least as good as the perfectly conducting strip errors when N=60. When

the scattering patterns for the cases in the table were graphed, they were not noticably different as N increased from 20 to 60. Although, graphs of the strip current were slightly different as N increased. A sampling interval of 12 match points per wavelength is deemed adequate for the examples presented later.

2.3 Techniques for Solving the Matrix Equation

The matrix equation, (2.2-4), for the strip current density may be solved in one of several ways. Of the techniques investigated, PLU decomposition and back-substitution is the recommended approach in this thesis because the matrices are small and well-conditioned. Another approach is iterative methods. Three types of iterative methods are considered: 1) relaxation, 2) secant, and 3) Steffensen's acceleration. The final approach is conjugate gradient. This approach is currently receiving considerable attention in the literature. Often Conjugate Gradient is considered an iterative method. Here, it is not for two reasons. First, unlike the iterative methods mentioned, Conjugate Gradient is guaranteed to converge in a finite number of steps if the A matrix is properly formed. Second, it does not require a relaxation constant.

Iterative methods and conjugate gradient are generally only used for large, sparse, or near singular matrices. The matrices in this thesis do not fall under any of these categories. The motivation for trying these techniques is to use the PO current as a first guess to speed the convergence of the algorithms. Unfortunately, the PO current failed to increase convergence much faster than assuming an inititial guess for the current of 0.

2.3.1 PLU decomposition and back-substitution

PLU decomposition and back-substitution is a form of Gaussian elimination where the lower diagonal matrix (L) contains the factors that converted the matrix A to an upper triangular matrix (U) using Gaussian elimination. U and L replace the original A in the computation. The P matrix is a partial pivoting matrix that multiplies A in order to interchange rows in the matrix to reduce numerical error.

The NAAS (Numerical Analysis and Applications Software) library has complex PLU decomposition and back-substitution subroutines. Here, the subroutine CGECO forms the PLU decomposition and the subroutine CGESL performs the back-substitution.

AVERAGE RMS SCATTERING PATTERN ERRORS[†] AS A FUNCTION OF N, THE NUMBER OF PULSES					
PULSE BASIS FUNCTIONS		E-polarization		H-polarization	
η	N	σ_{bi} ($\phi_o = 90°$)	σ_{bk}	σ_{bi} ($\phi_o = 90°$)	σ_{bk}
0.0	20	0.0552	0.0544	0.1131	0.1364
	40	0.0198	0.0179	0.0242	0.0379
	60	0.0085	0.0075	0.0096	0.0147
2.0	20	0.0039	0.0081	0.0040	0.0039
	40	0.0008	0.0016	0.0021	0.0018
	60	0.0003	0.0005	0.0011	0.0010
$3(\frac{x}{a})^2$	20	0.0026	0.0055	0.0020	0.0023
	40	0.0005	0.0012	0.0017	0.0014
	60	0.0001	0.0004	0.0006	0.0005
40dB Taylor $\bar{n}=12$	20	0.0066	0.0074	0.0240	0.0174
	40	0.0014	0.0015	0.0035	0.0026
	60	0.0005	0.0005	0.0011	0.0008

[†]σ is the rms errror between the scattering patterns with N=20, 40, and 60 and the scattering patterns with N=100

$$N = \text{number of points at which the current is calculated}$$
$$\eta = \text{normalized strip resistivity}$$
$$\sigma_{curam} = \text{average rms current amplitude error}$$
$$\sigma_{curph} = \text{average rms current phase error}$$
$$\sigma_{bi} = \text{average rms bistatic scattering error}$$
$$\sigma_{bi} = \text{average rms backscattering error}$$

Table 2.3 — The average rms error between scattering patterns with either 20, 40, or 60 basis functions and one with 100 basis functions is listed.

A total of $\frac{1}{3}(4N^3+6N^2-10N)$ real multiplications and $\frac{4}{3}N^3+8N^2-\frac{28}{3}N$ real additions[7] are required for PLU decomposition and back-substitution. Only $2N^2 + 2N$ real multiplications and $N^2 - N$ real additions are required for back-substitution alone. When the same A matrix is used to solve for the current with a new right-hand-side, the U and L forms remain the same. The new current is found by back-substitution. Thus, when calculating backscattering patterns, only $2N^2 + 2N$ real multiplications and $N^2 - N$ real additions are required for calculating the current at each backscattering angle once the initial PLU decomposition is done. Backsubstitution is much faster than a single step in any of the iterative methods or conjugate gradient.

2.3.2 Iterative Methods

An iterative method for solving the matrix equations in section 2.2 begins with an initial guess $J^{(0)}$ and computes a sequence of vectors $(J^0, J^1, ..., J^k)$ that converges to the correct answer, J_s, as $k \rightarrow \infty$. If one had an excellent first guess, the iterative method may converge faster than a first guess of 0. Since the PO current is rather simple to calculate and models the actual current reasonably well (especially for resistive strips), it is a good candidate for the first guess. As it turns out, however, PO does not substantially improve the convergence of these algorithms. When calculating backscattering patterns, a good first guess is the current from the previous backscattering angle. This guess does significantly improve the convergence of the algorithms. When calculating backscattering currents with iterative methods, one should begin at $\phi_o = \phi = 90°$ and procede to $\phi = 0°$, because convergence is much faster at $\phi = 90°$ than at $\phi = 0°$. Having the current from the previous angle as a first guess for the current at edge-on incidence substantially reduces the convergence time.

Three iterative methods are presented in this section. The first method, relaxation, appears again in Chapter 4 for the solution of a finite difference equation. The second method, secant method, is a finite difference form of Newton's method. The third method, Steffensen's acceleration, has the greatest stability of the three methods.

2.3.2.1 Relaxation

---

[7] Four real multiplications constitute one complex multiplication and two real additions constitute one complex addition

Relaxation is a modification to the Gauss-Seidel procedure. Its formula for a matrix solution is given by [Burden and Fares, 1985]

$$J_m^{(k)} = (1 - \omega)J_m^{(k-1)} + \frac{\omega}{a_{mm}}\left[v_m - \sum_{n=1}^{m-1} a_{mn}J_n^{(k)} - \sum_{n=m+1}^{N} a_{mn}J_n^{(k-1)}\right] \qquad (2.3\text{-}1)$$

where

m = row number in vector or matrix

n = column number in vector or matrix

k = iteration number

ω = relaxation number

a_{mn} = element of the matrix in (2.2-4)

v_m = element of incident field vector in (2.2-4)

A starting value for the strip current density, $J^{(0)}$, is either the PO approximation or 0.

The relaxation constant determines the convergence speed of the algorithm. An optimum value of ω is [Ferziger, 1981]

$$\omega_{opt} = \frac{2}{1 + \sqrt{(1 - \lambda_{max}^2)}} \qquad (2.3\text{-}2)$$

where λ_{max} is the maximum eigenvalue or spectral radius of the A matrix. Rather than calculating λ_{max}, one often plots ω versus the number of iterations to convergence. A very sharp dip in this graph occurs at the value of ω_{opt}.

For the matrices in this thesis, ω is less than 1, so the method is known as an under relaxation method. This method requires $4N^2 + 2N + 2$ real multiplications and $2N^2 + 3N$ real additions per iteration. If the relaxation method converges in $\frac{4}{9}N$ steps, then it is as fast as PLU decomposition and back-substitution. However, even one iteration takes longer than back-substitution alone.

2.3.2.2 Secant Method

The secant method is Newton's method with the derivative approximated by a finite difference formula. This method searches for a $J_s(x)$ such that a function $f\left(J_s(x)\right) = 0$. Putting the E-polarized integral equation into this form gives

$$f\left(J_s(x)\right) = - H_o e^{jkx\cos\,\phi_o} + \eta(x)J_z(x) + \frac{k}{4}\int_{-a}^{a} J_z(x')H_o^{(2)}(k|x - x'|)dx' = 0$$

$$f\left(J_m^{(k)}\right) = v_m + \sum_{n=1}^{m-1} a_{mn}J_n^{(k)} + \sum_{n=m}^{N} a_{mn}J_n^{(k-1)} \qquad (2.3\text{-}3)$$

where $J_m^{(k)}$ is the current update given by (2.3-1) and $J_m^{(k-1)}$ is the last update. The iterative formula is given by

$$J_m^{(k)} = J_m^{(k-1)} - \frac{f\left(J_m^{(k-1)}\right)}{f'\left(J_m^{(k-1)}\right)} = J_m^{(k-1)} - \frac{\left[J_m^{(k-1)} - J_m^{(k-2)}\right]}{1 - \frac{f\left(J_m^{(k-2)}\right)}{f\left(J_m^{(k-1)}\right)}} \qquad (2.3\text{-}4)$$

Two initial guesses are necessary for starting the algorithm. For bistatic scattering and backscattering at $\phi_o = 90°$, the first guess is the PO approximation of the current. The second guess comes from one iteration of the the relaxation algorithm. For the remaining backscattering angles, the first guess is PO and the second guess is the current from the previous angle.

This method requires $8N^2 + 4N$ real multiplications and $4N^2 + 9N$ real additions per iteration. If the secant method converges in $\frac{2}{9}N$ steps, then it is as fast as PLU decomposition and back-substitution. However, even one iteration takes longer than back-substitution alone.

2.3.2.3 Steffensen's Acceleration

Steffensen's acceleration accelerates the convergence of an iterative technique, usually fixed point iteration. Here it is used to accelerate relaxation. The formula for the algorithm is given by [Burden and Fares, 1985]

$$J_m^{(0)} = \text{PO approximation or } 0$$

$$J_m^{(1)} = (1 - \omega)J_m^{(0)} + \frac{\omega}{a_{mm}}\left[v_m - \sum_{n=1}^{m-1} a_{mn}J_m^{(1)} - \sum_{n=m+1}^{N} a_{mn}J_m^{(0)}\right] = \text{relaxation}$$

$$J_m^{(2)} = (1 - \omega)J_m^{(1)} + \frac{\omega}{a_{mm}}\left[v_m - \sum_{n=1}^{m-1} a_{mn}J_m^{(2)} + \sum_{n=m+1}^{N} a_{mn}J_m^{(1)}\right] = \text{relaxation}$$

$$J_m^{(3)} = J_m^{(0)} - \frac{\left(J_m^{(1)} - J_m^{(0)}\right)^2}{J_m^{(2)} - 2J_m^{(1)} + J_m^{(0)}} = \text{Steffensen's acceleration}$$

If $J_m^{(3)}$ does not have the desired accuracy, then substitute $J_m^{(3)}$ into $J_m^{(0)}$ and repeat the steps.

This method requires $8N^2 + 8N + 4$ real multiplications and $4N^2 + 10N$ real additions per iteration. If Steffensen's acceleration converges in $\frac{2}{9}N$ steps, then it is as fast as PLU decomposition and back-substitution. However, even one iteration takes longer than back-substitution alone.

2.3.3 Conjugate Gradient

The conjugate gradient algorithm combines some of the major advantages of PLU decomposition and back-substitution, and iterative methods. First, as in iterative methods, the round-off and truncation errors are limited to the final step. Thus, this method produces more accurate results for near singular matrices than does PLU decomposition and back-substitution. Second, as in PLU decomposition and back-substitution, this algorithm converges to the answer in a finite number of steps. Thus, this method converges in N steps, whereas iterative methods do not.

The conjugate gradient algorithm is described below [Sarkar and Arvas, 1985].

Initializat :

$$J^{(0)} = \text{PO approximation}$$

$$r^{(0)} = V - AJ^{(0)}$$

$$p^{(0)} = A^\dagger r^{(0)}$$

The following steps are repeated until some tolerance is achieved or the number of iterations=N:

$$\alpha^{(k)} = \frac{||r^{(k)}||^2}{||p^{(k)}||^2}$$

$$J^{(k+1)} = J^{(k)} + \alpha^{(k)} p^{(k)}$$

$$r^{(k+1)} = r^{(k)} - \alpha^{(k)} A p^{(k)}$$

$$\beta^k = \frac{||r^{(k+1)}||^2}{||r^{(k)}||^2}$$

$$p^{(k+1)} = A^\dagger r^{(k+1)} + \beta^{(k)} p^{(k)}$$

The norm of a vector is given by

$$||r|| = \sqrt{\sum_{i=1}^{N} r_i r_i^*}$$

where r_i^* is the complex conjugate of vector element r_i.

This method requires $8N^2 + 16N$ real multiplications and $10N^2$ real additions per iteration plus $8N^2$ real multiplications and 2N real additions in the initialization. If the conjugate gradient method converges in $\frac{3}{9}N$ steps, then it is as fast as PLU decomposition and back-substitution. However, even one iteration is slower than back-substitution alone.

2.3.4 A Comparison of the Matrix-Solving Techniques

The two criteria for choosing a matrix solving technique are accuracy and speed, with accuracy being the more important. Accuracy is checked by determining if a technique converges to the correct answer and if the numerical errors are tolerable. Speed is checked by counting the total number of floating point operation (FLOPS) - multiplications and additions.

Tables 2.4 to 2.7 help compare the five choices of matrix solving routines. Tables 2.4 to 2.6 show the number of iterations needed for one of the iterative methods or Conjugate Gradient to converge to the correct answer (rms error of .01) when calculating the strip current for an incident plane wave at 90°. An "*" means the method diverges and an "s" means it slowly converges (more than 100 iterations). There are four resistive tapers:

$\eta = 0, 1, 2$, and x^2; two polarizations: E- and H- polarization; two sizes of strips: 2a=2λ and 8λ or matrices that are 24×24 and 96×96, respectively; and two choices of an initial guess: PO current and 0.

Table 2.7a lists the number of real FLOPS for a single iteration. The numbers from Tables 2.4 to 2.6 may be substituted into the formulas to determine the total length of time taken by one of the techniques. If the total number of FLOPS is less than the number in the last column, then the technique is faster than PLU decomposition and back-substitution. The number of FLOPS in a single iteration for any of the iterative methods or conjugate gradient is slower than back-substitution alone.

The number of FLOPS for PO is listed for two reasons. First, to show how fast this method is compared to all the other methods. Second, to show how much longer an initial guess of the PO current takes to calculate. If PO reduces the number of iterations by 1, it is worth using. The hope is that it will substantially reduce the number of iterations, especially for resistive strips.

The first check for accuracy is to determine whether the methods converge to the correct answer after a reasonable time. Tables 2.4 to 2.6 show that only the secant method refuses to converge for all resistive tapers. A value for ω is listed for the secant method because the second guess is found from the relaxation formula. It is also quite slow for the tapered resistive strips. The relaxation method did not converge for perfectly conducting strips when $\omega \geq 1$. Thus, only the secant method is discarded as a potential candidate.

As for numerical errors, all the methods provide an adequate representation of the current for the cases in this thesis. The iterative methods have the advantage of limiting numerical errors to only the last iteration. Accuracy in all the methods may be improved by using double precision, if necessary.

The speed of the algorithms are measured by counting the total number of FLOPS (Floating point Operations) needed to find the strip current for one angle of incidence. For the iterative methods, the total number of FLOPS = number of iterations to convergence times the number of FLOPS per iteration. Table 2.7 gives that type of information. Plugging the numbers from Tables 2.4 to 2.6 into the formulas in Table 2.7 result in a good idea of how fast these algorithms are.

Number of Iterations to Convergence

E-polarization, initial guess is 0, strip is 2λ wide, matrix has 24×24 elements							
Resistive taper	Relaxation		Secant Method		Steffensen's Iteration		Conjugate Gradient
	$\omega = 1.0$	$\omega = 0.5$	$\omega = 1.0$	$\omega = 0.5$	$\omega = 1.0$	$\omega = 0.5$	
$\eta = 0$	*	15	113	171	10	9	12
$\eta = 1$	7	8	7	7	3	3	5
$\eta = 2$	5	7	4	4	2	2	4
$\eta = x^2$	22	9	24	26	5	4	7

E-polarization, initial guess is PO, strip is 2λ wide, matrix has 24×24 elements							
Resistive taper	Relaxation		Secant Method		Steffensen's Iteration		Conjugate Gradient
	$\omega = 1.0$	$\omega = 0.5$	$\omega = 1.0$	$\omega = 0.5$	$\omega = 1.0$	$\omega = 0.5$	
$\eta = 0$	*	14	227	113	9	8	10
$\eta = 1$	6	5	6	6	3	4	4
$\eta = 2$	4	4	4	4	2	2	3
$\eta = x^2$	20	8	48	48	5	5	7

ω is the relaxation constant for relaxation

* means the method diverges

Table 2.4 — The number of iterations until convergence is listed for the iterative methods and conjugate gradient when the incident field is E-polarized and the matrix has 24×24 elements.

Number of Iterations to Convergence						
H-polarization, initial guess is 0, strip is 2λ wide						

Resistive taper	SOR		Secant Method		Steffensen's Iteration		Conjugate Gradient
	$\omega = 1.0$	$\omega = 0.5$	$\omega = 1.0$	$\omega = 0.5$	$\omega = 1.0$	$\omega = 0.5$	
$\eta = 0$	*	298	*	*	49	87	13
$\eta = 1$	8	13	6	6	4	4	6
$\eta = 2$	5	9	4	4	2	2	4
$\eta = x^2$	160	87	95	49	11	10	13

H-polarization, initial guess is PO, strip is 2λ wide						

Resistive taper	SOR		Secant Method		Steffensen's Iteration		Conjugate Gradient
	$\omega = 1.0$	$\omega = 0.5$	$\omega = 1.0$	$\omega = 0.5$	$\omega = 1.0$	$\omega = 0.5$	
$\eta = 0$	*	159	*	*	39	69	13
$\eta = 1$	6	8	5	6	4	6	5
$\eta = 2$	3	5	4	4	2	2	3
$\eta = x^2$	107	38	188	71	5	5	10

ω is the relaxation constant for SOR
* means the method did not converge

Table 2.5 — The number of iterations until convergence is listed for the iterative methods and conjugate gradient when the incident field is H-polarized and the matrix has 24×24 elements.

| Number of Iterations to Convergence |

| E-polarization, initial guess is 0, strip is 8λ wide, matrix has 96×96 elements |

Resistive taper	relaxation constant	Relaxation	Secant Method	Steffensen's Iteration	Conjugate Gradient
$\eta = 0$	$\omega=.32$	22	s	16	26
$\eta = 1$	$\omega=.6$	8	14	3	7
$\eta = 2$	$\omega=.8$	5	6	3	5
$\eta = x^2$	$\omega=.45$	14	61	6	12

| E-polarization, initial guess is PO, strip is 8λ wide, matrix has 96×96 elements |

Resistive taper	relaxation constant	Relaxation	Secant Method	Steffensen's Iteration	Conjugate Gradient
$\eta = 0$	$\omega=.32$	20	s	13	26
$\eta = 1$	$\omega=.6$	7	10	4	7
$\eta = 2$	$\omega=.8$	4	4	2	5
$\eta = x^2$	$\omega=.6$	18	s	8	12

ω is the relaxation constant for relaxation
s means the method converges very slowly (>100 iterations)

Table 2.6 — The number of iterations until convergence are listed for the iterative methods and conjugate gradient when the incident field is E-polarized and the matrix has 96×96 elements.

Technique	FLOPS per iteration	Number of iterations needed to make the total number of FLOPS for each technique equal to the total number of FLOPS for PLU decomposition and back-substitution
Relaxation	$6N^2 + 5N + 2$	$\frac{4}{9}N$
Secant	$12N^2 + 13N$	$\frac{2}{9}N$
Steffensen's	$12N^2 + 8N + 4$	$\frac{2}{9}N$
Conjugate gradient	$18N^2 + 16N$	$\frac{3}{9}N$

a. The technique is listed in the first column, the number of FLOPS per iteration is listed in the second column, and column 2 times column 3 approximatelly equals the total number of FLOPS in PLU decomposition and back-substitution.

Technique	Total number of FLOPS
PLU Decomposition	$\frac{1}{3}(8N^2 + 30N^2 + 38N)$
Back-substitution	$3N^2 + N$
PO	$9N + 4 + 4$ Trig. function evaluations

b. Number of FLOPS for PLU decomposition, back-substitution, and PO are listed.

Table 2.7 — The number of Floating Point Operations (FLOPS) are listed for the various methods given a matrix with N×N elements.

PLU decomposition and back-substitution produces the fastest results for the matrices encountered in this thesis for two reasons. First, the matrices are generally small (less than 100×100 elements). The total number of real multiplications for PLU decomposition and back-substitution and the iterative methods and conjugate gradient are equal at about 100×100 elements. Below this point PLU decomposition and back-substitution is fastest and above this point iterative methods and conjugate gradient are the fastest. Second, the PLU decomposition and back-substitution only has to be calculated for one angle when solving for the backscattering pattern. The remaining angles only require backsubstitution, which takes far less time than a single step in any of the iterative methods.

Table 2.7a compares the number of real operations required for the iterative methods and conjugate gradient. It also shows the number of iterations that will produce the same number of total operations as PLU decomposition and back-substitution, back-substitution alone, and PO. Using the PO current as an initial guess adds a very small number of multiplications to the iterative methods. Although the total number of multiplications for PLU decomposition and back-substitution is large, the number of multiplications for backsubstitution alone is very small. This feature makes PLU decomposition and back-substitution attractive for calculating backscattering patterns.

The main motivation for trying iterative methods in this thesis is to find out if the PO current results in a good first guess. Tables 2.4 to 2.6 compare the methods for convergence speed. The results indicate that PO contributes little to speeding the convergence of the algorithms compared to using 0 as the first guess. PO fails to be an excellent first guess, because it models only the real part of the current and not the imaginary part. Consequently, approximately the same number of steps are needed to converge for the imaginary part as for the real part with an initial guess of 0. Perhaps some good guess for the imaginary part of the current would possibly speed up the iteration.

As already mentioned, the current from the previous backscattering angle is an excellent first guess of the current at the angle presently being calculated. This guess gets better as the increment between angles gets smaller. For one degree increments, this first guess results in a 3 to 4 fold savings in the number of iterations to convergence, compared to starting with 0 as the initial guess.

If the matrix were large enough to justify using a technique other than PLU decomposition and back-substitution, then one of the other techniques must be decided upon. Relaxation is the fastest of the remaining techniques, but is very sensitive to the value of ω. The sensitivity seems to increase as the size of the matrix increases and as the strip resistivity decreases. If the maximum eigenvalue is known, then ω_{opt} can be calculated, otherwise calculating the maximum eigenvalue is not worth the trouble and one of the other techniques should be used.

Steffensen's acceleration also relies upon the value of ω, but as can be inferred from Tables 2.4 to 2.6, is far less sensitive to this value than relaxation. When the strip resistivity is close to 0, then ω should be small. As the strip resistivity increases, then the value of ω should also increase. Some approximate formula for finding a good value for ω given the strip resistivity of the strip and the size of the matrix could probably be found, but is not pursued here. This method is more stable than relaxation and faster than conjugate gradient, but still requires calculating a value for ω.

Conjugate gradient is slower than relaxation or Steffensen's acceleration, but is guaranteed to converge in N steps and does not require the calculation of ω. A conjugate gradient FFT method [Sarkar, Arvas, and Rao, 1986] is very attractive for large matrices, because it has all the advantages of conjugate gradient plus significant savings in storage requirements.

2.4 Calculating the Radar Cross-Section (RCS) of a Strip

The scattering patterns of the current distributions are found from (2.1-10) and (2.1-14). In the far field ($\rho >> x'$), the Hankel functions in these equations may be replaced by the following large argument approximations [Abramowitz and Stegen, 1972]:

$$H_o^{(2)}(k|\rho - x'|) = e^{j\frac{\pi}{4}}(.5\pi k|\rho - x'|)^{-\frac{1}{2}} e^{jk|\rho - x'|} \qquad (2.4\text{-}1)$$

$$H_1^{(2)}(k|\rho - x'|) = e^{j\frac{3\pi}{4}}(.5\pi k|\rho - x'|)^{-\frac{1}{2}} e^{jk|\rho - x'|} \qquad (2.4\text{-}2)$$

A two-dimensional bistatic radar cross section is calculated from

$$\sigma(\phi) = \lim_{\rho \to \infty} 2\pi\rho \left| \frac{E^s(\phi)}{E^i(\phi_o)} \right|^2 \tag{2.4-3}$$

which for E- and H-polarizations are

$$\sigma_E(\phi) = \frac{k}{4H_o^2} \left| \int_{-a}^{a} J_z(x')e^{jkx'\cos\phi}dx' \right|^2 \tag{2.4-4}$$

$$\sigma_H(\phi) = \frac{k}{4H_o^2} \left| \sin\phi \int_{-a}^{a} J_x(x')e^{jkx'\cos\phi}dx' \right|^2 \tag{2.4-5}$$

Backscattering RCS assumes $\phi = \phi_o$ in these equations. Consequently, a new strip current density is calculated at every angle.

Ordinarily, RCS is given in units of dBsm (decibels above one square meter) or in the case of a 2-dimensional RCS in dBm (decibels above one meter). Throughout the following chapters the units of RCS for the strip are given in terms of dBλ (decibels above one wavelength). This type of designation keeps the RCS independent of frequency. Since the RCS is independent of the magnitude of the incident field, H_o is given the value of 1.0. As a result, the RCS equations in dBλ are given by

$$\sigma_E(\phi) = 1.961 + 10log\left[\left| \int_{-a}^{a} J_z(x')e^{jkx'\cos\phi}dx' \right|^2 \right] \quad dB\lambda \tag{2.4-6}$$

$$\sigma_H(\phi) = 1.961 + 10log\left[\left| \sin\phi_o \int_{-a}^{a} J_x(x')e^{jkx'\cos\phi}dx' \right|^2 \right] \quad dB\lambda \tag{2.4-7}$$

CHAPTER III

SYNTHESIS OF RESISTIVE TAPERS

The major goal of this thesis is to develop a method of synthesizing resistive tapers that produce desired scattering patterns from strips. Only simple tapers, such as parabolic and edge loading, have been reported in the past. Although these simple tapers do lower the scattering pattern sidelobes, they do not provide precise control over the scattering patterns as antenna aperture tapers provide over an antenna's far field pattern.

An extremely effective synthesis procedure for resistive tapers comes from solving the integral and PO equations for η. Values for η is calculated by substituting a current distribution with known far field pattern characteristics into the equations. The integral equation approach is very accurate, but is complicated to generate and requires a complex strip resistivity. The PO approach is not as accurate, but is relatively fast and produces a real strip resistivity.

This chapter begins with an analysis of simple resistive tapers then moves on to describe the integral equation and PO synthesis techniques for resistive tapers. Next, the Taylor current taper that results in a far field pattern with low sidelobes at desired levels is presented. Finally, the Steyskal-Shore null synthesis technique is presented in a form that generates a current distribution that produces nulls in the scattering pattern. This current distribution is related to a resistive taper via the integral equation method, since the resistive taper has real and imaginary parts. The resistive tapers derived from these current tapers produce the desired far field scattering patterns from a strip.

The figures throughout this chapter contain four graphs: 1) normalized strip resistivity on the strip, 2) strip current density, 3) bistatic scattering pattern for $\phi_o = 90°$, and 4)

backscattering pattern. When appropriate, each graph has two plots: one for PO and one for the integral equation approach. The close correspondence between the two plots demonstrates the validity of the PO synthesis technique.

3.1 Tapering the Strip Resistivity for Low Sidelobes

Past attempts at controlling the scattering patterns from resistive strips include constant and parabolic resistive tapers and edge loading. These forms of resistive tapers do not provide precise control over the sidelobe level or null locations of far field scattering patterns. Although superior techniques are presented later, the tapers presented in this section are the state-of-the-art.

3.1.1 Resistive Tapers

A strip with a uniform resistive taper

$$R(x) = r \qquad (3.1\text{-}1)$$

has a lower over-all scattering pattern than a perfectly conducting strip, because some of the incident field energy is converted into heat instead of current. The sidelobe levels do go down with this taper, but not relative to the main beam. Thus, a constant taper that lowers the sidelobes by 20dB also lowers the main beam by approximately the same amount.

Figures 3.1 and 3.2 contain graphs of the calculated strip current density and scattering patterns for a 4λ perfectly conducting strip for E- and H-polarization, respectively. The PO and integral equation plots show good agreement except in the nulls of the PO patterns and at angular locations far from the main beam. However, when $\eta=1$, the two currents and corresponding scattering patterns agree much better (Figures 3.3 and 3.4). As the strip resistivity increases, the two current plots agree even more closely. Figure 3.5b demonstrates the increased correspondence between the two currents for an E-polarized incident wave with $\eta=4.0$. Notice that the relative sidelobe level of the scattering patterns remains the same as the strip resistivity increases (Figures 3.5c and 3.5d).

The relative sidelobe level may be lowered by tapering the strip resistivity from a minimum at the center of the strip to a maximum at the edges. In turn, the current decreases from the center to the edges, thus lowering the sidelobes. One possible taper is
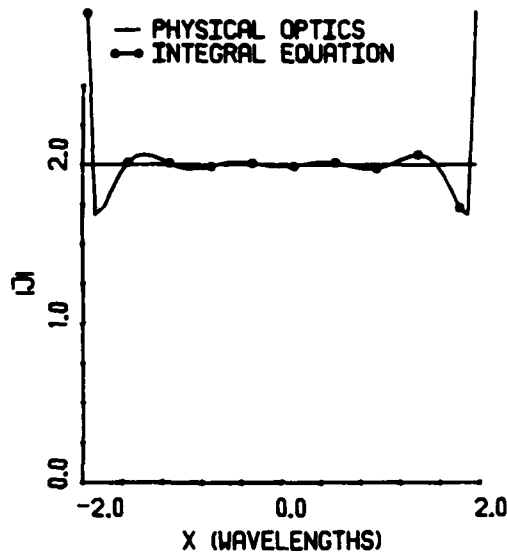
a. Magnitude of induced surface
current density on strip, ϕ_o=90°
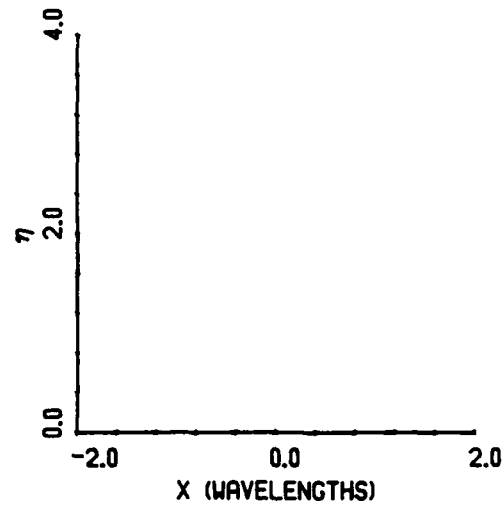
b. Normalized resistivity on strip
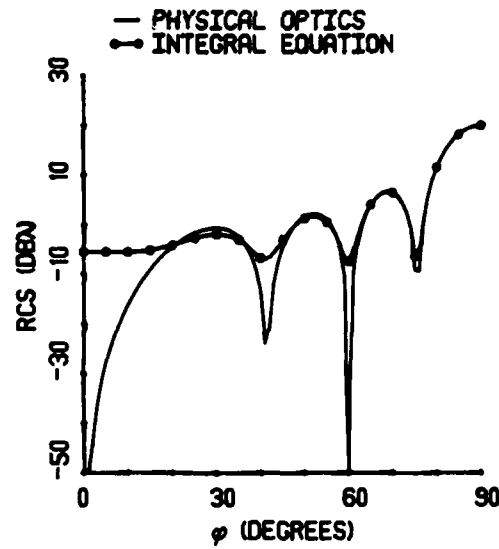
c. Bistatic scattering pattern, φ_o=90°

d. Backscattering pattern

Figure 3.1 — E-polarized computed scattering results for a 4λ perfectly conducting strip

a. Magnitude of induced surface current density on strip, $\phi_o = 90°$

b. Normalized resistivity on strip

c. Bistatic scattering pattern, $\varphi_o = 90°$

d. Backscattering pattern

Figure 3.2 — H-polarized computed scattering results for a 4λ perfectly conducting strip

a. Magnitude of induced surface
current density on strip, ϕ_o=90°

b. Normalized resistivity on strip

c. Bistatic scattering pattern, φ_o=90°

d. Backscattering pattern

Figure 3.3 — E-polarized computed scattering results for a 4λ resistive strip with $\eta = 1.0$

— PHYSICAL OPTICS
•—• INTEGRAL EQUATION

a. Magnitude of induced surface
current density on strip, ϕ_o=90°

b. Normalized resistivity on strip

— PHYSICAL OPTICS
•—• INTEGRAL EQUATION

— PHYSICAL OPTICS
•—• INTEGRAL EQUATION

c. Bistatic scattering pattern, ϕ_o=90°

d. Backscattering pattern

Figure 3.4 — H-polarized computed scattering results for a 4λ resistive strip with $\eta = 1.0$

a. Magnitude of induced surface current density on strip, $\phi_\circ$=90°

b. Normalized resistivity on strip

c. Bistatic scattering pattern, $\varphi_\circ$=90°

d. Backscattering pattern
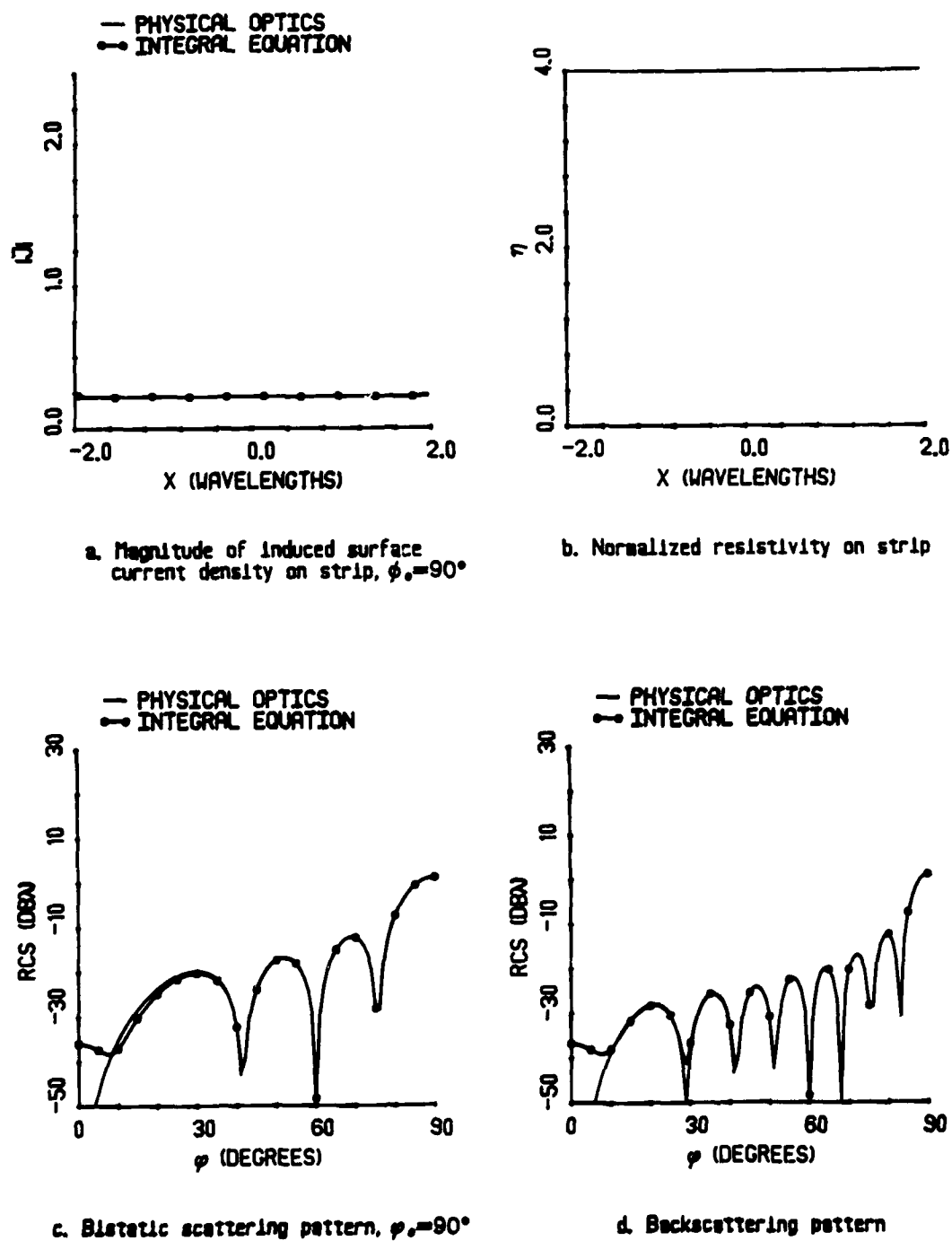
Figure 3.5 — E-polarized computed scattering results for a 4λ resistive strip with $\eta = 4.0$

$$R(x) = r + b\left|\frac{x}{a}\right|^c \tag{3.1-2}$$

where r, b, and c are constants and 2a is the width of the strip. When c=1, the taper is triangular, and when c=2 the taper is parabolic.

Figures 3.6 and 3.7 show the scattering results of a parabolic taper when an E-polarized plane wave is incident on the strip. The smooth resistive taper produces a smooth current taper that lowers the sidelobe level. Increasing the resistive taper by changing b from 1.0 to 4.0, causes the relative sidelobe level to go up close to the main beam but down far from the main beam (Figure 3.7). Another consequence is the main beam gets fatter and its level goes down.

A third type of taper has a gaussian shape

$$R(x) = r + b[1 - e^{(2cx/a)^2}] \tag{3.1-3}$$

This taper is attractive because of its smoothness (It has an infinite number of non-zero derivatives.). Figures 3.8 and 3.9 show E-polarized results as b increases from 1.0 to 4.0. These results look similar to the results from the parabolic taper. A slowly varying taper as in Figures 3.6 or 3.8 produces a very nice scattering pattern with low sidelobes. A very steep taper as in Figures 3.7 and 3.9 produces a pattern with a wide main beam and high sidelobes near the main beam but low sidelobes far from the main beam.

3.1.2 Edge Loading

Edge loading, the final type of resistive taper considered, terminates a conductive strip with a resistive load a distance q from each edge. The purpose of edge-loading is to mask the edge contribution to the scattering pattern. In effect, the load provides a transition from the perfectly conducting strip with R=0 to free space with R=∞. The length and the resistivity level of the load determines how smoothly the transition takes place. A perfect match would occur when the discontinuities on the strip are transparent. At that time the integral equation and PO current and bistatic scattering pattern for a given angle would be identical.

A careful choice of the length and strip resistivity of the loads can alter the scattering patterns in desirable ways. A small constant resistive strip added to the edges of a perfectly
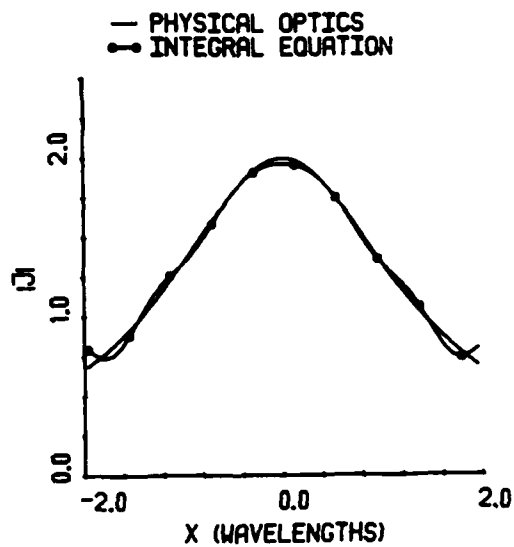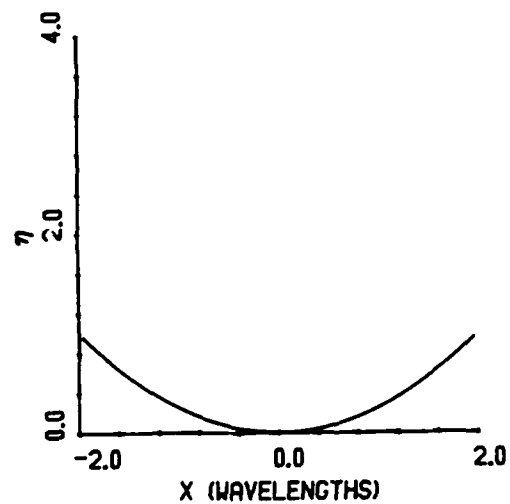
— PHYSICAL OPTICS
— INTEGRAL EQUATION

a. Magnitude of induced surface
current density on strip, $\phi_o = 90°$

b. Normalized resistivity on strip

— PHYSICAL OPTICS
— INTEGRAL EQUATION

— PHYSICAL OPTICS
— INTEGRAL EQUATION
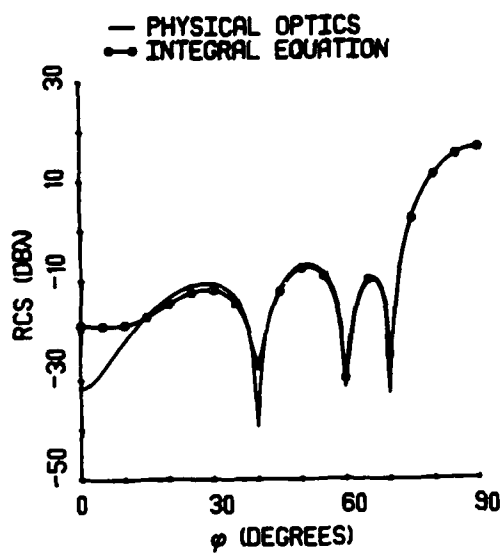
c. Bistatic scattering pattern, $\varphi_o = 90°$
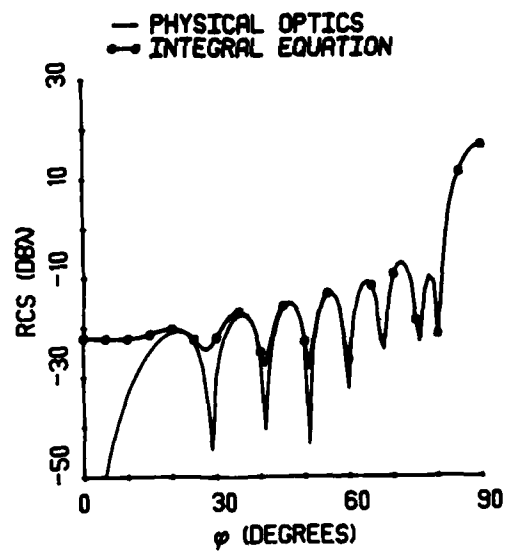
d. Backscattering pattern

Figure 3.6 — E-polarized computed scattering results for a 4λ resistive strip with
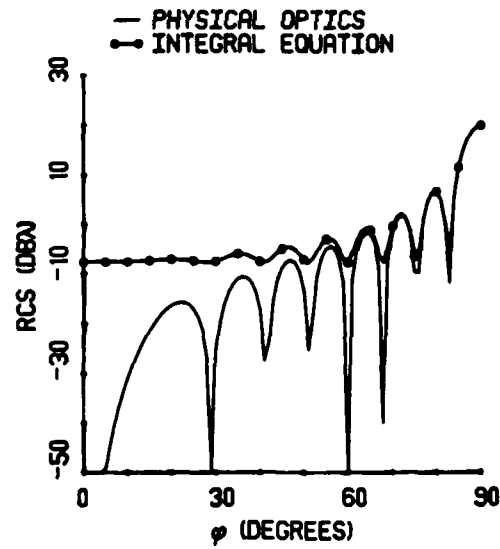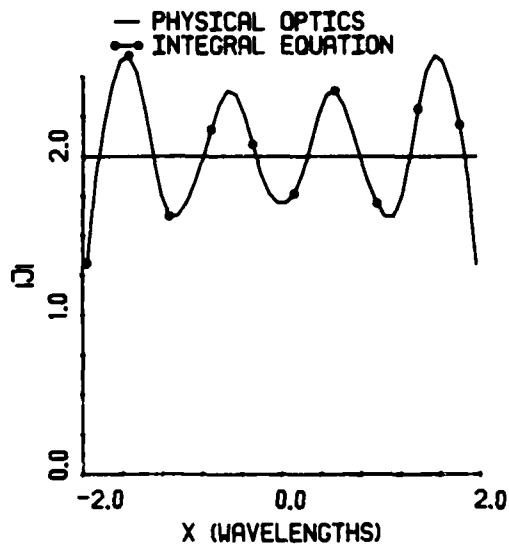
$$\eta = \left(\frac{X}{a}\right)^2$$

a. Magnitude of induced surface
current density on strip, ϕ_o=90°

b. Normalized resistivity on strip
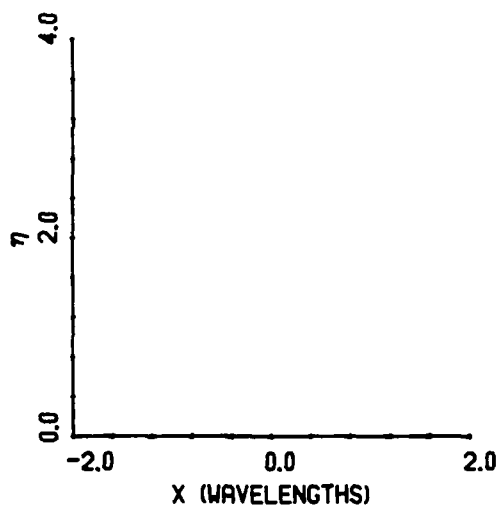
c. Bistatic scattering pattern, φ_o=90°

d. Backscattering pattern
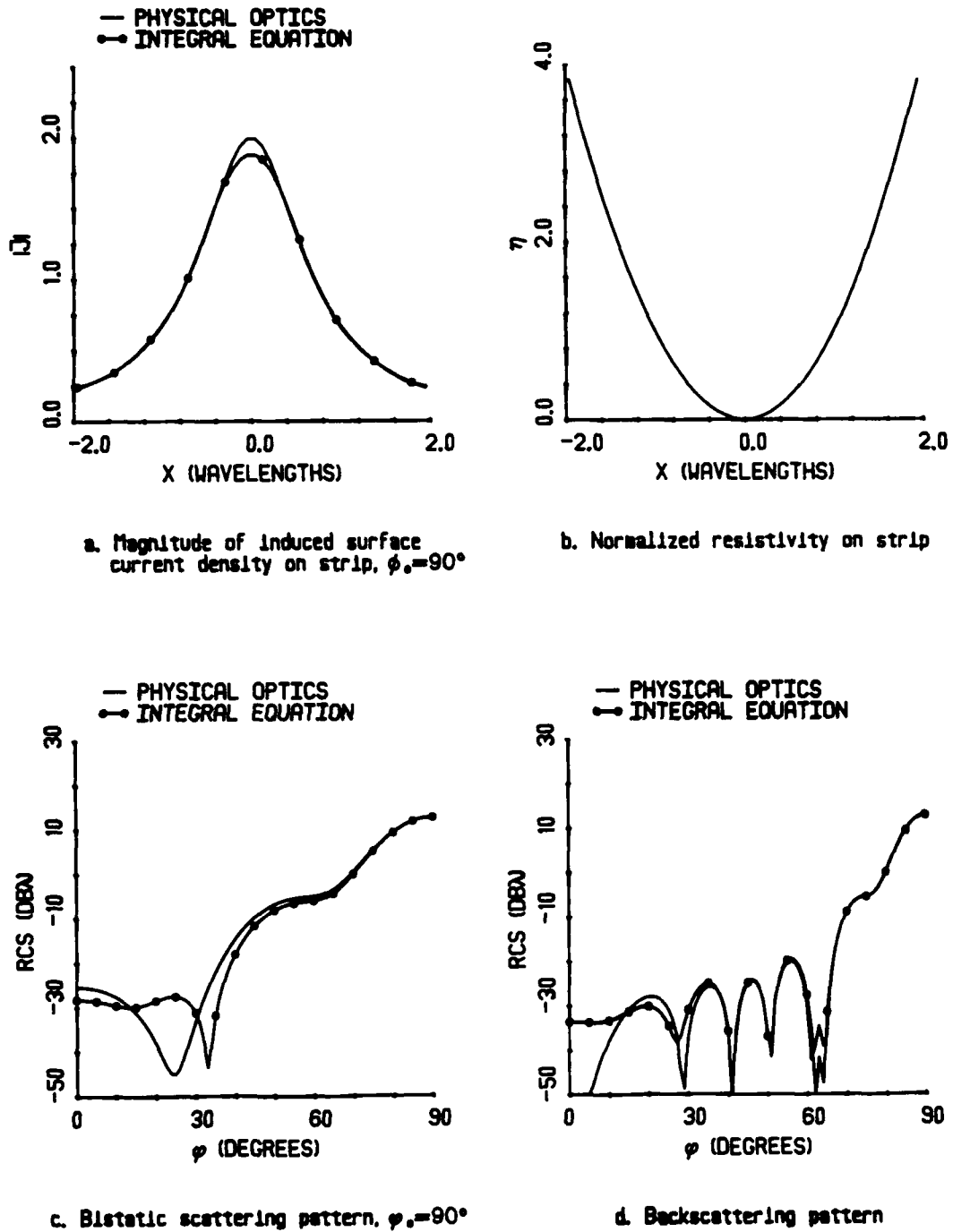
Figure 3.7 — E-polarized computed scattering results for a 4λ resistive strip with

$$\eta = 4(\tfrac{X}{a})^2$$

a. Magnitude of induced surface current density on strip, ϕ_o=90°

b. Normalized resistivity on strip

c. Bistatic scattering pattern, φ_o=90°

d. Backscattering pattern
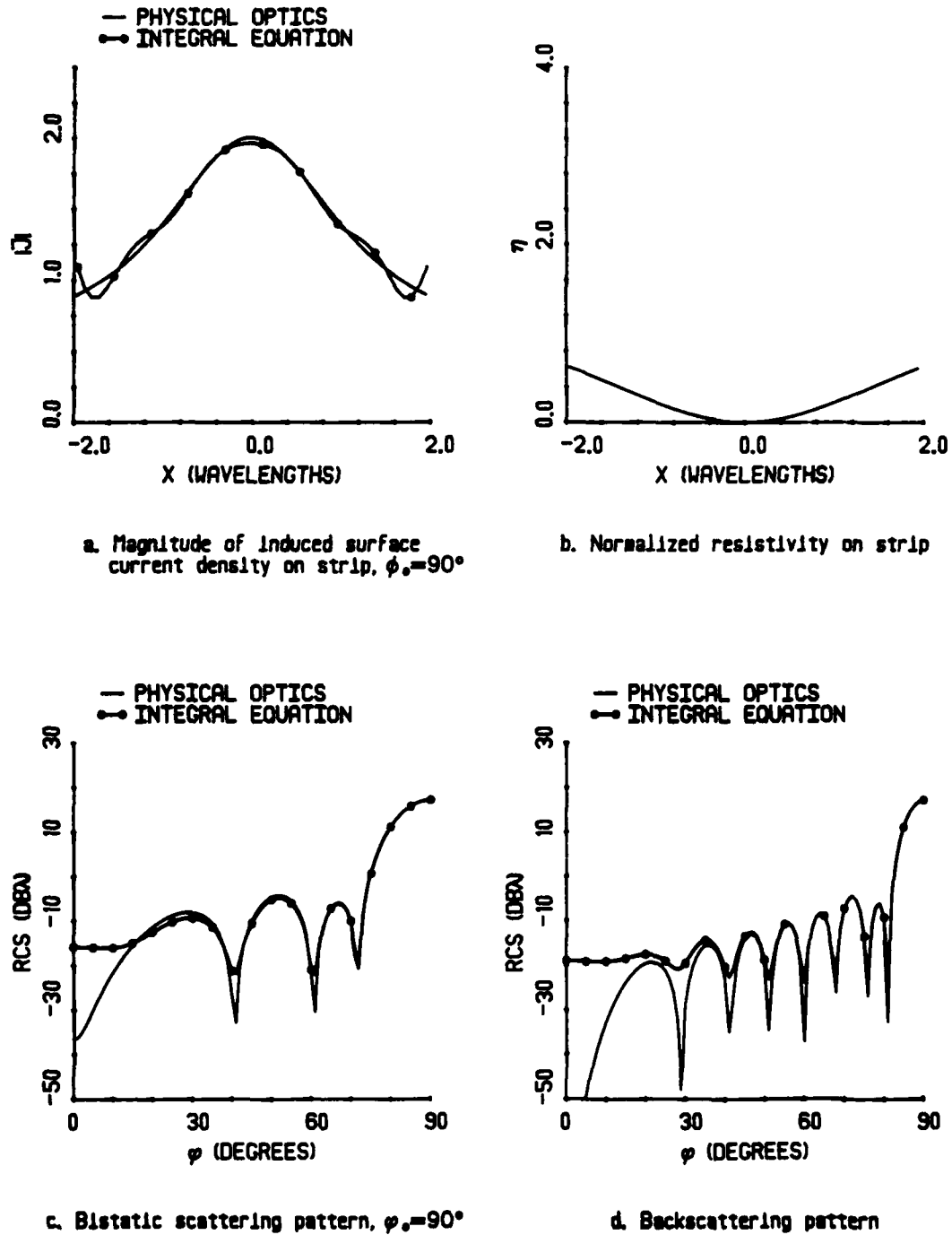
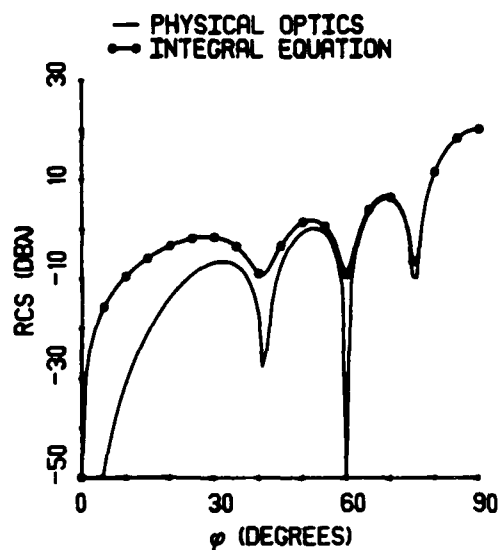Figure 3.8 — E-polarized computed scattering results for a 4λ resistive strip with
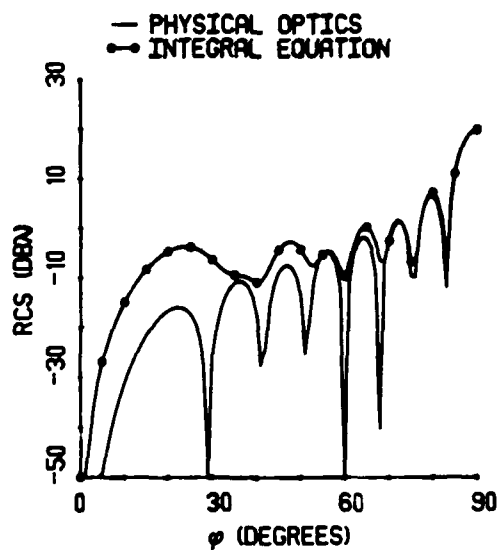
$$\eta = 1 - e^{(2x/a)^2}$$
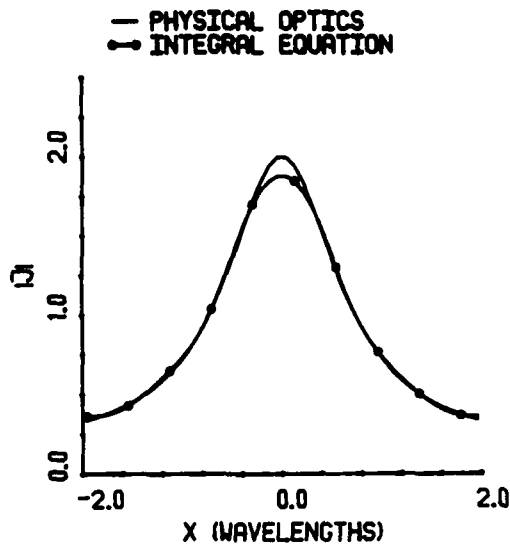
a. Magnitude of induced surface
current density on strip, $\phi_o = 90°$
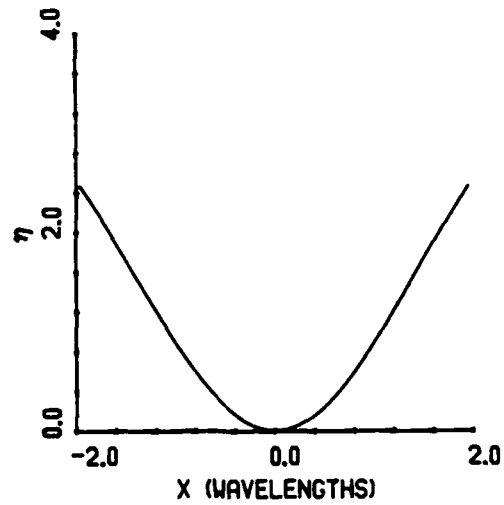
b. Normalized resistivity on strip
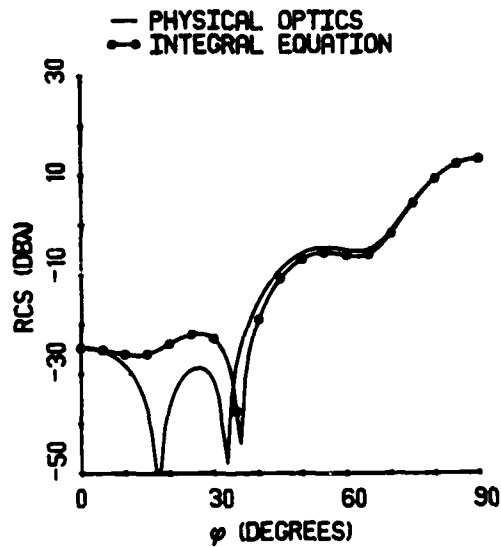
c. Bistatic scattering pattern, $\varphi_o = 90°$
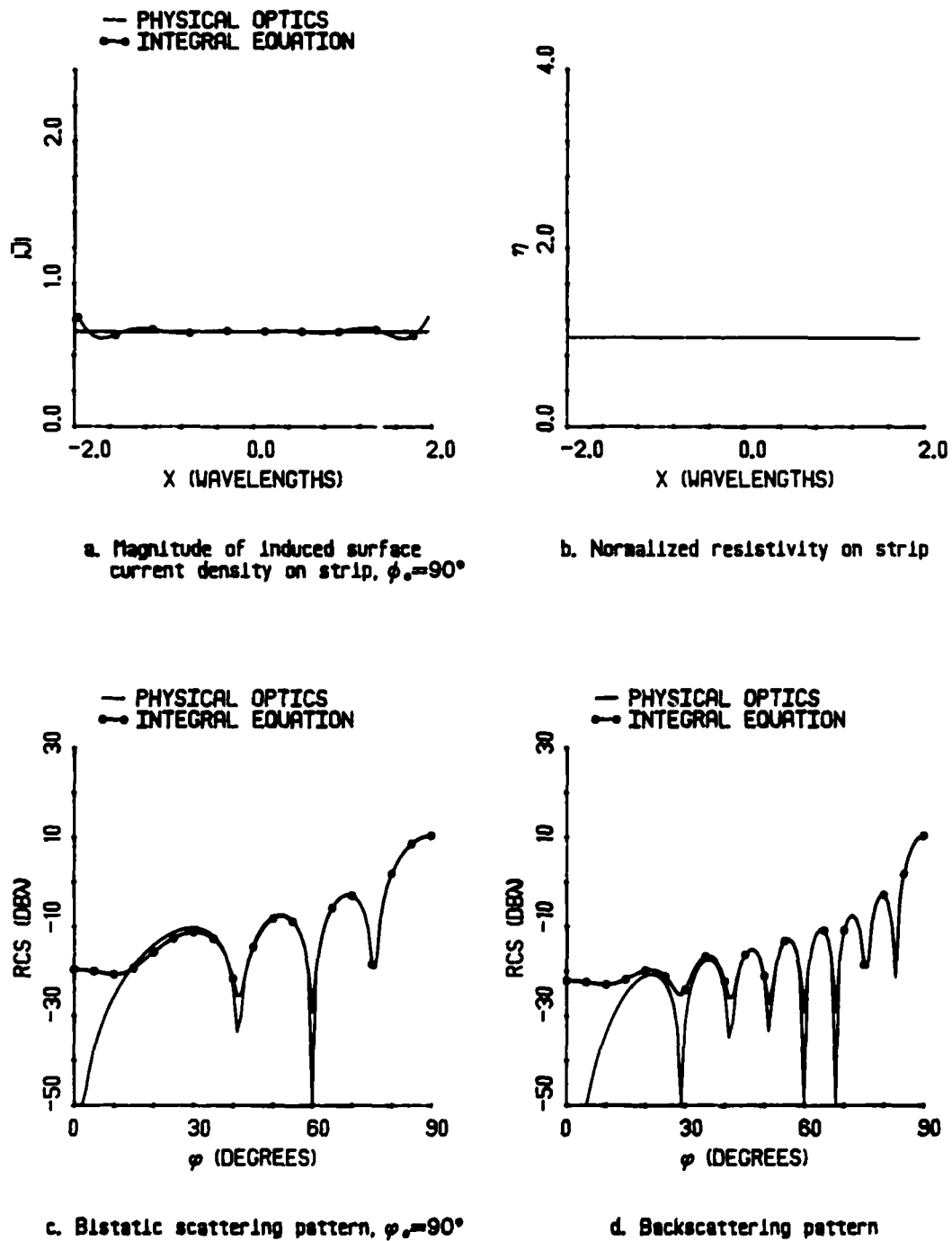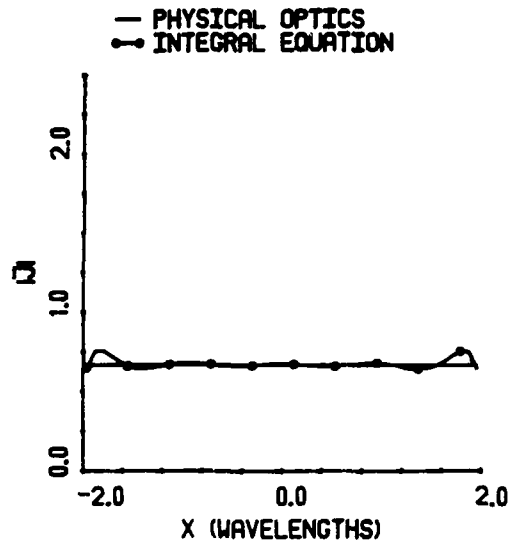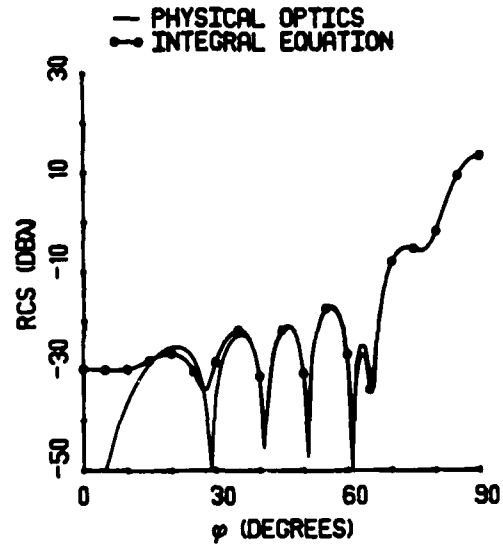
d. Backscattering pattern

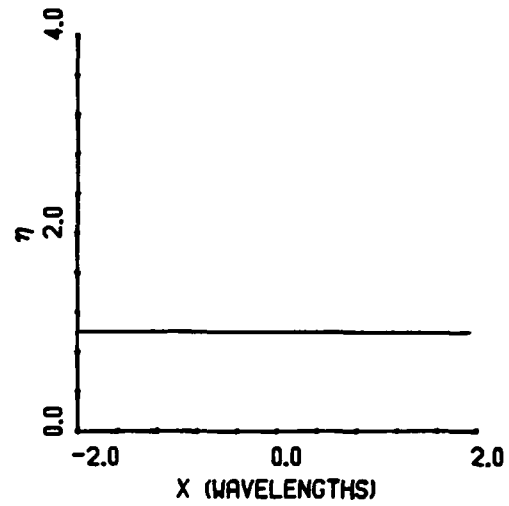Figure 3.9 — E-polarized computed scattering results for a 4λ resistive strip with

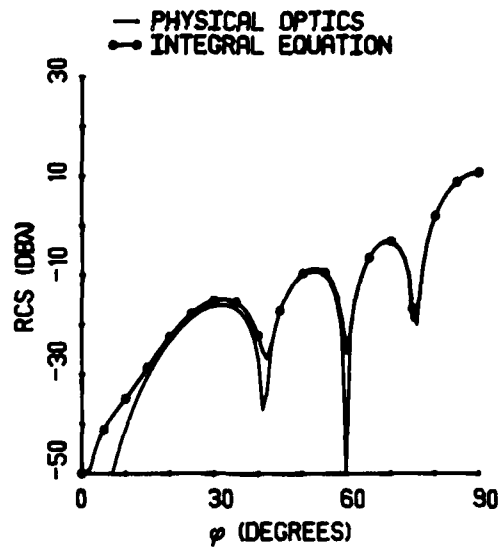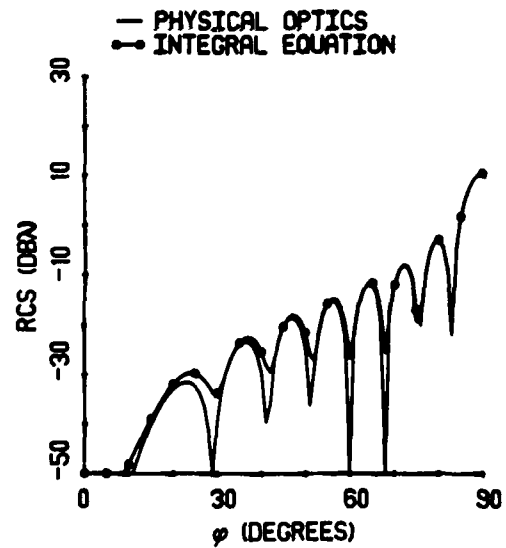$$\eta = 4[1 - e^{(2x/a)^2}]$$

conducting strip lowers the scattering sidelobe level. Increasing the value of the resistive load beyond a certain value actually raises the sidelobe level, because the scattering contributions from the loads become very small relative to the contribution from the conducting part of the strip. At a very high value of strip resistivity, the edge loads have no effect on the scattering patterns and the strip has the scattering patterns of a perfectly conducting strip $2(a - q)$ long.

Figure 3.10 shows the E-polarized plots for a 4λ strip having constant edge loads of $\eta = .5$ a distance of $.5\lambda$ from the edges. Compared with Figure 3.1, the scattering sidelobes from this strip are lower, but the scattering mainbeam does not change much. Figure 3.11 shows the results when the strip resistivity of the load is increased to $\eta = 1.5$. Notice that the width of the main beam increases and the outer sidelobe level goes up compared to Figure 3.10.

Grating lobes occur in the scattering patterns of an edge-loaded strip, just as they do in antenna theory. Consider an 8λ wide strip, perfectly conducting at the center, and constant resistive loads ($\eta=1.0$) 2.0λ from either edge. Grating lobes in the bistatic scattering pattern are given by Mailloux's formula [1984] for grating lobes in a subarrayed phased array

$$\phi_p = cos^{-1}\left[\frac{p}{q}\right], \quad p = \pm(1, 2, ..., q) \tag{3.1-4}$$

or $\phi_p = 60°$ and $90°$. Figure 3.12c confirms this prediction. Backscattering grating lobes occur twice as often as the bistatic grating lobes and are predicted from

$$\phi_p = cos^{-1}\left[\frac{p}{2q}\right], \quad p = \pm(1, 2, ..., 2q) \tag{3.1-5}$$

or $\phi_p = 75.52°, 60°, 41.41°$, and $90°$. Figure 3.12d confirms this prediction.

In order to reduce the abrupt discontinuity at the resistive loads and prevent the formation of grating lobes, the resistive load can be tapered from a small value of strip resistivity at the conductive part to a large value at the edge. Tapering the subarrays of a phased array has also been suggested to eliminate grating lobes [Haupt, 1985]. Figures 3.13 and 3.14 show the dramatic improvement to the scattering patterns when the resistive load has a quadratic taper rather than a constant strip resistivity. The smooth transition between

a. Magnitude of induced surface
   current density on strip, $\phi_o = 90°$

b. Normalized resistivity on strip

c. Bistatic scattering pattern, $\varphi_o = 90°$

d. Backscattering pattern

Figure 3.10 — E-polarized computed scattering results for a 4λ strip with loads of $\eta = .5$ a distance of 1.0λ from the edges

a. Magnitude of induced surface current density on strip, ϕ_o=90°

b. Normalized resistivity on strip

c. Bistatic scattering pattern, φ_o=90°

d. Backscattering pattern

Figure 3.11 — E-polarized computed scattering results for a 4λ strip with loads of $\eta = 1.5$ a distance of 1.0λ from the edges

a. Magnitude of induced surface
current density on strip, $\phi_o=90°$
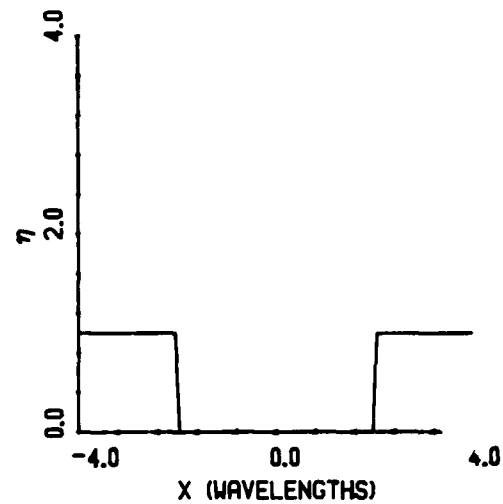
b. Normalized resistivity on strip
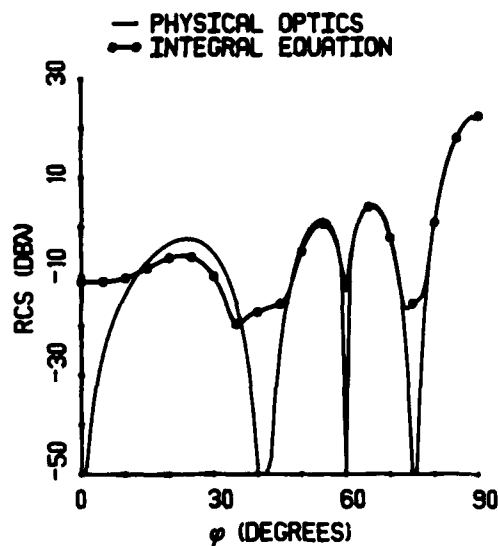
c. Bistatic scattering pattern, $\varphi_o=90°$
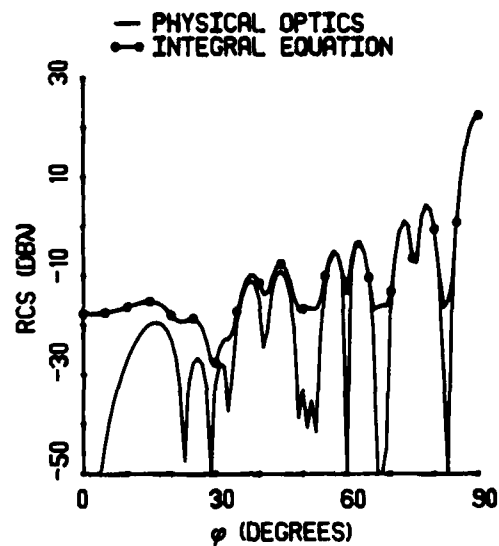
d. Backscattering pattern

Figure 3.12 — E-polarized computed scattering results for an 8λ strip with loads of
$\eta = 1.0$ a distance of 2.0λ from the edges

the perfectly conducting strip and its load reduces the current spikes at the discontinuity which in turn reduces the scattering sidelobes. Figure 3.13 has a taper $\eta = \left(\frac{x}{a}\right)^2$ a distance of 1λ from either edge. No grating lobes appear in the scattering patterns and the outer sidelobes are about 5 dB lower than those of a perfectly conducting strip. Figure 3.14 has a taper $\eta = 4\left(\frac{x}{a}\right)^2$ a distance of 1λ from either edge. Again, no grating lobes appear in the scattering patterns and the outer sidelobes are about 15 dB lower than those of a perfectly conducting strip.

3.2 Synthesizing a Resistive Taper

The examples of resistive tapers in the last section demonstrate that some control over the scattering patterns is possible. Ultimately, one wishes to synthesize a resistive taper from any current distribution on the strip that leads to a desired scattering pattern. Antenna theory provides many types of synthesis techniques for relating desired far field pattern characteristics to the aperture taper of the antenna. Another step is needed in scattering theory that relates the current taper to the resistive taper.

The objective here is to develop a synthesis technique for relating a current distribution to a strip resistivity distribution on the strip, then borrow one of the many synthesis techniques that already exists for relating the desired far field pattern characteristics to a current taper. This chapter presents two techniques for synthesizing a resistive taper. The first solves the integral equations for the strip resistivity. This method is more exact than PO but requires complex resistivities. The second solves the PO equations for the strip resistivity. This method is not as accurate as the integral equation approach but only requires real valued resistivities.

3.2.1 Synthesis of a Resistive Taper from the Integral Equations

The strip resistivity for a given current distribution may be found by solving (2.1-11) or (2.1-15) for η.

E-polarization:

$$\eta(x) = \frac{1}{J_z(x)}\left[e^{jkx\cos\,\phi_o} - \frac{k}{4}\int_{-a}^{a} J_z(x')H_o^{(2)}(k|x - x'|)dx'\right] \tag{3.2-1}$$

H-polarization:

— PHYSICAL OPTICS
•— INTEGRAL EQUATION

a. Magnitude of induced surface
current density on strip, ϕ_o=90°

b. Normalized resistivity on strip

— PHYSICAL OPTICS
•— INTEGRAL EQUATION

— PHYSICAL OPTICS
•— INTEGRAL EQUATION

c. Bistatic scattering pattern, φ_o=90°

d. Backscattering pattern
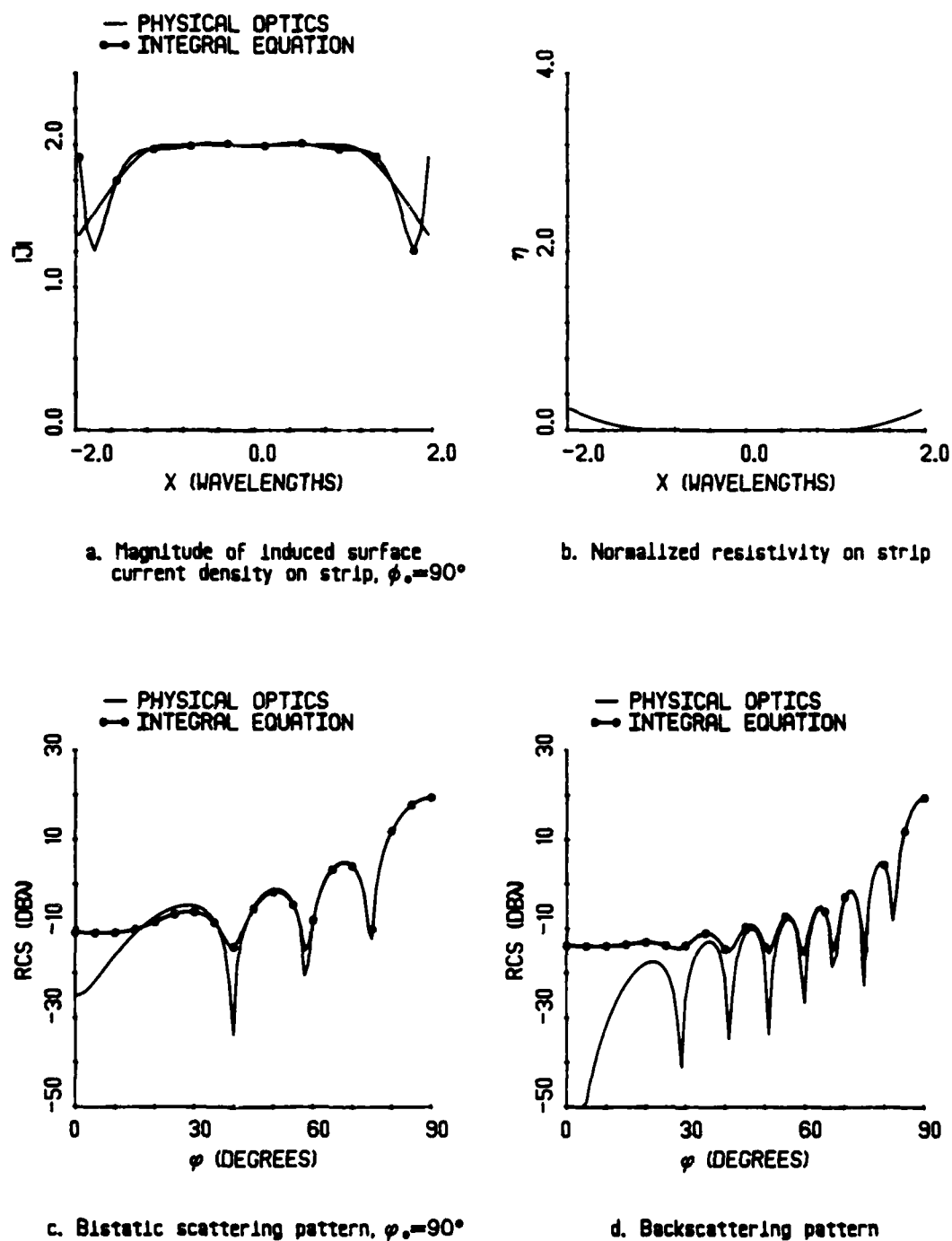
Figure 3.13 — E-polarized computed scattering results for a 4λ strip with loads of

$$\eta = \left(\frac{x}{a}\right)^2 \text{ a distance of } 1.0\lambda \text{ from the edges}$$
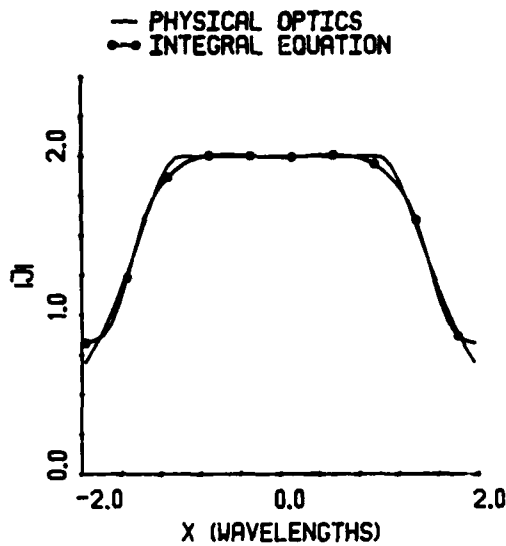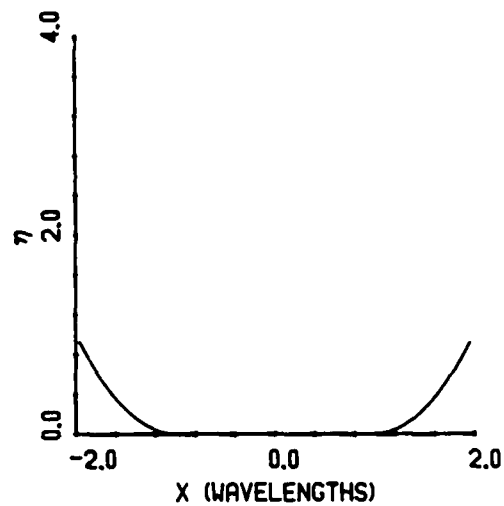
— PHYSICAL OPTICS
•—• INTEGRAL EQUATION

a. Magnitude of induced surface
current density on strip, $\phi_o=90°$

b. Normalized resistivity on strip
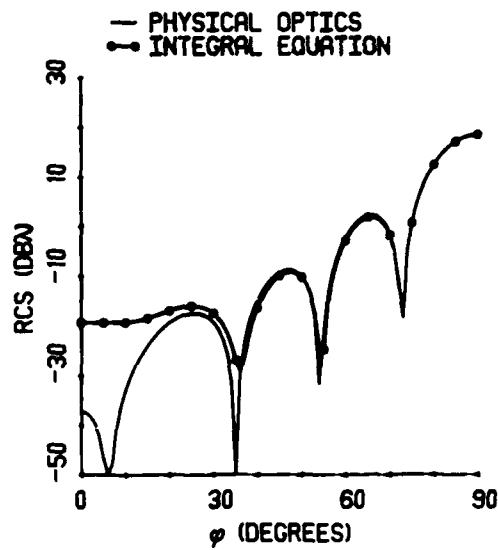
c. Bistatic scattering pattern, $\varphi_o=90°$
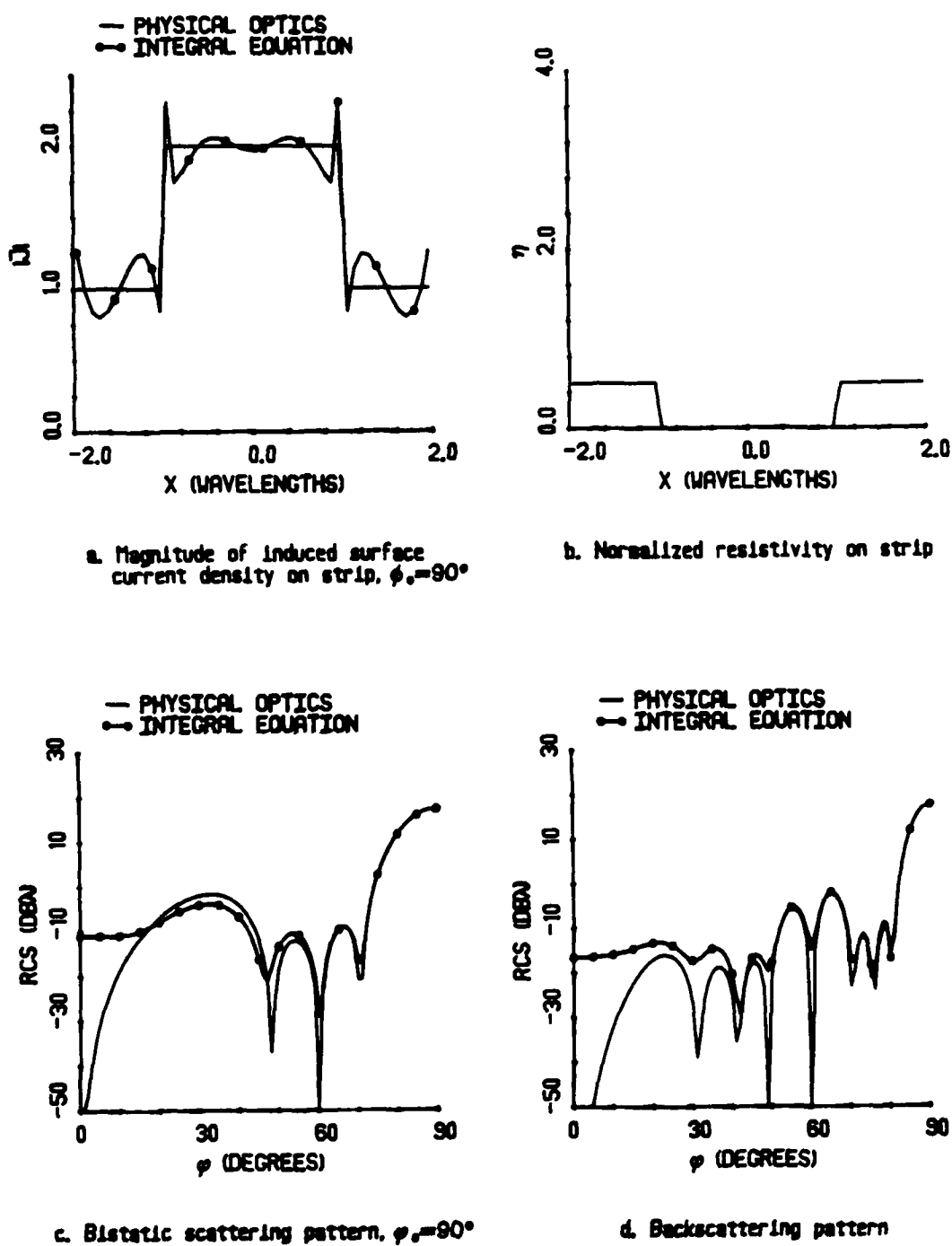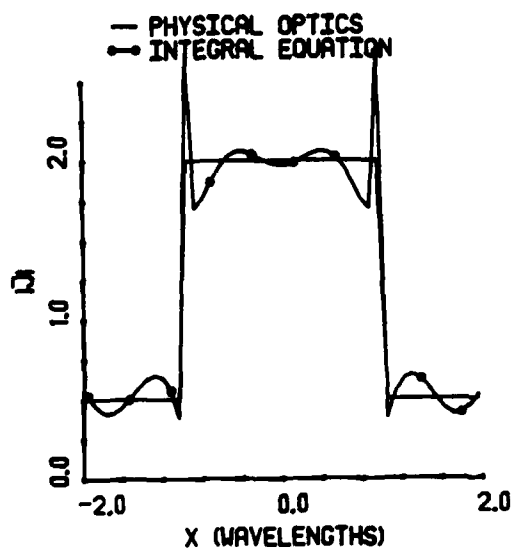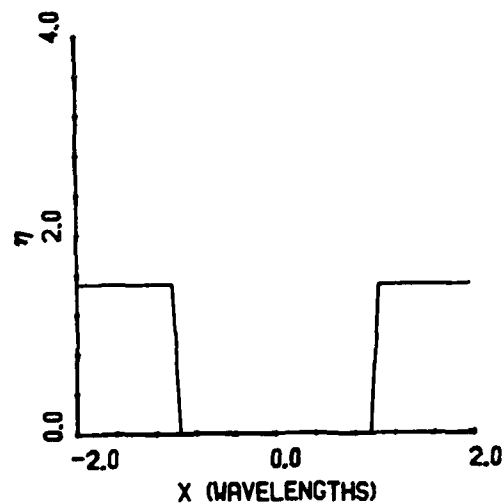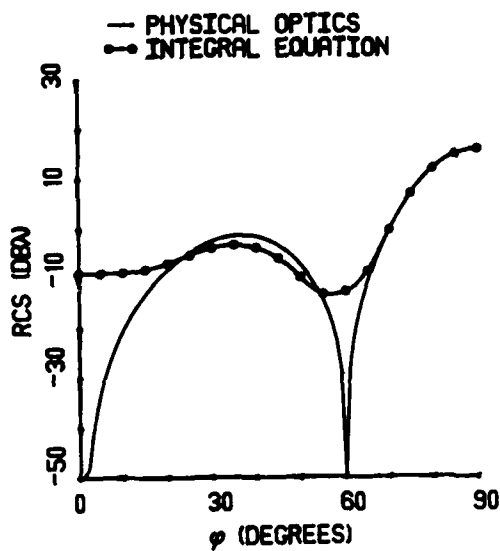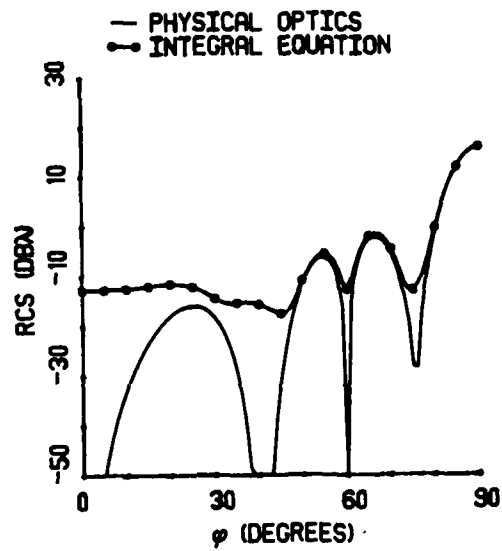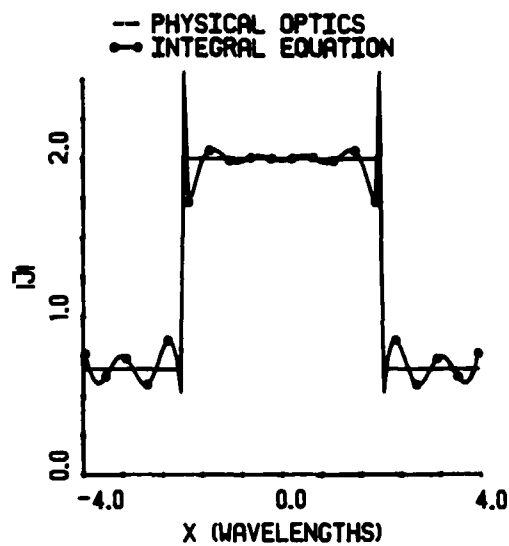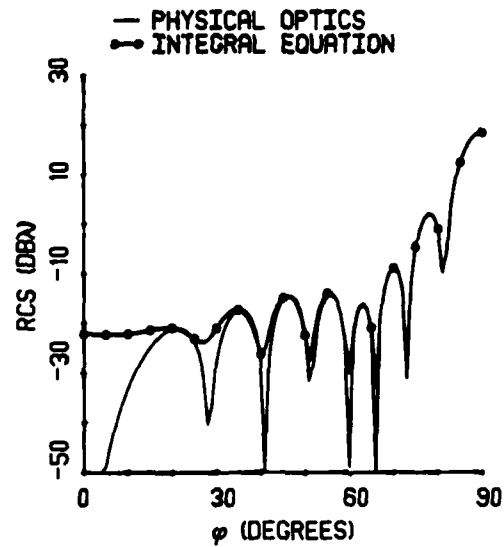
d. Backscattering pattern

Figure 3.14 — E-polarized computed scattering result for a 4λ strip with loads of $\eta = (\frac{z}{a})^2$ a distance of 1.0λ from the edges

$$\eta(x) = \frac{1}{J_x(x)}\left[\sin\phi_o e^{jkx\cos\phi_o} - \frac{k}{4}\int_{-a}^{a}J_x(x')\frac{1}{k|x-x'|}H_1^{(2)}(k|x-x'|)dx'\right] \qquad (3.2\text{-}2)$$

The current distributions come from synthesis techniques in antenna theory (see sections 3.3 and 3.4). If the same numerical integration techniques used to evaluate the current in (3.2-1) and (3.2-2) as are used to evaluate the current in (2.1-11) and (2.1-15), then the exact desired current will be found when solving (2.1-11) and (2.1-15).

The strip resistivity derived in this manner is a complex value, which means that not only does the conductivity of the strip vary, but the real part of ϵ must vary too. As such, a resistive strip can no longer be modeled by a substrate with an $\epsilon \approx \epsilon_o$ that is coated with a conductive material. Instead, the real part of the dielectric constant of the substrate must also vary as a function of position. Some scattering pattern characteristics, for instance placing a null at a desired angle, are obtained only through modifying the amplitude and phase of the strip current. Complete control over the amplitude and phase of the strip current is only possible through a complex strip resistivity. A variable complex strip resistivity is much more difficult to manufacture than a strip resistivity with a variable real part and a constant imaginary part. Fortunately, the imaginary part of the resistive taper is often quite small, as in many low sidelobe tapers. In that case, either the magnitude or the real part of the resistive taper is sufficient to elicit the desirable characteristics in the scattering pattern.

3.2.2 Synthesis of a Resistive Taper from Physical Optics

An alternative to solving the integral equations for η, is to solve the PO equations for η. This alternative has its roots in inverse scattering. Boerner [1980], for example, suggests that PO is the most reasonable approach to inverse scattering problems. He does caution that PO has limitations such as

1. PO applies to targets with metallic surfaces.
2. PO approximation gets worse as bistatic angle increases.
3. PO does not account for multiple reflections.
4. PO does not account for creeping waves.

These limitations can be severe for metallic strips. However, as shown in Chapter II, PO equations also exist for non-metallic surfaces. Although these equations do not account

for multiple reflections from the edges or creeping waves, a smoothly tapered strip resistivity considerably reduces these effects. Also, the smoothly tapered strip resistivity extends the accuracy of PO in the bistatic scattering pattern to angles closer to the edges.

The strip resistance is found by solving (2.1-28) and (2.1-29) for $\eta(x)$.

E-polarization:

$$\eta = \frac{1}{J_z(x)} e^{jkx\cos \phi_o} - \frac{1}{2\sin\phi_o} \qquad (3.2\text{-}3)$$

H-polarization:

$$\eta = \frac{\sin\phi_o}{J_x(x)} e^{jkx\cos\phi_o} - \frac{\sin\phi_o}{2} \qquad (3.2\text{-}4)$$

Within the limits of accuracy of the PO, these values of $\eta(x)$ produce the desired strip currents which in turn produce the desired scattering pattern. The advantage of using this technique is quite apparent: it is easy to calculate $\eta(x)$ compared to the integral equation approach.

3.2.3 Relating the Desired Current to the Strip Resistivity

It is logical to assume that $\phi_o = 0$ in the synthesis equations, otherwise an unnecessary phase shift is required in the current, which means the strip resistivity derived from the integral equation and PO approaches must be complex. These equations now take the form

E-polarization integral equation:

$$\eta(x) = \frac{1}{J_z(x)} - \frac{k}{4} \int_{-a}^{a} J_z(x') H_o^{(2)}(k|x - x'|) dx' \qquad (3.2\text{-}5)$$

H-polarization integral equation:

$$\eta(x) = \frac{1}{J_x(x)} - \frac{k}{4} \int_{-a}^{a} J_x(x') \frac{1}{k|x - x'|} H_1^{(2)}(k|x - x'|) dx' \qquad (3.2\text{-}6)$$

E- or H- polarization PO equation:

$$\eta(x) = \frac{1}{J_s(x)} - \frac{1}{2} \qquad (3.2\text{-}7)$$

Observe that the leading terms in these three equations are identical and that the PO equation is the same for both polarizations. If the first terms are dominant, then the three

equations give nearly the same result. Consequently, the synthesis techniques are relatively independent of the polarization!

When the resistive taper is first computed, it may have negative or exceptionally high values. To eliminate any negative real values of strip resistivity, the taper is normalized by following these steps:

1. Find the smallest value of strip resistivity in the taper and its location, x_{min}.

2. Assume the minimum strip current density, $J_s(x_{min})$, occurs at this point.

3. Specify the minimum value of the strip resistivity, η_{min}. η_{min} is typically 0.0.

4. Find a real conversion constant, γ, such that γ produces a current $\gamma J_s(x_{min})$ at the point x_{min}. γ is given by one of the following equations:

PO:

$$\gamma = Real\left\{ \frac{1}{J_s(x_{min})[\eta_{min} + 0.5]} \right\} \qquad (3.2\text{-}8)$$

Integral Equation E-polarization:

$$\gamma = Real\left\{ \frac{1}{J_z(x_{min})\eta_{min} + \frac{k}{4}\int_{-a}^{a} J_z(x')H_o^{(2)}(k|x - x'|)dx'} \right\} \qquad (3.2\text{-}9)$$

Integral Equation H-polarization:

$$\gamma = Real\left\{ \frac{1}{J_x(x_{min})\eta_{min} + \frac{k}{4}\int_{-a}^{a} J_x(x')\frac{1}{k|x-x'|}H_1^{(2)}(k|x - x'|)dx'} \right\} \qquad (3.2\text{-}10)$$

5. Multiply the derived current distribution by γ and solve for the new values of η using (3.2-5) to (3.2-7). The new taper has a minimum value of η_{min} and produces the same relative scattering pattern.

Another important realization is that these synthesis techniques work for the backscattering pattern as well as the bistatic scattering pattern, even though $\eta(x)$ is derived for only the normal incidence angle. At normal incidence ($\phi_o = 90°$), the phase of the current across a resistive strip is nearly constant. The small values for σ_{curph} in Table 2.2 confirms this fact, since PO has 0 current phase across the strip for any polarization and strip resistivity when $\phi_o = 0$. Thus, the current phase may be assumed to be zero with reasonable accuracy. However, as ϕ_o varies from $90°$, a nearly linear phase shift is produced in the current across

the strip. If the strip had infinite width, the phase shift would steer the main beam of the scattering pattern to $\phi = -\phi_o$. This is Snell's law. A linear phase shift across the aperture is also used to steer the main beam of an antenna. The larger ϕ_o and the smaller the strip, the less Snell's Law applies, because the edges make a large contribution relative to the surface. In fact, H-polarization has a traveling current that becomes more dominant near edge-on incidence [Peters, 1958]. Thus, a "reasonable" variation in ϕ_o should only "steer" the main beam of the scattering pattern without having much effect on the shape of the pattern. As a result, we should expect the backscattering pattern to also exhibit desirable properties at angles other than those near grazing incidence.

3.3 Taylor Low Sidelobe Synthesis Technique

An effective way to control the scattering patterns from a strip is to relate a strip current density that produces the desired scattering pattern to a resistive taper via (3.2-5) to (3.2-7). Low sidelobes over a specified angular sector is a very desirable far field pattern characteristic. Many aperture tapers are available to generate low sidelobes in the far field for phased array antennas, as well as continuous apertures. Some of the more popular tapers include Chebychev, Taylor, Binomial, and Bayliss. These tapers have the common characteristic that the height of the sidelobes decreases or remains constant as the angle from the main beam increases. Of these, the Taylor current taper [Taylor, 1955] has the most desirable characteristics.

This analysis uses the Taylor amplitude taper to relate the far field pattern to the current on the strip for two reasons.[8] First, it produces very desirable far field pattern characteristics. The taper limits the first $\bar{n}$-1 sidelobes on either side of the main beam to a height of q dB below the peak of the main beam, while the remaining sidelobes fall-off exponentially. Second, the taper is smooth with little to no increases in current at the edges. This advantage is extremely important when using PO, since PO does not take edge effects into account. Tapers with large increases in current at the edges are difficult to physically realize (e.g Chebychev).

---

[8] New techniques have been reported that give arbitrary sidelobe topography [Elliot, 1981a and 1985b]. In other words, each sidelobe of the antenna pattern may be specified at a certain height. Instead of using one of these methods, more standard low sidelobe taper with the option of placing nulls in the pattern (section 3.3.2) is used here.

The current amplitude weights for the Taylor taper are given by[Stutzman and Thiele, 1981]

$$J_s(x) = \frac{1}{2a}\left[1 + 2\sum_{n=1}^{\overline{n}-1} f(n)cos(\frac{\pi n x}{a})\right] \qquad (3.3\text{-}1)$$

where

$$f(n) = \begin{cases} \frac{[(\overline{n}-1)!]^2}{(\overline{n}-1+n)(\overline{n}-1-n)} \prod_{m=1}^{\overline{n}-1}(1 - \frac{n^2}{w_m^2}), & |n| < \overline{n} \\ 0, & |n| \geq \overline{n} \end{cases}$$

$$w_m = \begin{cases} \overline{n}\sqrt{\frac{A^2+(m-0.5)^2}{A^2+(\overline{n}-0.5)^2}}, & |n| < \overline{n} \\ n, & |n| \geq \overline{n} \end{cases}$$

$\overline{n} - 1$ = number of sidelobes q dB below the main beam

x = distance from center of strip in wavelengths

$2a$ = length of strip in wavelengths

$$A = \frac{1}{\pi}cosh^{-1}R$$

$$R = 10^{q/20}$$

Figure 3.15 shows the resistive taper derived from (3.2-5) and its corresponding induced current and scattering patterns for a 30dB, $\overline{n}=6$ Taylor current taper on a 4λ strip with an E-polarized incident plane wave. Figure 3.15c shows the desired bistatic scattering pattern perfectly replicated from the complex strip resistivity. As predicted, the backscattering pattern bears a rather good resemblence of the desired pattern. Although the backscattering pattern does not go to zero at edge-on incidence, it is about 18dB lower than the backscattering pattern of the perfectly conducting strip.

A resistive taper may also be synthesized form the same Taylor current taper using PO. This time, the taper is real-valued. Figure 3.16b is the PO resistive taper. The strip current density calculated using PO and the integral equation approaches are shown in Figure 3.16a. These currents agree very closely. The corresponding bistatic scattering patterns are shown in Figure 3.16c. Notice that the PO and integral equation patterns nearly overlay except

at 0° to $15°$ observation angles and right at the null locations. The integral equation backscattering pattern in 3.16d actually resembles the desried Taylor pattern better than the backscattering pattern in 3.15d. Again, the PO and integral equation approaches agree very well except at $0°$ through $15°$ observation angles and at the null at $30°$.

Two other ways of getting real-valued resistive tapers are taking the real part of or the magnitude of the tapers derived from the integral equation formulas. Examples of these procedures applied to the taper in Figure 3.15 appear in Figures 3.17 and 3.18, respectively. The scattering patterns closely resemble the far field patterns of the desired Taylor taper. Of the four methods of getting a resistive taper, the PO approach produced a backscattering pattern most closely resembling the desired Taylor taper. Consequently, all the low sidelobe Taylor tapers in the remainder of this thesis are derived from PO.

The PO synthesis technique works equally well for H-polarization (Figure 3.19). The resistive tapers in Figure 3.16 and 3.19 are identical and the current taper and scattering patterns are very similar even though the polarizations are orthogonal.

Much lower sidelobes are also possible. Figures 3.21 and 3.22 show the resistive PO tapers of a 40dB $\bar{n}{=}12$ Taylor current taper for E- and H-polarizations, respectively. The strip current density and scattering patterns are calculated using the integral equation and PO approaches and are shown together for comparison. Notice the very close agreement between the two approaches.

3.4 Modifying the Current on a Strip for Nulls

Occasionally, nulls at certain angles (particularly at edge-on incidence) in the far field pattern are desirable in addition to or instead of low sidelobes. This section begins by describing a technique reported by Shore and Steyskal for placing nulls in the far field pattern of an array. It is used to place multiple nulls in a bistatic scattering pattern or a single null in a backscattering pattern. Placing multiple nulls in a backscattering pattern is desirable in some cases, but is considerably more difficult to do. The problem is discussed at the end of this section, but not solved.

3.4.1 Nulling by Minimization of Current Perturbations

Although Shore and Steyskal [1982] developed this technique for phased array antennas,

a. Magnitude of induced surface
current density on strip, $\phi_o=90°$

b. Normalized resistivity on strip

c. Bistatic scattering pattern, $\varphi_o=90°$

d. Backscattering pattern
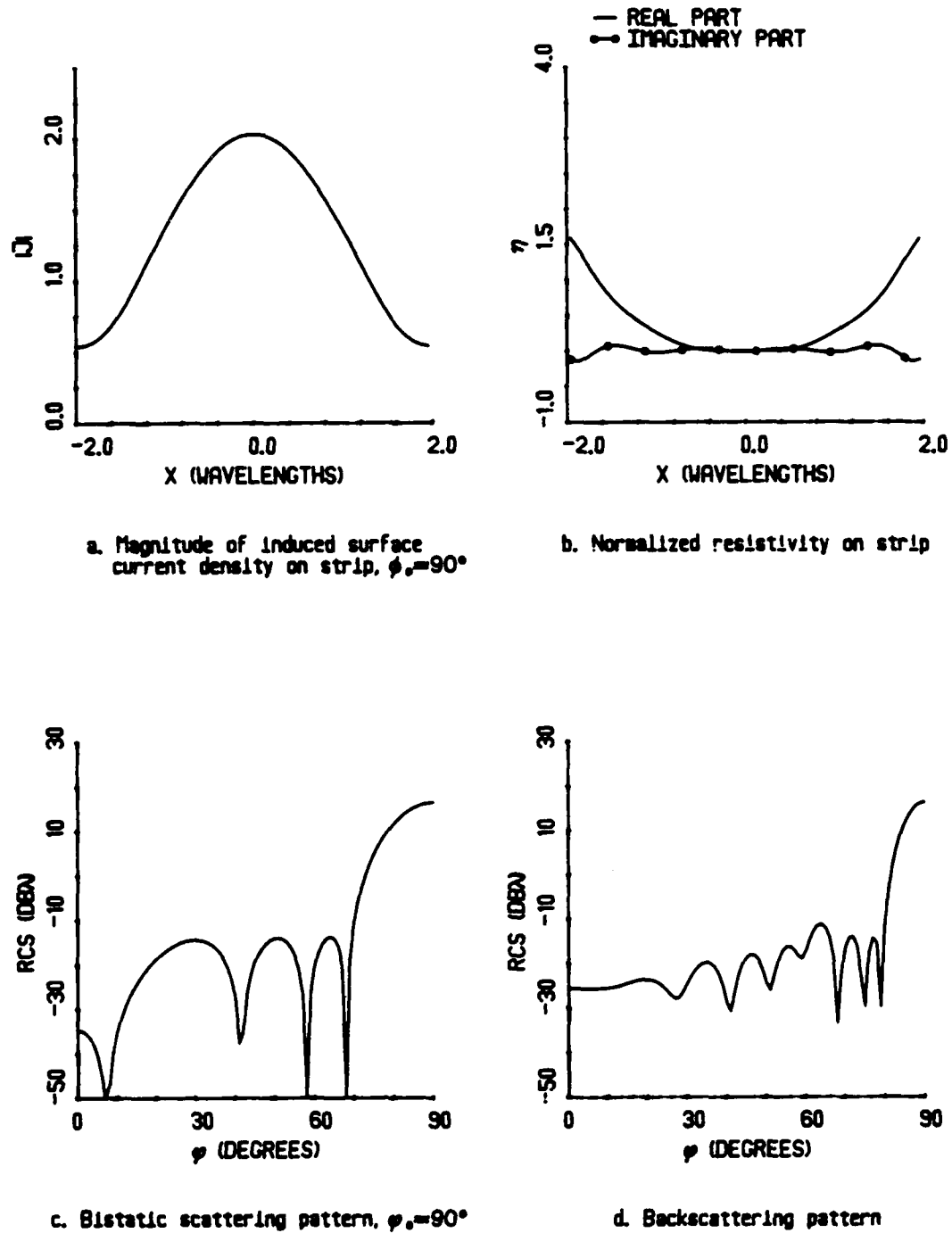
Figure 3.15 — E-polarized computed scattering results for a 4λ resistive strip when η is synthesized from a 30 dB $\bar{n}=6$ Taylor current taper using the integral equation approach.

a. Magnitude of induced surface current density on strip, $\phi_o = 90°$

b. Normalized resistivity on strip

c. Bistatic scattering pattern, $\varphi_o = 90°$

d. Backscattering pattern

Figure 3.16 — E-polarized computed scattering results for a 4λ resistive strip when η is synthesized from a 30 dB $\bar{n}=6$ Taylor current taper using the PO approach.

a. Magnitude of induced surface
current density on strip, $\phi_o=90°$

b. Normalized resistivity on strip

c. Bistatic scattering pattern, $\varphi_o=90°$

d. Backscattering pattern
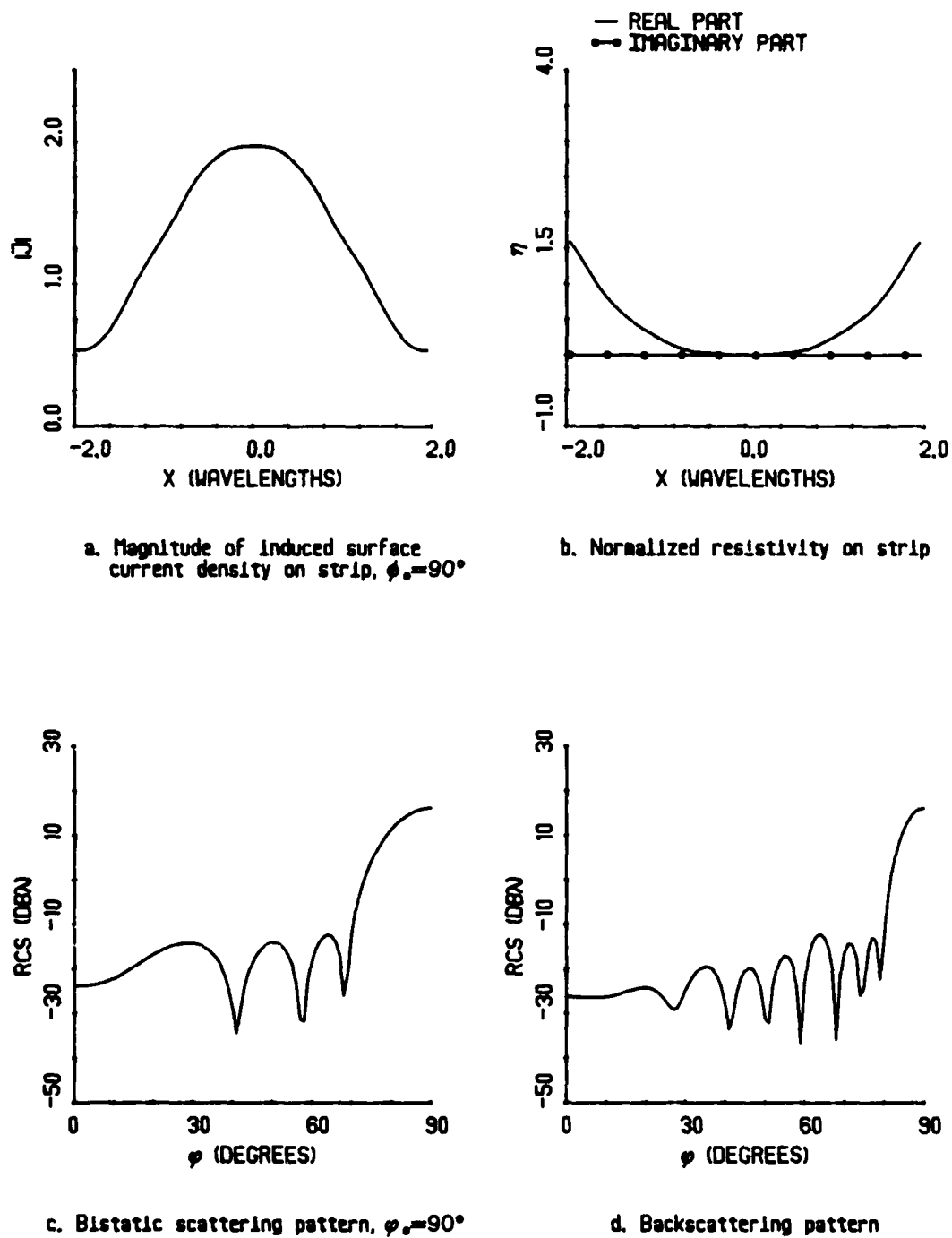
Figure 3.17 — E-polarized computed scattering results for a 4λ resistive strip with η synthesized from a 30 dB $\bar{n}=6$ Taylor current taper using the $|\eta|$ from the integral equation approach

a. Magnitude of induced surface current density on strip, $\phi_o=90°$

b. Normalized resistivity on strip

c. Bistatic scattering pattern, $\varphi_o=90°$

d. Backscattering pattern
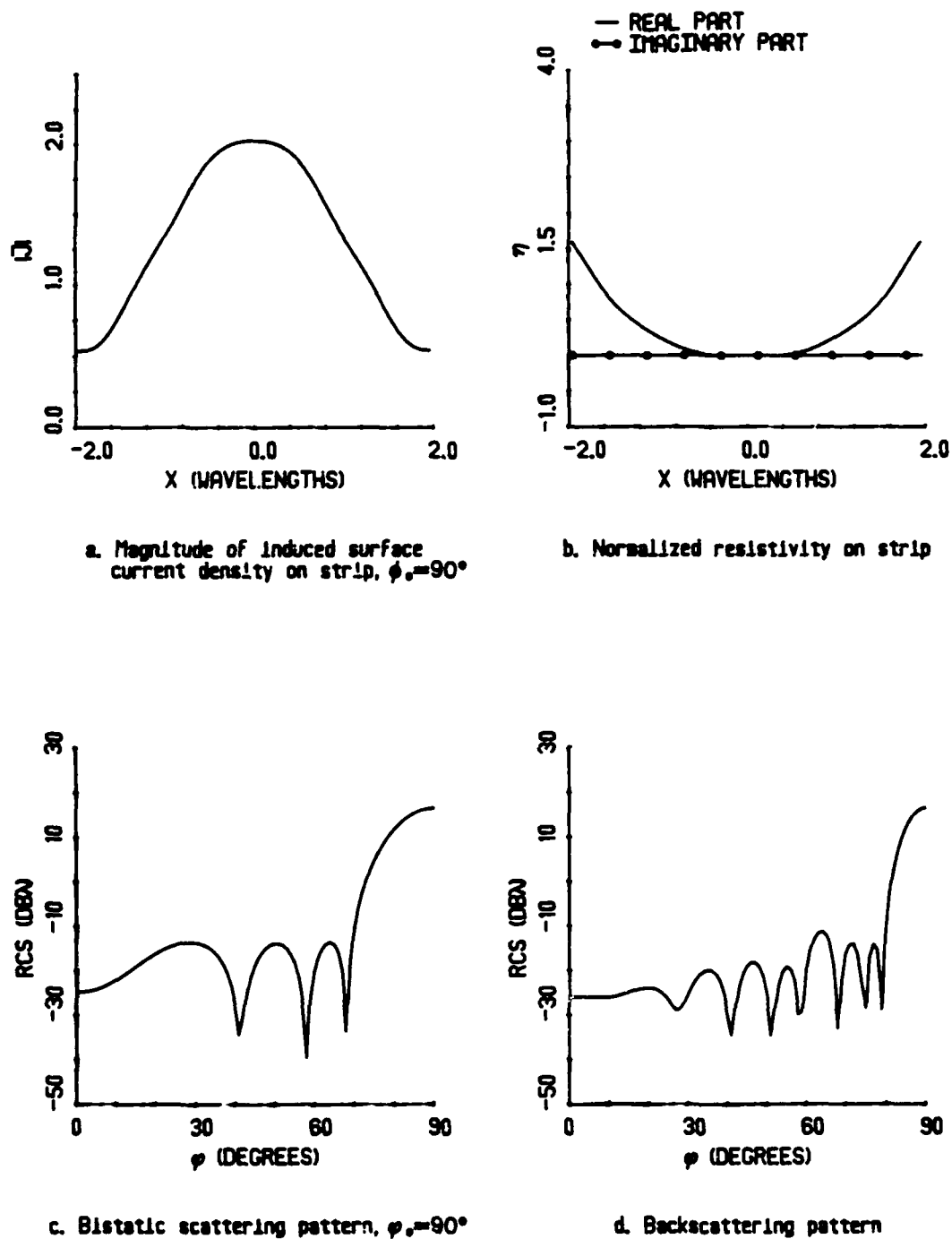
Figure 3.18 — E-polarized computed scattering results for a 4λ resistive strip with η synthesized from a 30 dB $\bar{n}=6$ Taylor current taper using $Real\{\eta\}$ from the integral equation approach

a. Magnitude of induced surface current density on strip, ϕ_o=90°

b. Normalized resistivity on strip

c. Bistatic scattering pattern, φ_o=90°

d. Backscattering pattern
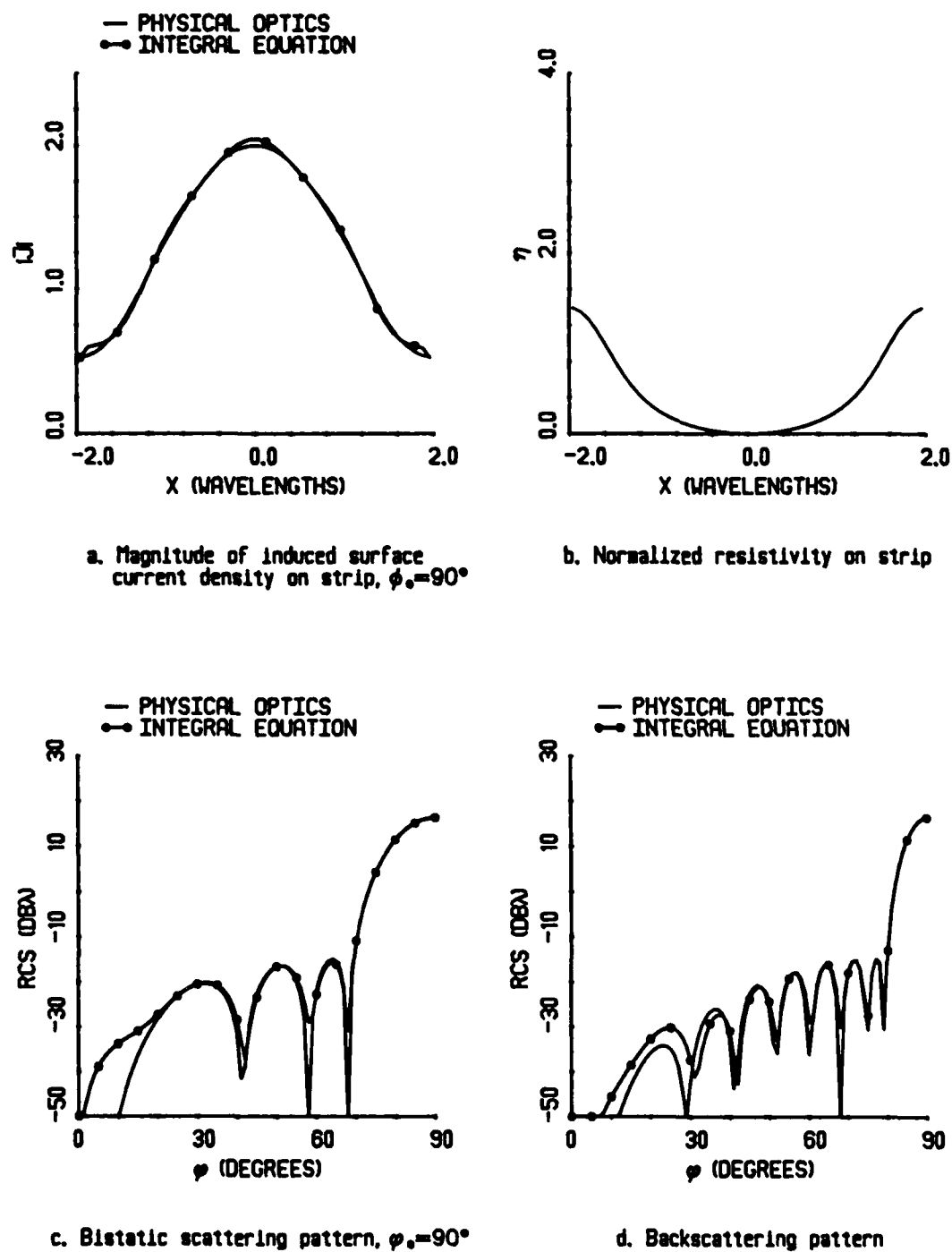
Figure 3.19 — H-polarized computed scattering results for a 4λ resistive strip when η is synthesized from a 30 dB $\bar{n}$=6 Taylor current taper using the PO approach

— PHYSICAL OPTICS
•—• INTEGRAL EQUATION

a. Magnitude of induced surface
   current density on strip, $\phi_0=90°$

b. Normalized resistivity on strip

— PHYSICAL OPTICS
•—• INTEGRAL EQUATION

— PHYSICAL OPTICS
•—• INTEGRAL EQUATION
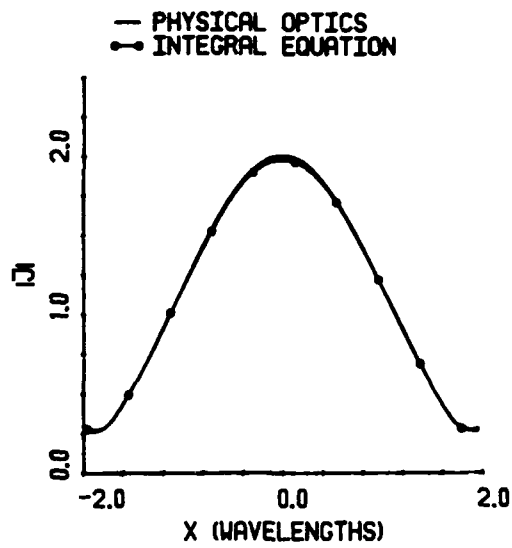
c. Bistatic scattering pattern, $\varphi_0=90°$

d. Backscattering pattern

Figure 3.20 — E-polarized computed scattering results for a 4λ resistive strip when η is
synthesized from a 40 dB $\bar{n}=12$ Taylor current taper using the PO approach

— PHYSICAL OPTICS
•—• INTEGRAL EQUATION

a. Magnitude of induced surface
current density on strip, $\phi_o=90°$

b. Normalized resistivity on strip

— PHYSICAL OPTICS
•—• INTEGRAL EQUATION

— PHYSICAL OPTICS
•—• INTEGRAL EQUATION

c. Bistatic scattering pattern, $\varphi_o=90°$

d. Backscattering pattern

Figure 3.21 — H-polarized computed scattering results for a 4λ resistive strip when η is synthesized from a 40 dB $\bar{n}=12$ Taylor current taper using the PO approach

it also works with continuous current sources, in particular current induced in a resistive strip.

The current distribution on the strip that generates nulls at specified angles in the bistatic scattering pattern is represented by the quiescent current, $J_o(x)$, plus a perturbation, $J_o(x)\delta(x)$.

$$J_s(x) = J_{so}(x)(1 + \delta(x)) \qquad (3.4\text{-}1)$$

In the far field, this new current produces nulls at M locations

$$S(\phi_m) = \int_{-a}^{a} J_s(x)e^{jkx\cos\phi_m}dx = 0 \quad \text{for } m = 1, 2, ..., M \qquad (3.4\text{-}2)$$

where $S(\phi)$ is the relative far field pattern. The above integral may then be solved using mid point integration

$$S(\phi_m) = \Delta \sum_{n=1}^{N} J_n e^{jkx_n\cos\phi_m} = \Delta \sum_{n=1}^{N} (1 + \delta_n)J_{on}e^{jkx_n\cos\phi_m} = 0 \qquad (3.4\text{-}3)$$

where

$J_n =$ current that produces nulls in the far field

$J_{on} =$ quiescent current

$\delta_n =$ perturbation to the quiescent current

$\Delta = \dfrac{2a}{N} =$ length of current segment

$S =$ far field pattern

Rearranging (3.4-3) into a form amenable to matrix solution yields

$$\sum_{n=1}^{N} \Delta \delta_n J_{on} e^{jkx_n\cos\phi_m} = -\sum_{n=1}^{N} \Delta J_{or} e^{jkx_n\cos\phi_m} = -S_o(\phi_m), \ m = 1, 2, ..., M \qquad (3.4\text{-}4)$$

where S_o is the quiescent relative far field pattern.

Now that (3.4-4) is in the form of M equations with N unknowns, where M<N, a least squares solution is possible. Usually, the minimum norm solution to the matrix equation is given by

$$(A^\dagger A)x = A^\dagger b \qquad (3.4\text{-}5)$$

where $\dagger$ is the comp.. conjugate transpose of matrix A. The unknown vector, x, is found using PLU decomposition and back-substitution. For this application, however, $M << N$ and a simpler solution is given by

$$x = A^\dagger (AA^\dagger)^{-1} b \qquad (3.4\text{-}6)$$

Rather than using PLU decompositition and back-substitution on the N $\times$ N matrix $(A^\dagger A)$, the actual inverse of $(AA^\dagger)^{-1}$ is computed since it is only an M $\times$ M matrix compared.

If the current perturbations are minimized in a least mean square sense

$$\sum_{n=1}^{N} |\delta_n|^2 = \text{minimum} \qquad (3.4\text{-}7)$$

then the components of (3.4-6) take the form

$$x = [\delta_1, \delta_2, ..., \delta_N]^T \qquad (3.4\text{-}8)$$

$$b = [S(\phi_1), S(\phi_2), ..., S(\phi_m)]^T \qquad (3.4\text{-}9)$$

$$A = \begin{pmatrix} J_1 e^{jkx_1 \cos\phi_1} & J_2 e^{jkx_2 \cos\phi_1} & ... & J_N e^{jkx_N \cos\phi_1} \\ J_1 e^{jkx_1 \cos\phi_2} & J_2 e^{jkx_2 \cos\phi_2} & ... & J_N e^{jkx_N \cos\phi_2} \\ \vdots & \vdots & \ddots & \vdots \\ J_1 e^{jkx_1 \cos\phi_M} & J_2 e^{jkx_2 \cos\phi_M} & ... & J_N e^{jkx_N \cos\phi_M} \end{pmatrix} \qquad (3.4\text{-}10)$$

where ^{T} is the transpose of the vector.

The minimization in (3.4-7) is, of course, not unique. One other interesting approach is to have

$$\sum_{n=1}^{N} |J_o \delta_n|^2 = \text{minimum} \qquad (3.4\text{-}7)$$

This approach minimizes the perturbations to the far field pattern rather than the perturbations to the current.

Figures 3.22 to 3.24 show examples of the nulling technique using the integral equation approach to derive the resistive taper. Figure 3.22 is an example of placing nulls at 20° and

$50°$ in the bistatic scattering patterns of a 4λ perfectly conducting strip. The reisistivity is complex with small variations in the real and imaginary parts. In order to avoid negative values of strip resistivity, the taper is normalized using the procedure outlined in section 3.2.3. The current still exhibits singularities at the edges, even with the resistive taper. No nulls appear in the backscattering pattern.

Figure 3.23 shows the scattering results when nulls are placed in a low sidelobe taper. As before, the nulls are at $20°$ and $50°$ in the bistatic scattering pattern. The quiescent resistive taper is derived from a Taylor current taper using PO.

Figure 3.24 is an example of placing a single null in the backscattering pattern at $0°$. The strip current density has large unrealistic variations across the strip. This example does show, though, that it is at least theoretically possible to place a single null in the backscattering patterns of strips. The resistive taper derived for backscattering nulls does not place nulls in the bistatic pattern at $90°$. They do, however, place a null in the specular direction of the bistatic scattering pattern calculated at the angle of the null.

3.4.2 Placing Multiple Nulls in the Backscattering Far Field Pattern

Placing multiple nulls in the backscattering far field pattern of a strip is conceivably possible, but the procedure is considerably more complicated and will only be outlined here. The problem with placing multiple nulls in the backscattering pattern of a strip is that a different induced strip current density contributes to the scattering pattern at each angle. Placing multiple nulls in a bistatic scattering pattern is simpler, because only one strip current density distribution contributes to the scattering pattern. The Shore-Steyskal nulling method places multiple nulls in the far field pattern of one strip current density distribution. In turn, a resistive taper is synthesized form this strip current density distribution. As the angle of incidence changes in the backscattering pattern so does the induced strip current density. The Shore-Steyskal method can calculate a strip current density that places a single null in the specular direction of a bistatic scattering pattern which also places a null in the backscattering pattern in the same direction. The same method can also produce a null in the backscattering pattern in a different direction. However, two different resistive tapers are needed to produce the two different strip current densities. Since the resistive taper cannot vary, the Shore-Steyskal method is not adequate for placing multiple nulls in

a. Magnitude of induced surface current density on strip, $\phi_o=90°$

b. Normalized resistivity on strip

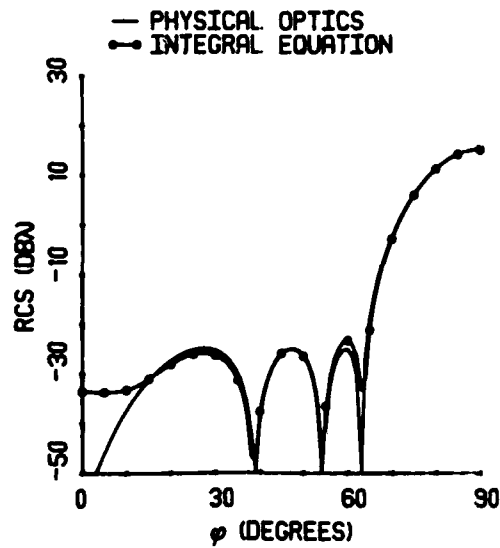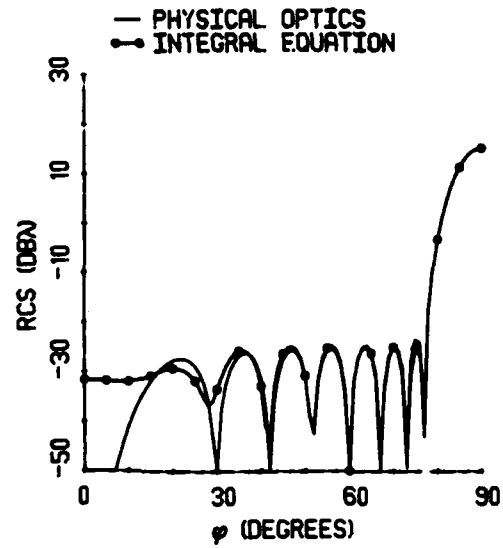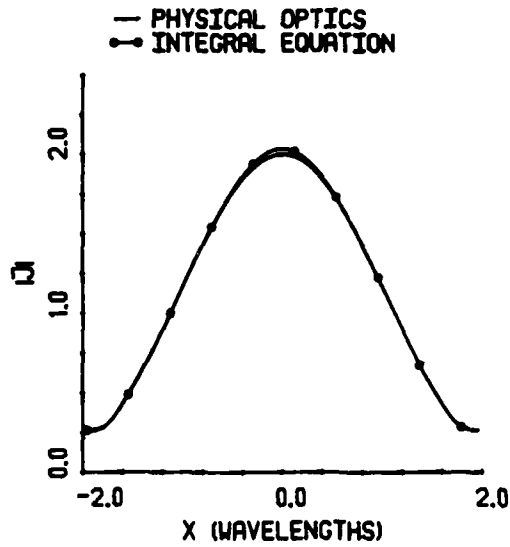c. Bistatic scattering pattern, $\varphi_o=90°$

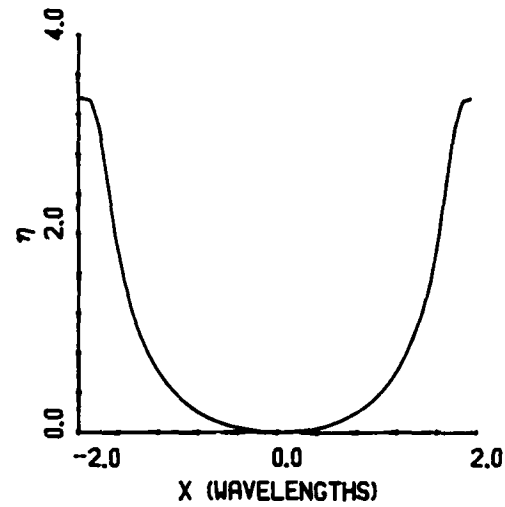d. Backscattering pattern

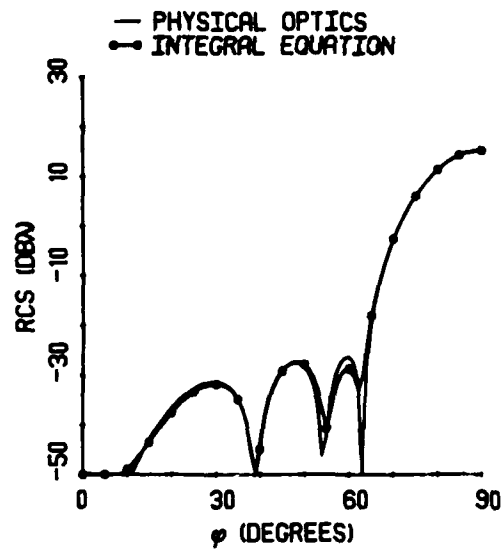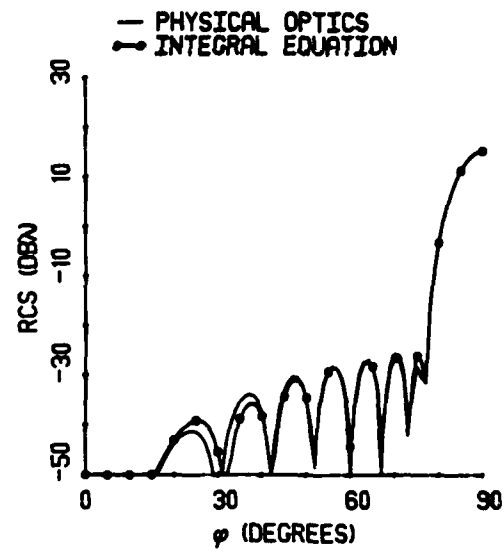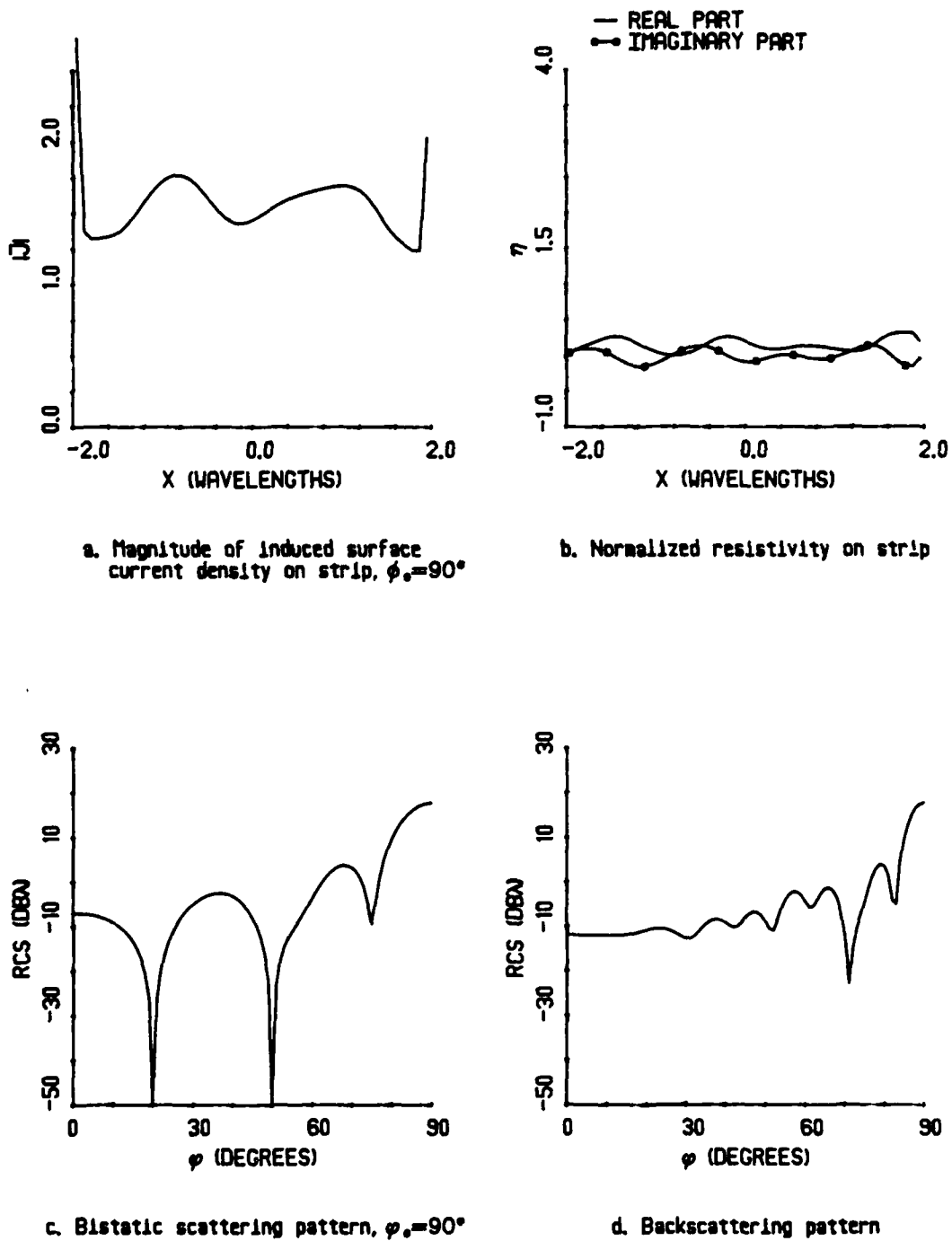Figure 3.22 — E-polarized integral equation scattering results for a 4λ perfectly conducting strip with η synthesized for nulls in the bistatic scattering pattern at $20°$ and $50°$.

a. Magnitude of induced surface
current density on strip, ϕ_o=90°

b. Normalized resistivity on strip

c. Bistatic scattering pattern, φ_o=90°

d. Backscattering pattern
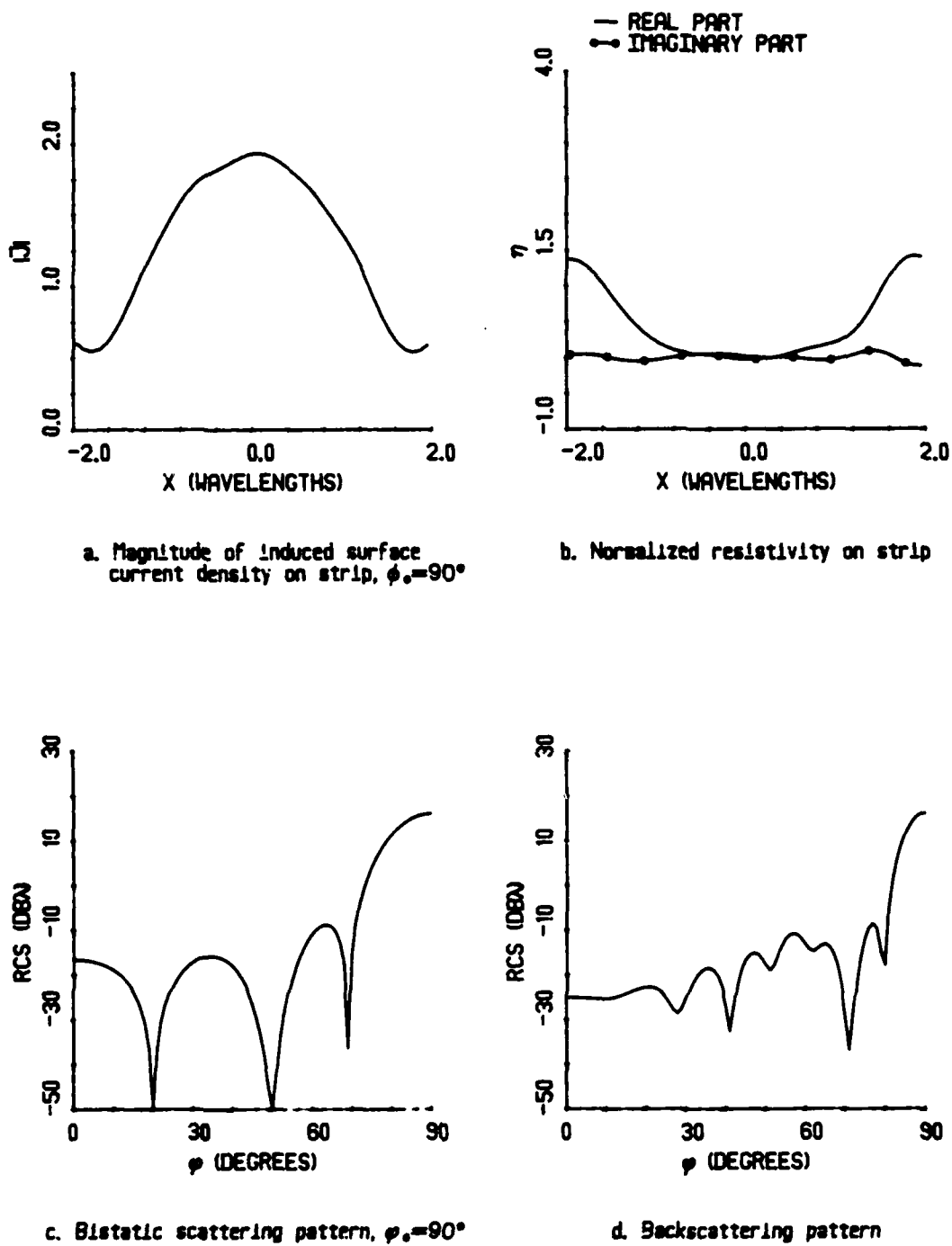
Figure 3.23 — E-polarized integral equation scattering results for a 4λ strip with η
synthesized from a Taylor current taper with nulls in the bistatic scattering pattern at
20° and 50°.

a. Magnitude of induced surface
current density on strip, ϕ_o=90°

b. Normalized resistivity on strip

c. Bistatic scattering pattern, φ_o=90°

d. Backscattering pattern
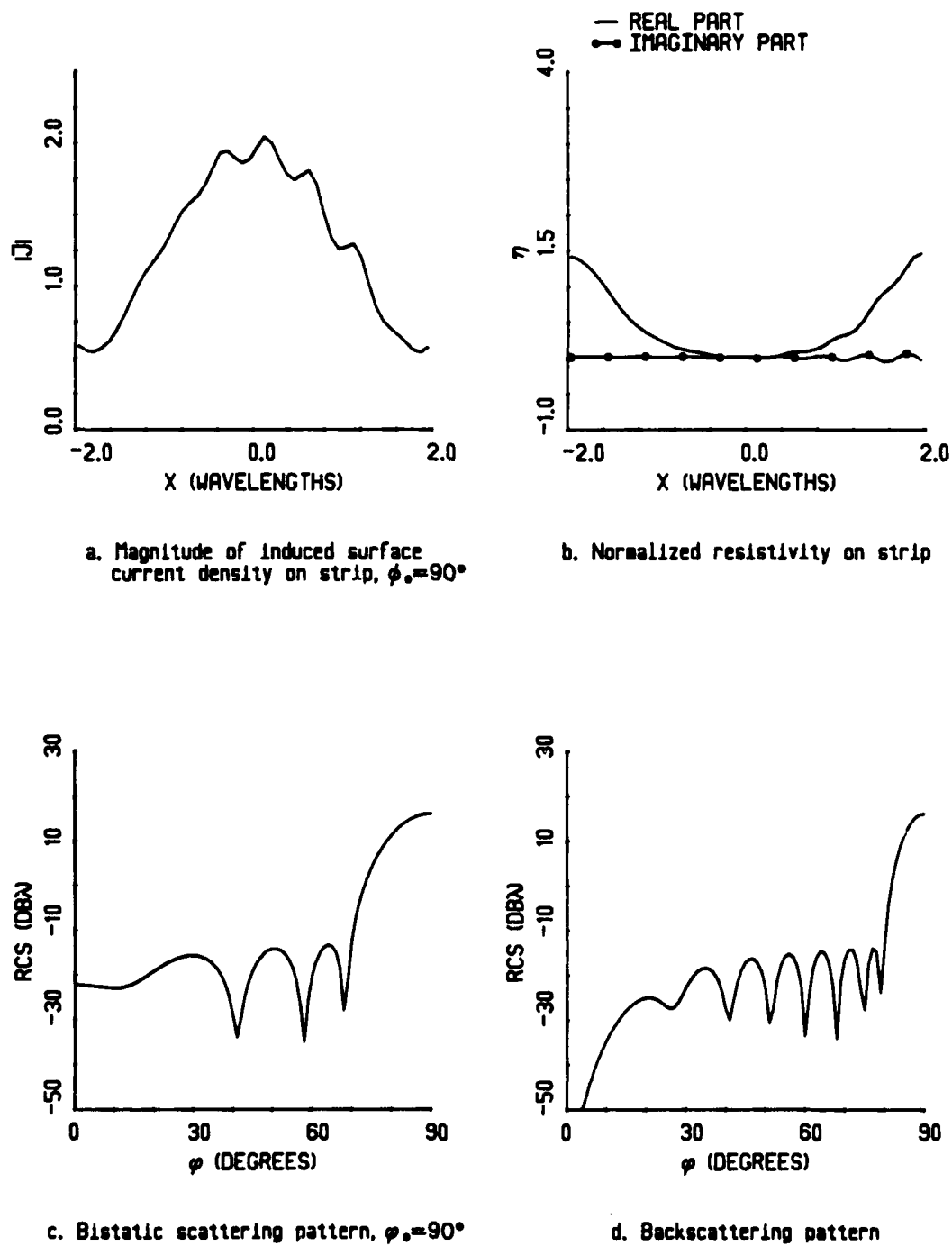
Figure 3.24 — E-polarized integral equation scattering results for a 4λ strip with η
synthesized from a Taylor current taper with a null in the backscattering pattern at $0°$.

the backscattering pattern.

More than one resistive taper can place a null in the specular direction of a bistatic scattering pattern. Placing multiple nulls in the backscattering pattern requires finding one resistive taper that results in nulls in 2 or more specular directions. The strip resistivity perturbations may be very erratic. Iterative techniques, steepest descent, and non-linear programming are possible methods to use in finding a resistive taper that causes multiple nulls in the backscattering pattern.

CHAPTER IV

STATIC RESISTIVITY MEASUREMENTS USING A FOUR-POINT PROBE

An important step in the manufacturing process of a resistive sheet with a low sidelobe resistive taper is accurately measuring the sheet resistivity. Errors in the measurement process manifest themselves as errors in the scattering patterns of the sheet. If the errors are large enough, then the sidelobes will not meet the tolerances of the desired taper.

Three viable nondestructive techniques for measuring sheet resistivity are four-point probe, network analyzer, and two-point probe measurements. The four-point and two-point probe measurements are static measurements, while the network analyzer measurement is an rf measurement. Other, perhaps more accurate, techniques are available for measuring the sheet resistivity, but they involve destroying the test object. For instance, cutting a small square from a resistive sheet, painting highly conductive strips on both sides of the square, then measuring the sheet resistivity with an ohm meter, gives an accurate answer. This technique is unacceptable because it destroys the sheet.

Four-point probe measurements of sheet resistivity have been of major importance in semiconductor electronics. The four point probe has two outer probes that insert a known current on the surface of the sheet and the two inner probes measure a voltage drop due to the current. A simple formula then relates the resistance on the sheet to the current and voltage drop. This method was used to determine the resistivity of the experimental resistive sheet; hence, it is of most interest here.

Network analyzer measurements of sheet resistivity have been limited. This method is attractive because the measurement is performed at the frequency of interest. The network

analyzer determines the reflection coefficient of the material under test which then relates to the complex dielectric constant of the medium. This method has been successfully applied to liquids such as water [Stuchly, 1982] and to vegetation such as leaves [ElRayes, 1987]. Wang also used this method to measure the resistivity of a tapered resistive groundplane [Wang, 1985].

Two-point probe measurements do not provide the accuracy of the four-point probe measurements. Wang [1985] measured resistive sheets with the two point probe and found the measurements varied significantly from one measurement to the next. She attributes this problem to the fact that the measured resistivity depends upon the contact between the probe and sheet. To help alleviate the problem, she averaged twenty sheet resistivity measurements to get an estimate of the actual sheet resistivity.

The first part of this chapter describes an analytical technique for finding the sheet resistivity of a uniform sheet using a four-point probe. Although it is derived for a uniform sheet, it is used to measure the sheet resistivity of tapered sheets. The second part of the chapter derives a partial differential equation for the voltage on the resistive sheet and solves for the voltage using Successive Over Relaxation (SOR). Results of the analytical and numerical methods are compared. Then, the accuracy of extending the analytical results to tapered sheets and measurements close to the edges is examined with the numerical method.

4.1 Analytically Calculating the Sheet Resistivity of a Uniform Resistive Sheet from Four-point Probe Measurements

Methods of calculating the static resistivity of materials from four-point probe measurements have appeared in the literature for many years. Valdes [1952] reports theoretical and experimental results on the effect of electrode spacing on measuring the resistivity of germanium semiconductor materials. He also gives various theoretical corrections to resistivity measurements on a finite piece of germanium [Valdes, 1954]. Uhlir [1954] and Smits [1957] provide analytical solutions for finding the resistivity of a surface using image theory. Although analytical solutions are not developed for tapered resistivities, they can provide a means of checking numerical algorithms developed for tapered resistive sheets.

Figure 4.1 is a diagram of a four point probe measurement system with a probe spacing of s. The probes lie along the y axis and symmetrically about the x axis. A direct current (I) passes through the outer two probes and a voltage differential (ΔV) appears between the inner two probes. One may find the resistivity by knowing the probe spacing, size of the resistive sheet ($2a \times d$), and the voltage and current between the inner and outer probe respectively.

Assuming the resistive sheet lies in the x-y plane and the resistivity does not vary in the ϕ or z directions, then Gauss' law states that

$$\int\int \overline{D} \cdot \overline{dS} = q \tag{4.1-1}$$

and

$$E(\rho) = \frac{q}{2\pi\rho} \tag{4.1-2}$$

The voltage drop between terminals 1 and 2 due to the positive current source is given by

$$V_A = \int_s^{2s} \overline{E} \cdot \overline{dl} = \int_s^{2s} \frac{q}{2\pi y \epsilon} dy = \frac{q}{2\pi\epsilon} \ln 2 \tag{4.1-3}$$

Likewise, the voltage drop between 1 and 2 due to the negative current source is given by

$$V_B = \frac{q}{2\pi\epsilon} \ln 2 \tag{4.1-4}$$

The total voltage drop between 1 and 2 is given by the superposition of the results form (4.1-3) and (4.1-4)

$$\Delta V = V_a + V_B = \frac{q}{\pi\epsilon} \ln 2 \tag{4.1-5}$$

Using (4.1-2), (4.1-5) may be written as

$$\Delta V = \frac{\ln 2}{\pi} \int_0^{2\pi} R\overline{J} \cdot \overline{dl} \, \rho d\phi \tag{4.1-6}$$

Since R does not vary with ϕ, it can be taken outside the integral.
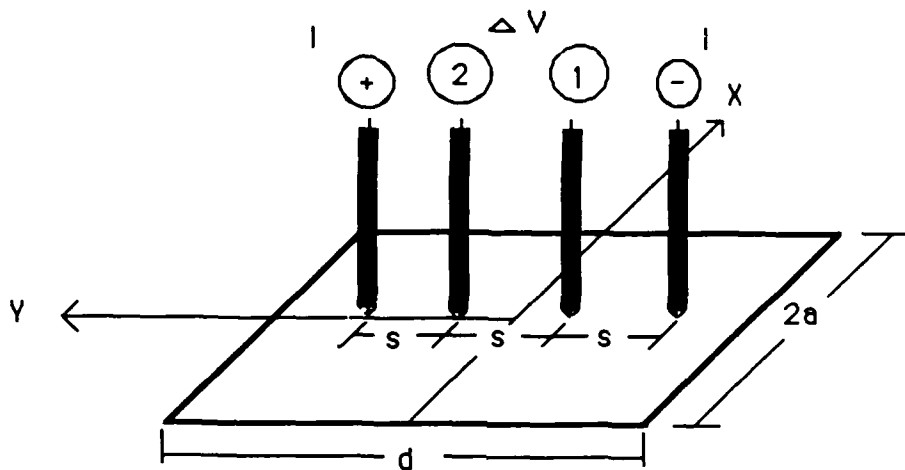
Figure 4.1 — Diagram of a four point probe measuring system. The outer probes insert a current I and the inner probes measure a voltage differential ΔV.

$$\Delta V = \frac{R \ln 2}{\pi} \int_0^{2\pi} J\rho d\phi \qquad (4.1\text{-}7)$$

$$\frac{\Delta V}{R} = \frac{I \ln 2}{\pi} \qquad (4.1\text{-}8)$$

Solving (4.1-8) for R gives

$$R = \frac{\Delta V \pi}{I \ln 2} \qquad (4.1\text{-}9)$$

Since (4.1-9) is not valid for finite resistive sheets, a correction factor is needed to take into account the finite size of the resistive sheet. Equations have been developed to sum the current points and their infinite number of images to find ΔV between the voltage probes which are symmetrically placed about the center of the sheet. Assuming that V, I, a, d, and s are known, the equation for the resistance is [Smits, 1958]

$$R = \frac{\Delta V}{I} C\left(\frac{d}{a}, \frac{a}{s}\right) \qquad (4.1\text{-}10)$$

where Table 4.1 lists the values for $C(\frac{d}{2a}, \frac{2a}{s})$.

4.2 Numerically Calculating the Resistivity of a Tapered Resistive Sheet

The solution in the preceding section assumes several simplifications to the problem. First, the probes must lie along the y axis and symmetric about the x axis. Second, the resistivity must be constant. Neither of the simplifications is possible when measuring the resistivity of a tapered resistive sheet. In this case, one must resort to a numerical solution of the static fields.

Static fields have a solenoidal current:

$$\nabla \cdot J = 0 \qquad (4.2\text{-}1)$$

Substituting $J = -G\nabla V$ into this equation and expanding ∇ into its rectangular representation yields

$$\frac{\partial G(x,y)}{\partial x}\frac{\partial V(x,y)}{\partial x} + G(x,y)\frac{\partial^2 V(x,y)}{\partial x^2} + \frac{\partial G(x,y)}{\partial y}\frac{\partial V(x,y)}{\partial y} + G(x,y)\frac{\partial^2 V(x,y)}{\partial y^2} = 0 \quad (4.2\text{-}2)$$

$\frac{2a}{s}$	$\frac{d}{2a} = 1$	$\frac{d}{2a} = 2$	$\frac{d}{2a} \geq 2$
1.0			0.9994
1.25			1.2248
1.5		1.4788	1.4893
1.75		1.7196	1.7238
2.0		1.9454	1.9475
2.5		2.3532	2.3541
3.0	2.4575	2.7000	2.7005
4.0	3.1137	3.2246	3.2248
5.0	3.5098	3.5749	3.5750
7.5	4.0095	4.0361	4.0362
10.0	4.2209	4.2357	4.2357
15.0	4.3882	4.3947	4.3947
20.0	4.4516	4.4553	4.4553
40.0	4.5120	4.5129	4.5129
∞	4.5324	4.5324	4.5324

Table 4.1 — Correction factors for measuring a finite sheet with a four point probe. The variables are s=probe spacing. 2a=width of sheet, and d=length of sheet.

where $G = \frac{1}{R}$ is the sheet conductivity. Assuming that the resistivity varies only in the x-direction reduces the above equation to

$$R(x)\frac{\partial G(x)}{\partial x}\frac{\partial V(x,y)}{\partial x} + \nabla^2 V(x,y) = 0 \qquad (4.2\text{-}3)$$

For numerical solution, this equation is placed into a finite difference form using fourth order differencing schemes with equal spacing for the first and second derivatives. The indices give the location of the grid point, where n is in the x-direction and m in the y-direction.

$$\frac{R(n)}{12h}\Big[G(n-2) - 8G(n-1) + 8G(n+1) - G(n+2)\Big] \times$$
$$\frac{1}{12h}\Big[V(n-2,m) - 8V(n-1,m) + 8V(n+1,m) - V(n+2,m)\Big] +$$
$$\frac{1}{12h^2}\Big[16\Big(V(n+1,m) + V(n-1,m) + V(n,m+1) + V(n,m-1) - 60V(n,m)\Big)$$
$$- \Big(V(n+2,m) + V(n-2,m) + V(n,m+2) + V(n,m-2)\Big)\Big] = 0 \quad (4.2\text{-}4)$$

where

$h =$ grid spacing in x and y directions

$n =$ point along x, n=1,...,N

$m =$ point along y, m=1,...,M

$N =$ number of points along x that lie on the resistive sheet

$M =$ number of points along y that lie on the resistive sheet

Solving this equation for $V(n,m)$ gives

$$V(n,m) = \frac{R(n)}{720}\Big[G(n-2) - 8G(n-1) + 8G(n+1) - G(n+2)\Big] \times$$
$$\Big[V(n-2,m) - 8V(n-1,m) + 8V(n+1,m) - V(n+2,m)\Big] +$$
$$\frac{1}{60}\Big[16\Big(V(n+1,m) + V(n-1,m) + V(n,m+1) + V(n,m-1)\Big) -$$
$$\Big(V(n+2,m) + V(n-2,m) + V(n,m+2) + V(n,m-2)\Big)\Big] \qquad (4.2\text{-}5)$$

Figure 4.2 shows an example of a finite difference grid. The N+4 grid points in the x direction are spaced h apart, and the M+4 grid points in the y direction are also spaced h
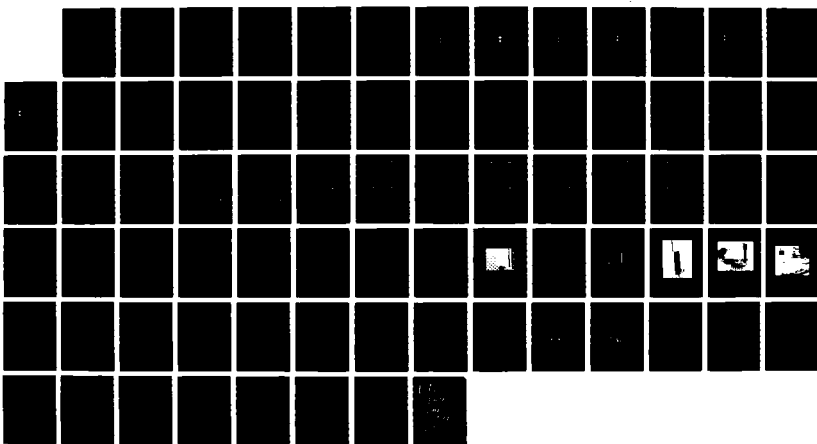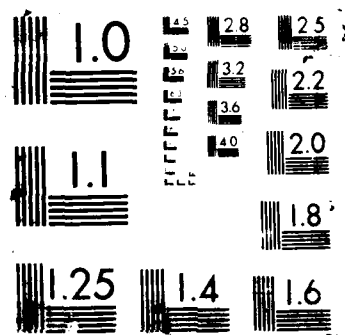
apart. The extra 2 rows and columns of grid points along each edge are necessary to form the Neumann boundary conditions.

When G is constant, the first term (4.2-3) becomes zero, leaving the familiar Laplace's Equation. Actually, if h is chosen small and the difference between G at n-1 and n+1 is small, then this term may also be ignored.

Two voltage source points (+V and -V) are located at the grid points corresponding to the current probes of the four-point probe. An initial guess for V is the solution of Laplace's equation for the two-wire transmission line. This initial guess accelerates convergence of the iterative method.

SOR is an efficient way to iteratively solve this difference equation. It takes the form

$$V_{NEW}(n, m) = (1.0 - \omega)V_{OLD}(n, m) + \omega V_d(n, m) \qquad (4.2\text{-}6)$$

where V_d is calculated from (4.2-5).

The speed of the SOR iterative method depends upon the value chosen for ω. The optimum ω is given by (2.3-2). Another way of finding the optimum ω is to plot ω versus the number of iterations to convergence. The curve has a sharp minimum at the optimum ω. Both there methods are time consuming.

There are some formulas available for estimating ω for the Laplace equation. When the surface is rectangular ω is given by [Varga, 1962]

$$\omega = \frac{4}{2 + \sqrt{(4 - [cos\frac{\pi}{m} + cos\frac{\pi}{n}]^2)}} \qquad (4.2\text{-}7)$$

When the surface is square then [Pearson, 1983]

$$\omega = 2 - 2\,sin(\frac{\pi}{N}) \qquad (4.2\text{-}8)$$

When m=n and $sin\frac{\pi}{N}$ is very small, these two equations are the same.

The boundary conditions for this problem are that the normal component of the derivative of V at the edges is zero. In order to numerically represent a boundary condition, two extra rows of grid points on the top, bottom, and two sides of the M × N grid are necessary. The derivative is estimated by a fourth order approximation which leads to the equation
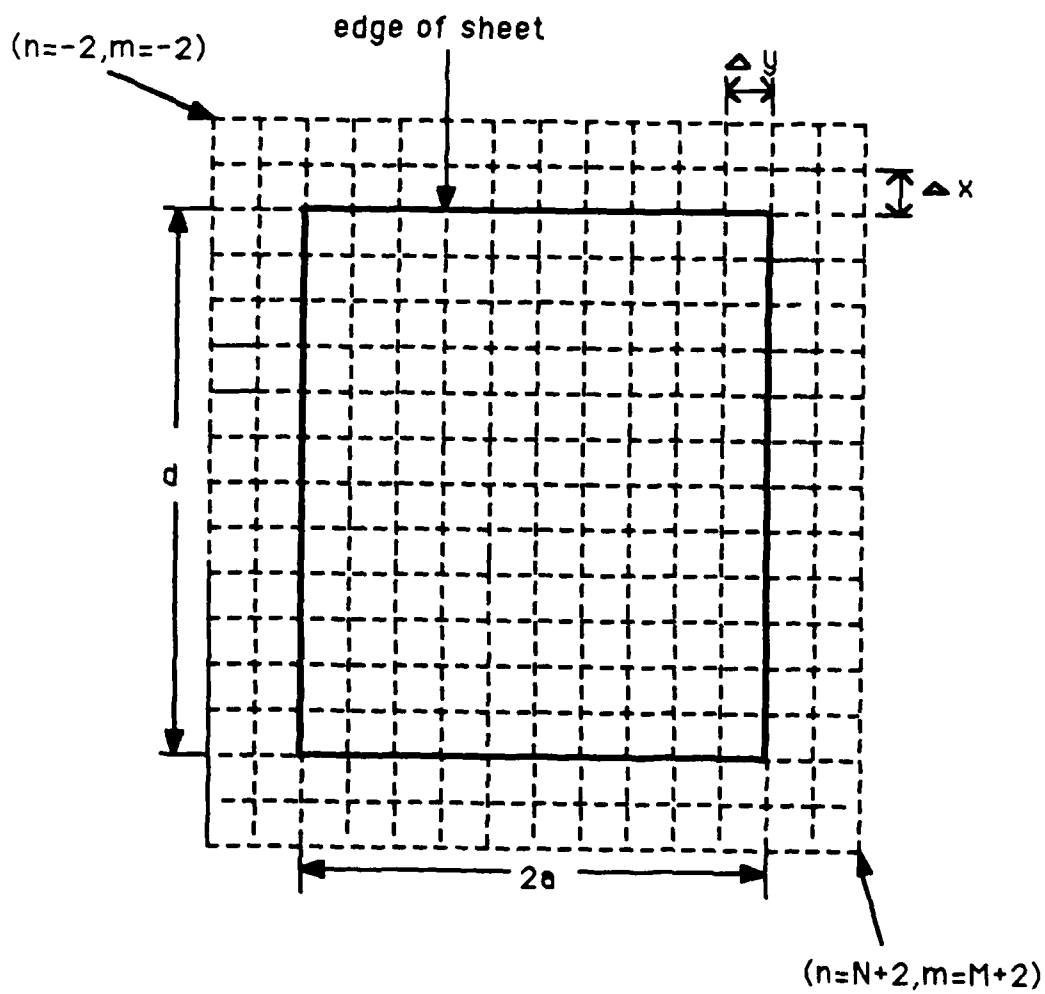
Figure 4.2 — Finite difference grid overlayed on a $2a \times d$ resistive sheet. The intersections of the dashed lines are the grid points. The x grid points range from $(n,m)=(0,0)$ to $(N+1,M+1)$.

$$\text{at } n = 1: \quad \frac{\partial V}{\partial x} = 0 \rightarrow V(-1, m) = V(3, m) \text{ and}$$

$$V(0, m) = V(2, m) \tag{4.2-9}$$

Similarly, the other three boundary conditions are

$$\text{at } n = N: \quad \frac{\partial V}{\partial x} = 0 \rightarrow \qquad V(N - 2, m) = V(N + 2, m) \text{ and}$$

$$V(N - 1, m) = V(N + 2, m) \tag{4.2-10}$$

$$\text{at } m = 1: \quad \frac{\partial V}{\partial y} = 0 \rightarrow \qquad V(n, -1) = V(n, 3) \text{ and}$$

$$V(n, 0) = V(n, 2) \tag{4.2-11}$$

$$\text{at } m = M: \quad \frac{\partial V}{\partial y} = 0 \rightarrow \qquad V(n, M - 2) = V(n, M + 2) \text{ and}$$

$$V(n, M - 1) = V(n, M + 1) \tag{4.2-12}$$

The rows corresponding to n=-1, 0, N+1, and N+2 and the columns corresponding m=-1, 0, N+1, and N+2 do not lie on the resistive sheet. After each iteration the boundary conditions (4.2-9) to (4.2-12) update the extra edge points before starting the next iteration.

The sheet current density can be calculated from the voltage by

$$\overline{J}(n, m) \approx - G(n, m) \frac{1}{12h} \Big\{ \Big[V(n - 2, m) - 8V(n - 1, m) + 8V(n + 1, m) - V(n + 2, m) \Big] \widehat{x} +$$

$$\Big[V(n, m - 2) - 8V(n, m - 1) + 8V(, m + 1) - V(n, m + 2) \Big] \widehat{y} \Big\} \tag{4.2-13}$$

The current, I, at the voltage source points may be found by integrating J around one of the voltage source points.

$$I = \int \overline{J} \cdot \overline{dl} \approx$$

$$h \Big\{ J_y(n, m - 2) - J_y(n, m + 2) + J_x(n - 2, m) - J_x(n + 2, m) +$$

$$J_y(n - 1, m - 2) - J_y(n - 1, m + 2) + J_x(n - 2, m - 1) - J_x(n + 2, m - 1) +$$

$$J_y(n + 1, m - 2) - J_y(n + 1, m + 2) + J_x(n - 2, m + 1) - J_x(n + 2, m + 1) +$$

$$\frac{1}{2} \Big[J_x(n - 2, m - 2) + J_x(n - 2, m + 2) - J_x(n + 2, m - 2) - J_x(n + 2, m + 2) +$$

$$J_y(n - 2, m - 2) + J_y(n - 2, m + 2) - J_y(n + 2, m - 2) - J_y(n + 2, m + 2) \Big] \Big\} \tag{4.2-14}$$

Table 4.2 compares the actual R of a $4\lambda \times 4\lambda$ with the R calculated from (4.1-10) using ΔV and I from the numerical solution and C from Table 4.1. The first 3 rows in the table show the effect of moving the probes (spaced s=.2λ apart) from the center of a uniform resistive sheet toward the edge. Close to the edge, the error in the calculated resistivity is quite high (20.20%). This large error occurs because the correction factor, C, in (4.1-10) was derived for measurements made at the center of the sheet.

The next two rows show the importance of close robe spacing. Measurements near the center do not require close probe spacing, while measurements near the edges do.

Rows 6 and 7 show that edge effects have a greater impact when the edge is parallel to the line of probes than when the edge is perpendicular to the line of probes.

The remaining rows show the results for resistive sheets with a parabolic resistive taper. The steepness of the taper had little impact on the error. Unlike the error in the calculations for the uniform sheet, the error for the tapered sheets increases towards the center of the sheet where the resistivity is very small. This occurs because the current follows a path of least resistance which is near the center of the sheet.

Figures 4.3 and 4.4 show the voltage and magnitude of the sheet current density contour plots when the resistive sheet is $4\lambda \times 4\lambda$, has a constant resistivity of 2, is divided into a 41×41 grid, the current source is located at (18,16) and (24,16), and the voltage is measured between points (20,16) and (22,16). The next two figures (4.5 and 4.6) show the contour plots when the sheet has an $.01 + 3x^2$ resistive taper, the current source is at (18,16) and (24,16), and the voltage is measured between points (20,16) and (22,16). Notice how the sheet current density contour lines are influenced by the highly conductive center of the sheet. This influence creates errors in the measurements. The next four figures (Figures 4.7 to 4.10) show the contours when the measurements are done closer to the edge. The constant and tapered resistive sheets have very similar contours in this case. Although, some current still leaks through to the center of the tapered sheet.

source locations (n,m)	ΔV	I	Taper (η)	Actual R	Calculated R	% Error
18,21 24,21	2.2719	4.9649	constant	2.0	2.0370	1.85
18,10 24,10	2.2878	4.8965	constant	2.0	2.0799	4.00
18,4 24,4	2.4216	4.4843	constant	2.0	2.4039	20.20
15,21 27,21	1.8822	3.9590	constant	2.0	2.0067	0.00
15,4 27,4	2.2487	3.2936	constant	2.0	3.0393	51.97
4,21 10,21	2.2983	4.8033	constant	2.0	2.1300	6.50
4,4 10,4	2.4558	4.2883	constant	2.0	2.5493	27.47
18,10 24,10	2.1649	34.2168	$.01+x^2$	0.31	0.2817	9.14
18,4 24,4	2.2970	13.4987	$.01+x^2$	0.73	0.7575	3.77
18,10 24,10	2.1550	11.7415	$.01+3x^2$	0.92	0.8170	11.19
18,4 24,4	2.2943	4.5592	$.01+3x^2$	2.18	2.2402	2.76
18,16 24,16	1.9805	60.0656	$.01+3x^2$	0.20	0.1468	26.61

Table 4.2 — Comparison of the actual R for a $4\lambda \times 4\lambda$ sheet (41×41 grid) with that found by substituting the numerical calculations of ΔV and I into equation 4.1-10.
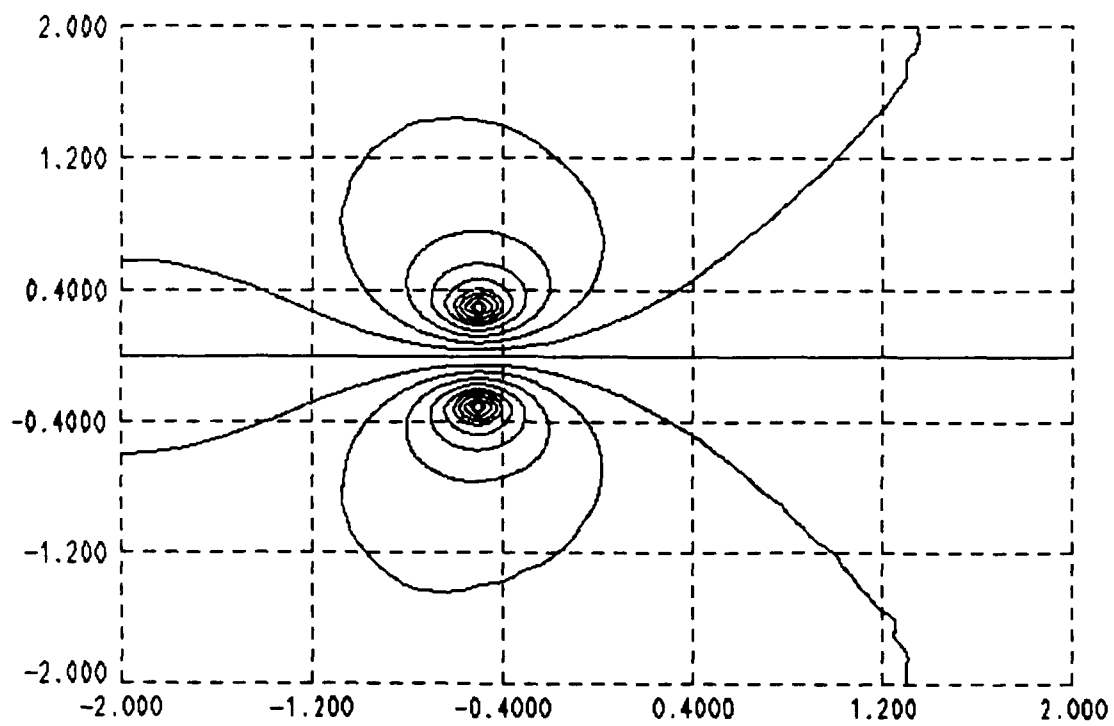
Figure 4.3 — Voltage contours for a $4\lambda \times 4\lambda$ sheet (41×41 grid) with $\eta = 2$, the current source at at (18,16) and (24,16), and ΔV measured between (20,16) and (22,16).
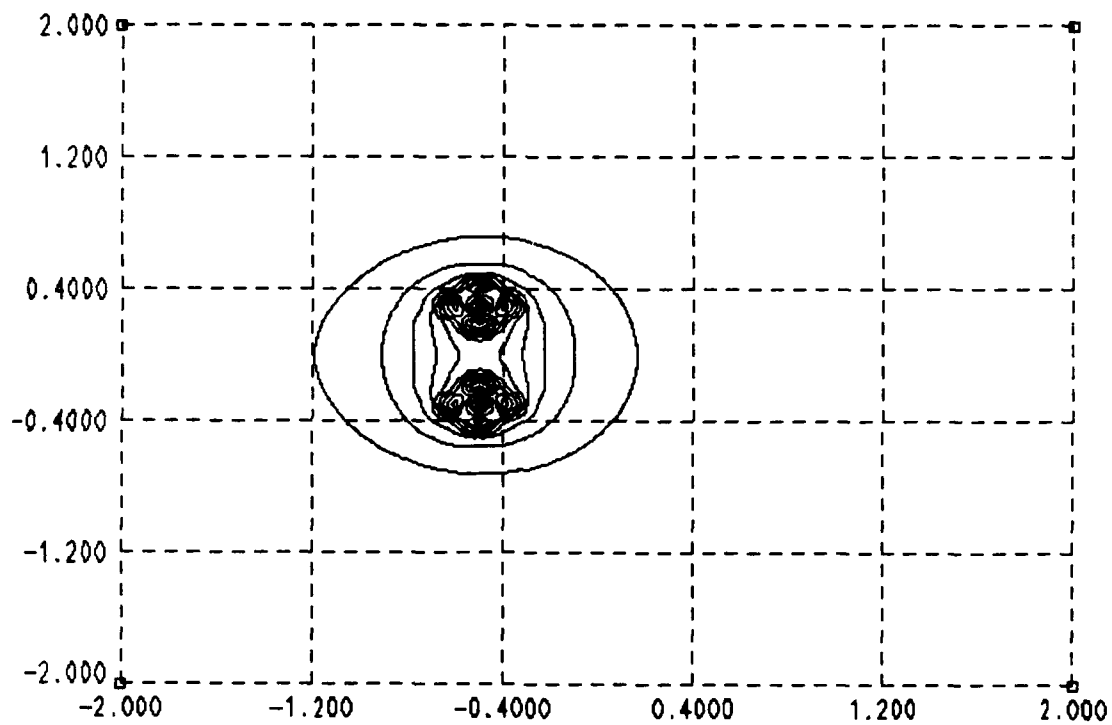
Figure 4.4 — $|\overline{J}|$ contours for a $4\lambda \times 4\lambda$ sheet (41×41 grid) with $\eta = 2$, the current source at at (18,16) and (24,16), and ΔV measured between (20,16) and (22,16).
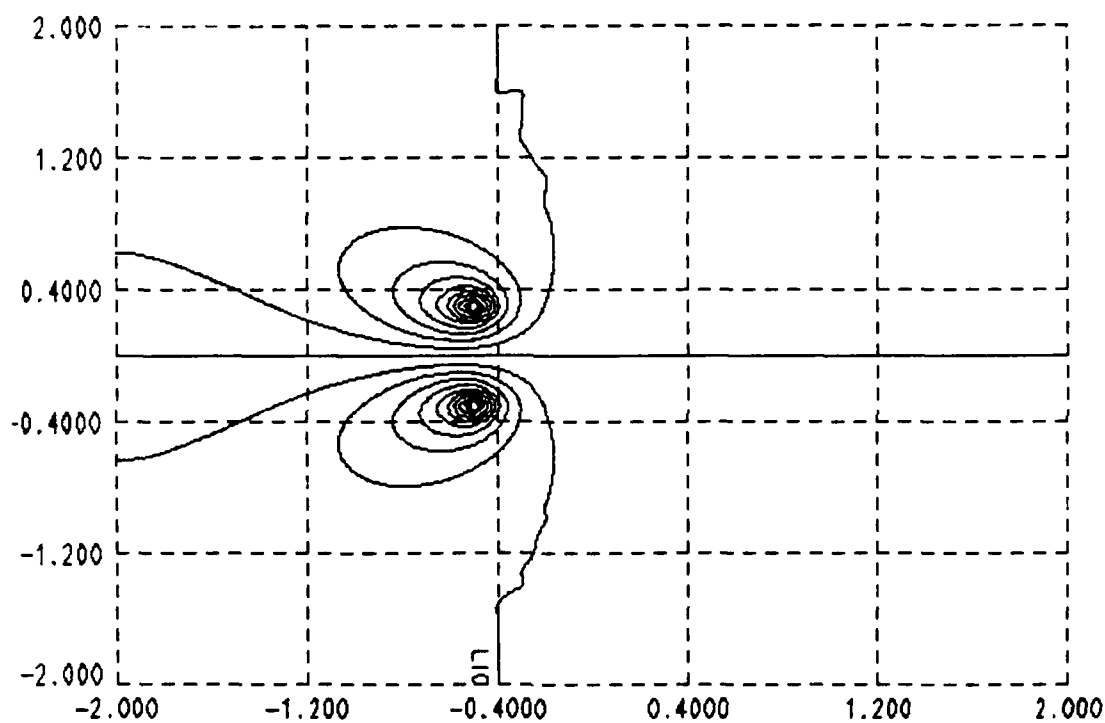
Figure 4.5 — Voltage contours for a $4\lambda \times 4\lambda$ sheet (41×41 grid) with $\eta = .01 + 3x^2$, the current source at at (18.16) and (24,16), and ΔV measured between (20.16) and (22,16).
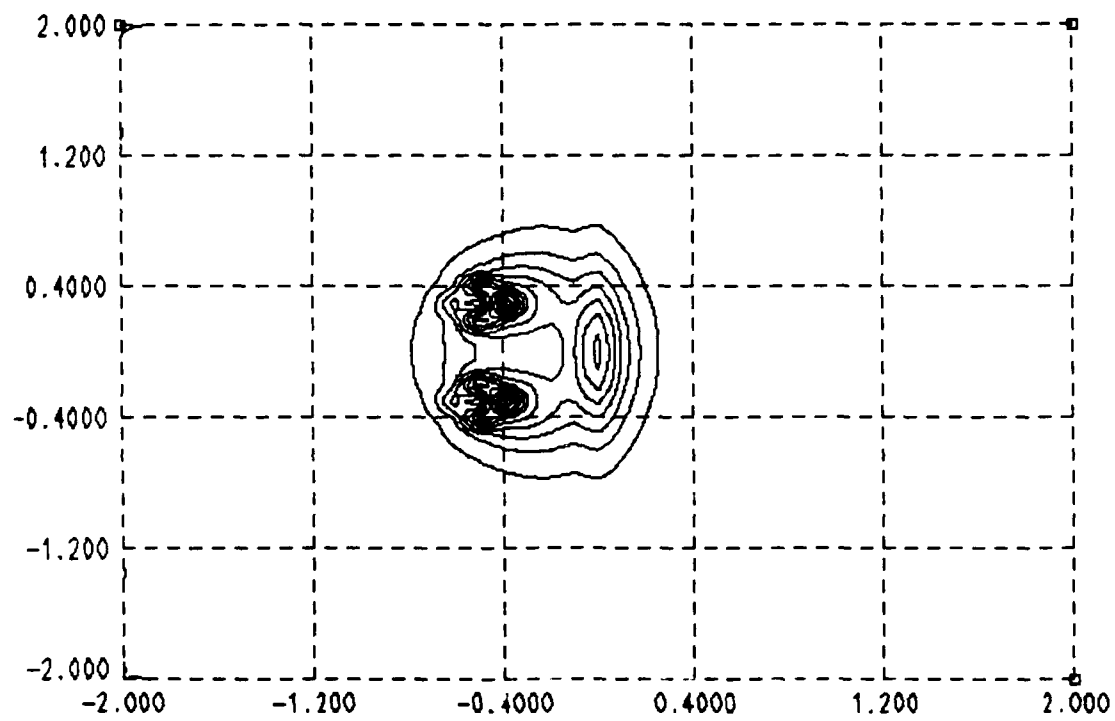
Figure 4.6 — $|\bar{J}|$ contours for a $4\lambda \times 4\lambda$ sheet (41×41 grid) with $\eta = .01 - 3x^2$, the current source at at (18,16) and (24,16), and ΔV measured between (20,16) and (22,16).
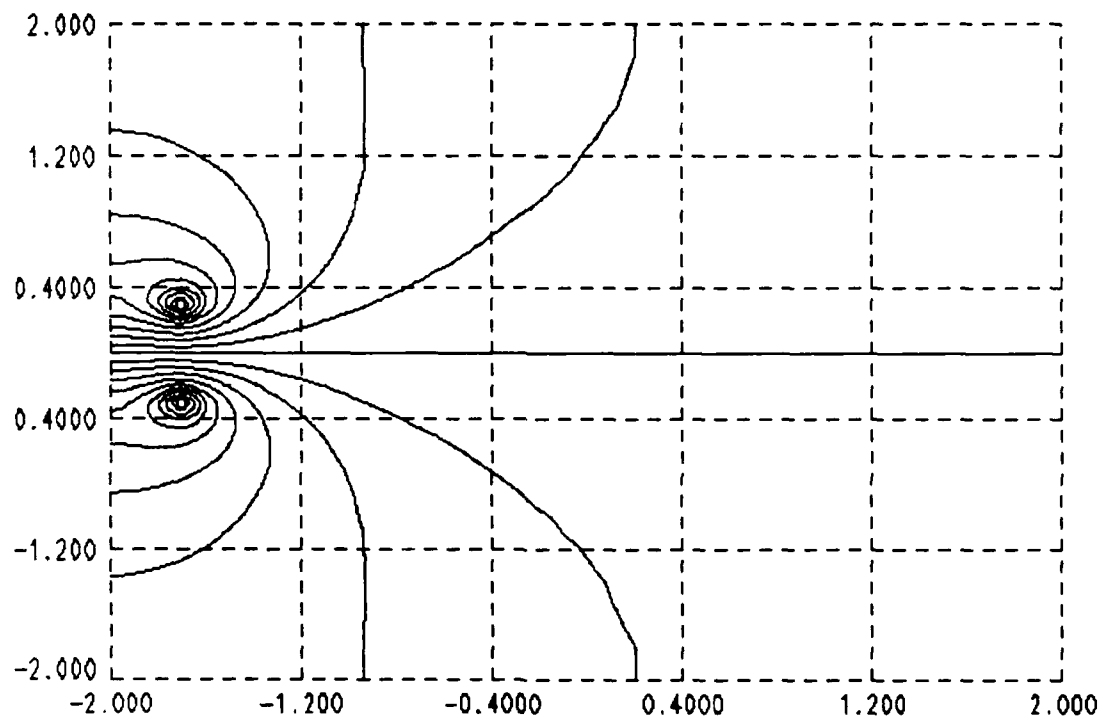
Figure 4.7 — Voltage contours for a $4\lambda \times 4\lambda$ sheet $(41 \times 41$ grid) with $\eta = 2$, the current source at at (18,4) and (24,4), and ΔV measured between (20,4) and (22,4).

Figure 4.8 — $|\overline{J}|$ contours for a $4\lambda \times 4\lambda$ sheet (41×41 grid) with $\eta = 2$, the current source at at (18,4) and (24,4), and ΔV measured between (20,4) and (22,4).

Figure 4.9 — Voltage contours for a $4\lambda \times 4\lambda$ sheet (41×41 grid) with $\eta = .01 - 3r^2$, the current source at at (18,4) and (24,4), and $\triangle V$ measured between (20,4) and (22,4).
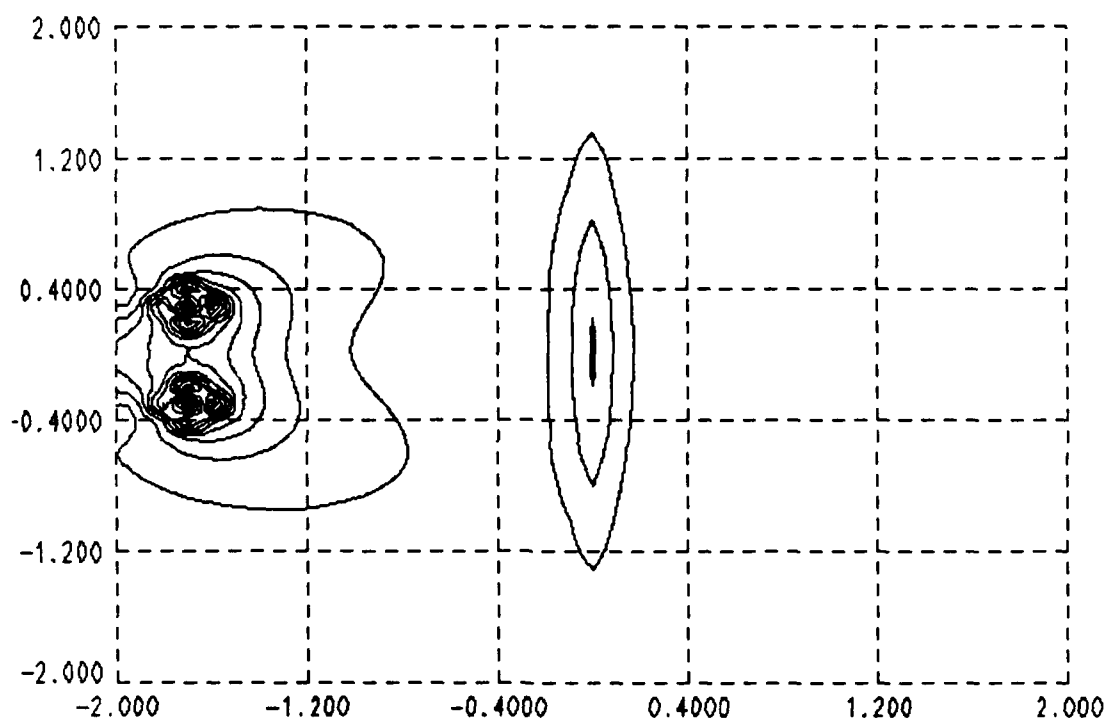
Figure 4.10 — $|\overline{J}|$ contours for a $4\lambda \times 4\lambda$ sheet $(41 \times 41$ grid) with $\eta = .01 + 3x^2$, the current source at at (18,4) and (24,4), and ΔV measured between (20,4) and (22,4).

CHAPTER V

EFFECTS OF ERRORS IN THE RESISTIVE TAPER ON THE FARFIELD SCATTERING PATTERNS

The theoretical low sidelobe resistive tapers derived in Chapter 3 have practical limitations. Tolerances in the metal deposition and resistivity measurement processes will introduce a certain range of errors in the resistive taper. These errors are modeled as random and/or correlated and cause the induced surface current density to deviate from the desired surface current density. In turn, the scattering pattern sidelobes differ form those calculated from the no-error resistive taper. The extent of the errors determines the lowest possible average sidelobe level in the scattering patterns of the strip.

This chapter begins with a review of error tolerance theory in electromagnetics. From there, the error models for the resistivity, PO and integral equation surface current densities, and bistatic scattering and backscattering patterns are derived. An rms average error level is calculated and tabulated for several tapered resistive strips. Computer plots show the error and error-free resistivity, current density and scattering patterns from the PO and integral equation approaches, as well as the isolated contributions from the errors alone.

5.1 Background

Relating errors in a resistive taper to perturbations in the scattering patterns of a strip is a new area of study. Similar topics that have been investigated include antenna error tolerance theory and rough-surface scattering. In particular, phased array error theory provides the most relevant background here.

The classic paper on antenna tolerance theory was written by Ruze [1966]. He theoretically and experimentally modeled the impact of surface errors on the gain and far field

100

pattern of a reflector antenna. The reflector is divided into N correlated regions with any one region being statistically independent from any other region. These correlation regions (dents in the reflector) are assumed to cause normal- or Gaussian-shaped distortions to the phase front. Their impact on the far field pattern is a function of the number and size of dents as well as the size and efficiency of the antenna aperture. Further extensions of this work have appeared more recently in the literature [Tripp, 1984].

The Ruze model takes into account phase errors in the aperture distribution, but not amplitude errors. Although a phase error model applies when the strip has wrinkels or indentations, or when the resistive taper is complex (as in the nulling problem), the main impetus here is how errors in the imaginary part of the dielectric constant (real part of the resistivity) alter the induced surface current density and far field scattering patterns. Errors in the imaginary part of the permitivity, ϵ'', predominantly result in amplitude errors in the surface current density. As such, past work on the impact of current amplitude errors on the far field pattern of an antenna has the most application in this situation.

Several sources in the literature analyze the effects of random phase and amplitude errors in the element excitations of an array on the array's far field pattern [Collin and Zucker, 1969; Mailloux, 1982]. From sampling theory, if N normally distributed random variables with mean of 0 and variance of δ^2 are averaged, then the average is normally distributed with a mean of 0 and a standard deviation of $\frac{\delta^2}{N}$. Since the current is tapered, the random variables do not have equal weighting. To compensate, the variance is also divided by the taper efficiency. The taper efficiency is a measure of how well the aperture collimates the radiated energy and is defined as the ratio of the directivity to the directivity of an identical aperture with uniform amplitude and phase. An array with random phase and amplitude errors has an average relative sidelobe power level (f^2) at a null in the no-error pattern given by

$$f^2 = \frac{\delta_a^2 + \delta_p^2}{N \eta_t} \tag{5.1-1}$$

where

$$\delta_a^2 = \text{amplitude error variance normalized to unity}$$

$$\delta_p^2 = \text{phase error variance(in radians)}$$

$$N = \text{number of elements in array}$$

$$\eta_t = \text{array taper efficiency}$$

Equation (5.1-1) states that random current errors by themselves (like white noise) have a flat Fourier Transform with a height of f^2. The height of the transform is inversely proportional to the number of samples (N) and the taper efficiency (η_t).

Unlike random errors, correlated errors have a response that peaks near the main beam and dies-off far from the main beam. An example of this type of error occurs when a scattering pattern is not measured in the far field. The resulting quadratic phase error across the test object fills-in nulls close to the main beam and expands the main beam. This error is noticeable in the experimental bistatic scattering results for a tapered sheet in Chapter 6.

Brookner[1975] gives a formula for the rms relative sidelobe level of the correlated errors due to subarraying:

$$f^2 = \frac{\delta_{sa}^2 + \delta_{sp}^2}{N_s \eta_t} \qquad (5.1\text{-}2)$$

but the extent of the errors is limited to

$$\frac{-1}{\sqrt{n_e}} \leq \theta \leq \frac{1}{\sqrt{n_e}}$$

where

δ^2_{sa} =amplitude error variance at the subarray port normalized to unity

δ^2_{sp} =phase error variance at the subarray port (in radians)

N_s =number of subarrays in array

n_e =number of elements in subarray

η_t =array efficiency

θ =angle from array broadside(in radians)

From the above equations one may conclude that random errors predominantly alter the far field pattern far from the main beam, whereas correlated errors predominantly alter the far field pattern close to the main beam. As a result, these equations predict the impact of the errors on the far field pattern whether only one occurs or both occur.

The effects of surface roughness and changing dielectric properties on scattering patterns is discussed in the literature [Beckmann and Spizzichino, 1987 ;Ulaby, Moore, and Fung, 1982]. These results apply to scattering from vegetation, earth surface, etc. They are not as applicable to "hard targets" such as the strip as the above are.

5.2 Modeling Resistivity Errors

Derivations in the resistive taper on a strip (resistivity errors) arise from the manufacturing and resistivity measurement processes. Blotching of the conductive material, inaccuracies in the deposition process, and possibly quantization errors, if only certain levels of resistivity are possible, limit the accuracy of depositing a fine coat of conductive material on a thin dielectric substrate having the imaginary part of $\eta=0$. Poor contacts between the measuring probe and the resistive surface, difficulties with measuring a resistive taper (Chapter 4), and equipment limitations produce errors in the resistivity measurement process. Accurately determining and classifying the errors in a resistive taper requires extensive experimental analysis of the manufacturing and measuring processes. In lieu of such an experimental analysis the errors are theoretically modeled and their impact on the scattering pattern of a strip are calculated.

Both error sources depend on the level of resistivity. The metal deposition process has an associated tolerance that is a function of the resistivity. Accurately depositing a thick coating of metal to obtain a low resistivity ($\eta \approx 0$) is much easier than accurately depositing a very sparse coating of metal to obtain a high resistivity ($\eta \approx 4$). The resistivity measurement process also has an error that is a function of the resistivity. Because there is a poor contact between the probes and the surface, accurate measurement of a high resistivity is much more difficult than a low resistivity, Since both error sources are a function of the resistivity level, the magnitude of the error should likewise be modeled as a function of the resistivity. In other words, smaller values of resistivity are prone to smaller errors and larger values of resistivity are prone to larger errors.

As in antenna theory, it is convenient to classify errors as either random or correlated. Random or uncorrelated means the errors on one part of the strip are totally independent from errors on another part of the strip. Correlated means the errors in a certain region of the strip are related. The region where this relationship holds is called the correlation region.

The actual resistive taper (η) on a strip is composed of the theoretical taper (η_o) plus perturbations (δ) to that taper due to manufacturing errors.

$$\eta(x) = \eta_o(x) + \delta(x) \tag{5.2-1}$$

The perturbations may be due to either correlated or random errors.

Both the random and correlated error models divide the strip into N small correlation regions over which the error is constant. On the one hand, the random error model assumes the errors assigned to the N correlation regions are all statistically independent. On the other hand, the correlated error model assumes the errors assigned to the N correlation regions are all related by a function. The two models are described in greater detail in the following subsections.

5.2.1 Modeling Random Errors in the Resistive Taper

Random errors are assumed to follow a normal probability density function (pdf) with a mean of 0.0 and a standard deviation of $\sigma_k \eta_o(x)$, where σ_k is a constant between 0.0 and 0.3. The upper limit of 0.3 is due to the definition of standard deviation. Since 99% of

the samples of a normal pdf are within 3 standard deviations on either side of the mean and since the negative values of resistivity are not allowed, then $\eta_o(x) - 3\sigma_k\eta_o(x)$ must be greater than 0. A value of $\sigma_k=0.3$ allows a small safely margin to insure no negative values of resistivity are generated.

5.2.2 Correlated errors in the Resistive Taper

Two correlated error models are considered:

1. $e(x) = c\left|\dfrac{x}{2a}\right|^q \eta_o(x)$ (5.2-2)

2. $e(x) = c\cos\left[2\pi\left(\dfrac{qx}{2a}\right)\right]\eta_o(x)$ (5.2-3)

where c and q are constants.

These equations are continuous, but their digital implementations are not. Hence, not only is the whole strip one correlation region, but it is also divided into N smaller correlation regions with each region having a constant resistivity. If the N correlation regions are small enough, then the error function appears continuous and the effects of these correlation regions are small and can be ignored.

5.3 Modeling Surface Current Density Errors

As with resistivity, the surface current density is separated into a desired surface current density (J_o) plus a perturbation (ξ).

$$J(x) = J_o(x) + \xi(x) \qquad (5.3-1)$$

The desired surface current density arises only from the no-error taper, while the current perturbation arises only form the resistivity errors. In either case, it should be noted that the current perturbation is a function of the resistivity perturbation and the quiescent resistive taper, not just the resistivity perturbation alone.

Errors in the induced surface current density are calculated from the errors in the resistive taper by two methods: integral equation and physical optics. Both approaches yield very similar results. The errors are modeled as real numbers, since they occur only in

the metal deposited on the substrate and not in the dielectric substrate. The errors may be either correlated or random.

5.3.1 Integral Equation Formulation of the Current Perturbations

The errors in the surface current density relate to the errors in the resistive taper via the integral equations derived in Chapter 2. Substituting (5.2-1) and (5.3-1) into the right-hand-side of (2.1-11) gives

$$\eta_o(x)J_z(x)+\frac{k}{4}\int_{-a}^{a}J_z(x')H_o^{(2)}(k|x-x'|)dx' = (\eta_o(x)+\delta(x))(J_{oz}(x)+\xi(x))$$
$$+\frac{k}{4}\int_{-a}^{a}(J_{oz}(x')+\xi(x'))H_o^{(2)}(k|x-x'|)dx' \tag{5.3-2}$$

This E-polarization equation may be simplified to the form

$$\eta_o(x)\xi(x)+\frac{k}{4}\int_{-a}^{a}\xi(x')H_o^{(2)}(k|x-x'|)dx' = -\delta(x)J_o(x) \tag{5.3-3}$$

The same procedure for H-polarization yields

$$\eta_o(x)\xi(x)+\frac{k}{4}\int_{-a}^{a}\xi(x')\frac{1}{k|x-x'|}H_1^{(2)}(k|x-x'|)dx' = -\delta(x)J_o(x) \tag{5.3-4}$$

These equations have the same form as the integral equations in Chapter 2, so they may be solved with the same numerical methods. All the variables are known except for the current perturbation.

5.3.2 PO Formulation of the Current Perturbations

The errors in the surface current density relate to the errors in the resistive taper through the PO equations derived in Chapter 2. For E-polarization the PO surface current density due to errors in the resistive taper is given by

$$\xi_z(x) + J_{oz}(x) = \frac{\sin\phi_o}{.5 + [\eta_o(x) + \delta(x)]\sin\phi_o}e^{jkx\cos\phi_o} \tag{5.3-5}$$

Substituting (2.1-29) for $J_{oz}(x)$ and solving for the current perturbations results in

$$\xi_z(x) = \frac{-\delta(x)\sin^2\phi_o}{[.5 + \eta_o(x)\sin\phi_o]^2 + \delta(x)\sin\phi_o[.5 + \eta_o(x)\sin\phi_o]}e^{jkx\cos\phi_o} \tag{5.3-6}$$

Assuming small resistivity perturbations such that

$$[.5 + \eta_o(x)sin\phi_o]^2 >> \delta(x)sin\phi_o[.5 + \eta_o(x)sin\phi_o] \tag{5.3-7}$$

or

$$\eta_o(x) + \frac{1}{2sin\phi_o} >> \delta(x) \tag{5.3-8}$$

An approximation to the surface current perturbation is given by

$$\xi_z(x) \approx \frac{-\delta(x)sin\phi_o}{[.5 + \eta_o(x)sin\phi_o]^2}e^{jkxcos\phi_o} \tag{5.3-9}$$

At normal incidence the current perturbation approximately equals the negative of the resistivity perturbation times the no-error current squared.

$$\xi_z(x) \approx -\delta(x)\Big[J_o(x)\Big]^2 = \frac{-\delta(x)}{[\eta(x) + .5]^2} \tag{5.3-10}$$

The H-polarization PO current perturbation is derived in the same manner.

$$\xi_x(x) = \frac{-\delta(x)\sin\phi_o}{[\eta_o(x) + .5\sin\phi_o]^2 + \delta(x)[\eta_o(x) + .5\sin\phi_o]}e^{jkxcos\phi_o} \tag{5.3-11}$$

When the current perturbations are small the equation simplifies to

$$\eta_o(x) + \frac{1}{2}sin\phi_o >> \delta(x) \tag{5.3-12}$$

Unlike (5.3-9), this equation has a $\sin\phi_o$ factor in the numerator rather than the denominator. Thus, as ϕ_o increases, (5.3-8) becomes a better approximation while (5.3-12) becomes a worse approximation. Care should be exercised when applying this result. When this approximation is assumed, the current perturbation is given by

$$\xi_x(x) = \frac{-\delta(x)\sin\phi_o}{[\eta_o(x) + .5\sin\phi_o]^2}e^{jkxcos\phi_o} \tag{5.3-13}$$

At normal incidence this equation reduces to (5.3-10).

Equations (5.3-10) and (5.3-13) show that at normal incidence the surface current perturbation is proportional to the resistivity perturbation, while it is inversely proportional

to the square of the resistive taper plus 0.5. In logarithmic form the magnitude of (5.3-10) is given by

$$\log |\xi| = \log |\delta| - 2\log |(\eta + .5)| \tag{5.3-14}$$

This form of the equation simply shows that δ is the dominant contributor for smaller values of the resistive taper $(\eta < \frac{1}{\sqrt{\delta}} - .5)$, and η is the dominant contributor for larger values of the resistive taper $(\eta > \frac{1}{\sqrt{\delta}} - .5)$ given that $\eta + \delta >> .5$.

5.4 Modeling Errors in the Scattering Patterns

The RCS of a strip with resistive errors is given by

$$\sigma = \sigma_o + \sigma_{err} \tag{5.4-1}$$

where σ_o is the no-error RCS and σ_{err} is the RCS due to the errors alone. Substituting the error currents from section 5.3 into the (2.4-4) and (2.4-5) yields

E-polarization:

$$\sigma_E(\phi) = \frac{k}{4} \left| \int_{-a}^{a} J_{oz}(x')e^{jkx'\cos\phi}dx' + \Delta \sum_{r=1}^{N} \xi_n e^{jkx\,n\cos\phi} \right|^2 \tag{5.4-2}$$

H-polarization:

$$\sigma_H(\phi) = \frac{k}{4}\sin^2\phi_o \left| \int_{-a}^{a} J_{ox}(x')e^{jkx'\cos\phi}dx' + \Delta \sum_{n=1}^{N} \xi_n e^{jkx\,n\cos\phi} \right|^2 \tag{5.4-3}$$

where Δ is the length of the integration region. The deviations in the scattering patterns may be isolated by completing the squares in the RCS formulas.

E-polarization:

$$
\begin{aligned}
\sigma_E(\phi) =& \frac{k}{4} \left| \int_{-a}^{a} J_{oz}(x')e^{jkx'\cos\phi}dx' \right|^2 + \\
& \frac{\Delta k}{2} Real\left\{ \int_{-a}^{a} J_{oz}(x')e^{jkx'\cos\phi}dx' \right\} Real\left\{ \sum_{n=1}^{N} \xi_n e^{jkx\,n\cos\phi} \right\} + \\
& \frac{\Delta k}{2} Imaginary \left\{ \int_{-a}^{a} J_{oz}(x')e^{jkx'\cos\phi}dx' \right\} Imaginary \left\{ \sum_{n=1}^{N} \xi_n e^{jkx\,n\cos\phi} \right\} + \\
& \frac{\Delta^2 k}{4} \left| \sum_{n=1}^{N} \xi_n e^{jkx\,n\cos\phi} \right|^2
\end{aligned}
\tag{5.4-4}
$$

H-polarization:

$$\sigma_H(\phi) = \frac{k}{4}\sin^2\phi_o \left| \int_{-a}^{a} J_{ox}(x')e^{jkx'\cos\phi}dx' \right|^2 +$$

$$\frac{\Delta k}{2}\sin^2\phi_o Real\left\{ \int_{-a}^{a} J_{ox}(x')e^{jkx'\cos\phi}dx' \right\} Real\left\{ \sum_{n=1}^{N} \xi_n e^{jkx_n\cos\phi} \right\} +$$

$$\frac{\Delta k}{2}\sin^2\phi_o Imaginary\left\{ \int_{-a}^{a} J_{ox}(x')e^{jkx'\cos\phi}dx' \right\} Imaginary\left\{ \sum_{n=1}^{N} \xi_n e^{jkx_n\cos\phi} \right\} +$$

$$\frac{\Delta^2 k}{4}\sin^2\phi_o \left| \sum_{n=1}^{N} \xi_n e^{jkx_n\cos\phi} \right|^2 \tag{5.4-5}$$

The first term in (5.4-4) and in (5.4-5) is the RCS due to the desired resistive tapers (σ_o). The remaining three terms (σ_{err}) are due to the errors in the taper. When the errors are small, the fourth term has a much lower average level than the other terms. Generally, the last three terms combined are much smaller than the first. The exception is in the nulls and low sidelobe regions of the RCS patterns. There, the level of the error terms may exceed the desired RCS.

5.5 Average Error Levels in the Scattering Patterns Due to Random Resistivity Errors

No obvious way exists to simply relate the resistivity error level to the current error level. For small resistive errors at normal incidence, (5.3-10) gives a reasonable estimate for the PO current error, if η and δ are replaced by their respective averages. Otherwise, the average rms current error is found by solving one of the current perturbation equations in section 5.3 and dividing the sum of the absolute values of the ξ's by $\sqrt{N}$.

After estimating the average rms current perturbation, two methods are used to find an estimate of the error levels in the scattering patterns. The first calculates average rms bistatic scattering (σ_{bi}) and backscattering (σ_{bk}) errors from the calculated error and no-error scattering patterns. This method provides accurate error information for all bistatic angles and for backscattering and may also be used for evaluating the impact of correlated resistive errors. The second only estimates the error level of the bistatic scattering pattern at a null in the error-free bistatic scattering pattern. This method is very similar to the

method used in array theory, (see (5.1-1)). It has the advantage of being much simpler to calculate than the first method.

5.5.1 Average RMS Errors

The average RMS error is defined by

$$\sigma_{av} = \sqrt{\frac{\sum_{i=1}^{N}[z_o(i) - z_e(i)]^2}{N}} \tag{5.5-1}$$

where

z_o = no-error quantity

z_e = error quantity

N = number of correlated regions

The constant σ_{av} may be one of the following:

σ_{res} = average RMS resistivity error

σ_{cur} = average RMS surface current density error

σ_{bi} = average RMS bistatic scattering error

σ_{bk} = average RMS backscattering error

The computer is used to generate random numbers that have a normal pdf with a mean of 0 and a standard deviation of $\sigma_N(x)$. Since it has already been assumed that the errors are a function of the resistive taper, the standard deviation for the resistive error at a point x along the strip is given by

$$\sigma_N(x) = \sigma_k \eta(x) \tag{5.5-2}$$

where σ_k is a constant such that $0 \leq \sigma_k \leq 0.3$. When $\eta(x) = 1$ then $\sigma_{res} \approx \sigma_k$, otherwise, the two constants differ.

No obvious way exists to accurately predict σ_{cur}, σ_{bi}, or σ_{bk} from σ_{res} for either the PO or integral equation approaches. Instead, σ_{cur}, σ_{bi}, and σ_{bk} are found by substituting the appropriate error and no-error quantities into (5.5-1). Table 5.1 and 5.2 display typical

examples of these quantities for a 4λ and a 6λ strip. These tables compare the impact of polarization, type of resistive taper, number of segments, method used to calculate the surface current density, length of strip, and level of σ_k on the RMS errors.

The tables bring several observations to light:

1. The integral equation and PO approaches agree much better when $\sigma_k=.15$ than when $\sigma_k=.3$. Large changes in the resistivity create large discontinuities which is the condition when PO and the integral equation approaches do not agree as well.

2. The agreement between the two approaches does not increase as the resistivity increases, because the magnitude of the error is a function of the resistivity. If the magnitude of the resistive error remains constant as the resistive taper increases, then agreement between the two approaches does get closer.

3. The magnitude of σ_{res} increases as σ_k and/or η increases.

4. σ_{bi} and σ_{bk} are greater for the larger strip than for the smaller strip.

5. The magnitude of σ_{bk} is smaller than σ_{bi}.

5. As N increases σ_{res} and σ_{cur} approach their limiting values and σ_{bi} and σ_{bk} decrease. In these examples the bistatic scattering and backscattering patterns are calculated at 1° increments form 0° to 90°.

One can calculate the average rms RCS error from σ_{bi} or σ_{bk} by using one of the following equations:

$$\sigma_E = \frac{\Delta^2 \pi \sigma_b^2}{2} \qquad (5.5\text{-}2)$$

$$\sigma_H = \frac{\Delta^2 \pi \sigma_b^2 \sin^2 \phi_o}{2} \qquad (5.5\text{-}3)$$

where the "b" in σ_b stands for either "bi" or "bk". This error measurement is $>$ the error measurement in the next section, because this error measurement takes all three error terms of (5.4-4) and (5.4-5) into account while the error measurement in the next section only takes the last term into account.

5.5.1.2 Average RMS Sidelobe Level at a Null in the Error-Free Pattern

This analysis develops simple equations for estimating the average rms bistatic scattering sidelobe level at a null in the error-free scattering pattern. Consider (5.4-4) and (5.4-5) at a null in the error-free pattern. In other words when

E-polarized RMS error averaged over 10 samples										
					Integral Equation			Physical Optics		
η	N	2a	$\cdot$	σ_{RES}	σ_{CUR}	σ_{BI}	σ_{BK}	σ_{CUR}	σ_{BI}	σ_{BK}
1.0	40	4λ	.15	.1575	.1005	.0307	.0273	.0748	.0340	.0254
	60	4λ	.15	.1489	.1007	.0246	.0217	.0702	.0246	.0197
2.0	40	4λ	.15	.3151	.0662	.0234	.0215	.0553	.0254	.0203
	60	4λ	.15	.2979	.0639	.0186	.0177	.0518	.0186	.0158
30dB $\bar{n}=8$	40	4λ	.15	.0962	.0870	.0215	.0200	.0595	.0252	.0178
Taylor	60	4λ	.15	.0884	.0946	.0171	.0163	.0545	.0175	.0138
40dB $\bar{n}=12$	40	4λ	.15	.2242	.0840	.0206	.0193	.0571	.0238	.0172
Taylor	60	4λ	.15	.2078	.0838	.0145	.0142	.0498	.0161	.0124
1.0	40	4λ	.3	.3125	.2752	.0917	.0788	.1814	.0876	.0642
	60	4λ	.3	.2980	.2867	.0824	.0687	.1683	.0669	.0506
2.0	40	4λ	.3	.6250	.2119	.0836	.0739	.1519	.0754	.0581
	60	4λ	.3	.5961	.2079	.0724	.0619	.1393	.0588	.0453
30dB $\bar{n}=8$	40	4λ	.3	.1903	.1967	.0542	.0480	.1300	.0581	.0405
Taylor	60	4λ	.3	.1791	.2296	.0564	.0488	.1240	.0469	.0344
40dB $\bar{n}=12$	40	4λ	.3	.4426	.1947	.0576	.0521	.1278	.0587	.0417
Taylor	60	4λ	.3	.4194	.2040	.0504	.0449	.1149	.0436	.0318
1.0	40	6λ	.3	.3125	.2255	.1173	.1027	.1814	.1412	.0933
	60	6λ	.3	.2980	.2510	.1039	.0907	.1683	.1032	.0743
	90	6λ	.3	.2986	.2877	.1118	.0915	.1678	.0871	.0643
2.0	40	6λ	.3	.6250	.1824	.1122	.0989	.1519	.1219	.0857
	60	6λ	.3	.5961	.1909	.0939	.0838	.1393	.0877	.0668
	90	6λ	.3	.5972	.2080	.0941	.0784	.1387	.0753	.0574
30dB $\bar{n}=8$	40	6λ	.3	.1903	.1538	.0741	.0661	.1300	.0915	.0613
Taylor	60	6λ	.3	.1791	.1887	.0726	.0631	.1240	.0732	.0507
	90	6λ	.3	.1888	.2547	.0823	.0692	.1326	.0662	.0476
40dB $\bar{n}=12$	40	6λ	.3	.4426	.1523	.0762	.0706	.1278	.0985	.0644
Taylor	60	6λ	.3	.4194	.1712	.0671	.0604	.1149	.0681	.0480
	90	6λ	.3	.4352	.2373	.0770	.0645	.1263	.0639	.0461

Table 5.1 — The average RMS error for a resistive strip when the incident field is

E-polarized

					Integral Equation			Physical Optics		
η	N	2a	σ_k	σ_{RES}	σ_{CUR}	σ_{BI}	σ_{BK}	σ_{CUR}	σ_{BI}	σ_{BK}
1.0	40	4λ	.15	.3125	.1369	.0619	.0531	.1814	.0684	.0625
	60	4λ	.15	.2980	.0982	.0465	.0398	.1683	.0570	.0489
2.0	40	4λ	.15	.6250	.1301	.0549	.0464	.1519	.0601	.0529
	60	4λ	.15	.5961	.0948	.0400	.0330	.1393	.0503	.0416
30dB $\bar{n}=8$	40	4λ	.15	.1903	.0985	.0453	.0426	.1300	.0419	.0429
Taylor	60	4λ	.15	.1791	.0735	.0329	.0320	.1240	.0365	.0345
40dB $\bar{n}=12$	40	4λ	.15	.4426	.0941	.0434	.0440	.1278	.0416	.0450
Taylor	60	4λ	.15	.4194	.0713	.0295	.0312	.1149	.0330	.0321
1.0	40	4λ	.3	.1575	.0652	.0258	.0226	.0748	.0247	.0232
	60	4λ	.3	.1489	.0473	.0204	.0178	.0702	.0200	.0180
2.0	40	4λ	.3	.3151	.0549	.0195	.0167	.0553	.0188	.0169
	60	4λ	.3	.2979	.0428	.0153	.0129	.0518	.0153	.0132
30dB $\bar{n}=8$	40	4λ	.3	.0962	.0488	.0207	.0190	.0595	.0175	.0184
Taylor	60	4λ	.3	.0884	.0347	.0141	.0135	.0545	.0129	.0135
40dB $\bar{n}=12$	40	4λ	.3	.2242	.0457	.0188	.0193	.0571	.0161	.0175
Taylor	60	4λ	.3	.2078	.0328	.0126	.0137	.0498	.0116	.0116
1.0	40	6λ	.3	.3125	.1819	.1024	.0874	.1814	.0972	.0911
	60	6λ	.3	.2980	.1299	.0727	.0626	.1683	.0785	.0723
	90	6λ	.3	.2986	.0962	.0560	.0470	.1678	.0744	.0627
2.0	40	6λ	.3	.6250	.1645	.0906	.0775	.1519	.0846	.0771
	60	6λ	.3	.5961	.1219	.0640	.0545	.1393	.0685	.0607
	90	6λ	.3	.5972	.0933	.0479	.0393	.1387	.0649	.0532
30dB $\bar{n}=8$	40	6λ	.3	.1903	.1282	.0706	.0675	.1300	.0619	.0659
Taylor	60	6λ	.3	.1791	.0963	.0508	.0483	.1240	.0521	.0517
	90	6λ	.3	.1888	.0735	.0462	.0435	.1326	.0537	.0481
40dB $\bar{n}=12$	40	6λ	.3	.4426	.1233	.0726	.0694	.1278	.0635	.0696
Taylor	60	6λ	.3	.4194	.0914	.0474	.0456	.1149	.0479	.0490
	90	6λ	.3	.4352	.0726	.0428	.0421	.1263	.0511	.0464

H-polarized RMS error averaged over 10 samples

Table 5.2 — The average RMS error for a resistive strip when the incident field is

H-polarized

$$\int_{-a}^{a} J_{os}(x')e^{jkx'\cos\phi}dx' = 0 \qquad (5.5\text{-}4)$$

where s=z for E-polarization and s=x for H-polarization. Now, the first three terms in both equations vanish, leaving only the fourth term. Since the H-polarization is the same as the E-polarization term except for a $\sin^2\phi_o$, the remaining part of the development is done only for E-polarization. Expand the fourth term as follows:

$$
\begin{aligned}
\left| \sum_{n=1}^{N} \xi_n e^{jkx_n\cos\phi} \right|^2 &= \sum_{n=1}^{N} \xi_n e^{jkx_n\cos\phi} \sum_{m=1}^{N} \xi_m^* e^{-jkx_m\cos\phi} \\
&= \sum_{n=1}^{N} |\xi_n|^2 + \sum\sum_{n=m} \xi_m^* \xi_n e^{jk(x_n-x_m)\cos\phi} \\
&\approx \sum_{n=1}^{N} |\xi_n|^2 \qquad (5.5\text{-}5)
\end{aligned}
$$

where * denotes complex conjugate. Substituting from (5.5-1), $\sum_{n=1}^{N} |\xi_n|^2 = N\sigma_{cur}^2$, gives

$$\sigma_{binE}^2 = \Delta^2 N\sigma_{cur}^2 = \frac{(2a)^2\sigma_{cur}^2}{N} \qquad (5.5\text{-}6)$$

$$\sigma_{binH}^2 = \frac{(2a)^2\sigma_{cur}^2\sin^2\phi_o}{N} \qquad (5.5\text{-}7)$$

The subscripts binE and binH stand for bistatic scattering level at the null of the error-free pattern E- and H-polarization, respectively.

When the strip is perfectly conducting or has a very light resistive taper the scattering patterns do not have distinct nulls (e.g. Figures 3.1 and 3.2). However, the error sidelobe level is only of concern when the sidelobes are low or the strip has a heavy resistive taper, in which case the low sidelobe and large constant resistive tapers do have distinct nulls (e.g. Figures 3.5 and 3.20).

Sometimes it is of interest to calculate the error sidelobe level relative to the peak of the main beam. At normal incidence, the peak of the electric field far from the strip is given by

$$\int_{-a}^{a} J_{oz}(x')dx' + \Delta \sum_{n=1}^{N} \xi_n \approx \Delta \sum_{n=1}^{N} [J_{oz}(x_n) + \xi_n] \qquad (5.5\text{-}8)$$

Since the ξ_n are normally distributed rv's with a mean on 0, then $\sum_{n=1}^{N} \xi_n \approx 0$, and the far field power pattern at the peak of the main beam (P_{MB}) reduces to

$$P_{MB} \approx \Delta^2 \left| \sum_{n=1}^{N} J_{oz}(x_n) \right|^2 \qquad (5.5\text{-}9)$$

Dividing (5.5-6) and (5.5-7) by (5.5-9) produces the relative scattering sidelobe level.

$$\sigma_E = \frac{\pi N \sigma_{cur}^2}{2H_o \left| \sum_{n=1}^{N} J_{oz}(x_n) \right|^2} \qquad (5.5\text{-}10)$$

$$\sigma_H = \frac{\pi N \sigma_{cur}^2 \sin^2 \phi_o}{2H_o \left| \sum_{n=1}^{N} J_{oz}(x_n) \right|^2} \qquad (5.5\text{-}11)$$

5.6 Computer Results

This section presents computer plots depicting the no-error and error resistive tapers, surface current densities, and scattering patterns for various strips. In addition, the isolated error terms for the resistive taper, surface current density, and scattering patterns are shown.

Figure 5.1 delineates the E-polarization integral equation error and no-error results for a 4λ resistive strip with a 40dB $\bar{n}=12$ Taylor resistive taper and $\sigma_k = 0.3$. Figure 5.2 shows the PO results for the same strip with exactly the same resistivity errors. The integral equation error surface current density is much smoother than the PO error current. Notice the excellent agreement between the PO and integral equation scattering patterns, though. Figure 5.3 superimposes the PO and integral equation error terms. The surface current densities are plots from (5.3-3) and (5.3-6) and the scattering patterns are plots of the last three terms in (5.4-4).

Decreasing σ_k to 0.1 produces a marked decrease in the error perturbations as shown by the integral equation results in Figure 5.4.

Figures 5.5 to 5.7 show the results for a constant resistive strip with $\eta = 2.0$ and $\sigma_k=0.3$. Even though there are radical changes in the surface current density of the strip, the scattering patterns show little change. This happens because the original sidelobe level of the strip is much higher than the scattering pattern due to the error terms.

a. Magnitude of induced surface
   current density on strip, ϕ_o=90°

b. Normalized resistivity on strip

c. Bistatic scattering pattern, ϕ_o=90°

d. Backscattering pattern

Figure 5.1 — Error and no-error plots calculated from the E-polarized integral equation when the strip is 4λ wide, has a 40dB $\bar{n}$=12 Taylor resistive taper, and has random errors with σ_k=0.3

a. Magnitude of induced surface
current density on strip, $\phi_o=90°$

b. Normalized resistivity on strip
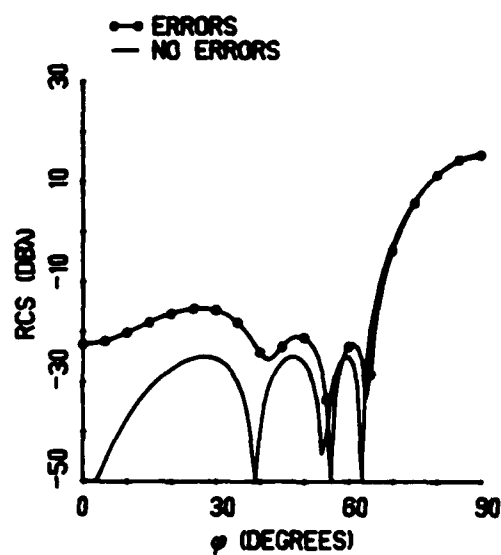
c. Bistatic scattering pattern, $\varphi_o=90°$
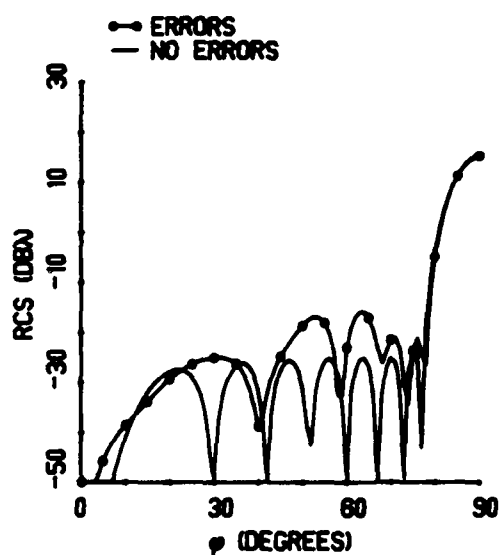
d. Backscattering pattern

Figure 5.2 — Error and no-error plots calculated using the E-polarized PO equation when the strip is 4λ wide, has a 40dB $\bar{n}=12$ Taylor resistive taper, and has random errors with

$$\sigma_k=0.3$$

a. Magnitude of surface current, ϕ_o=90° due to errors in the resistivity

b. Errors in normalized resistivity

c. Bistatic scattering pattern, φ_o=90° due to errors in the surface current

d. Backscattering pattern due to errors in the surface current
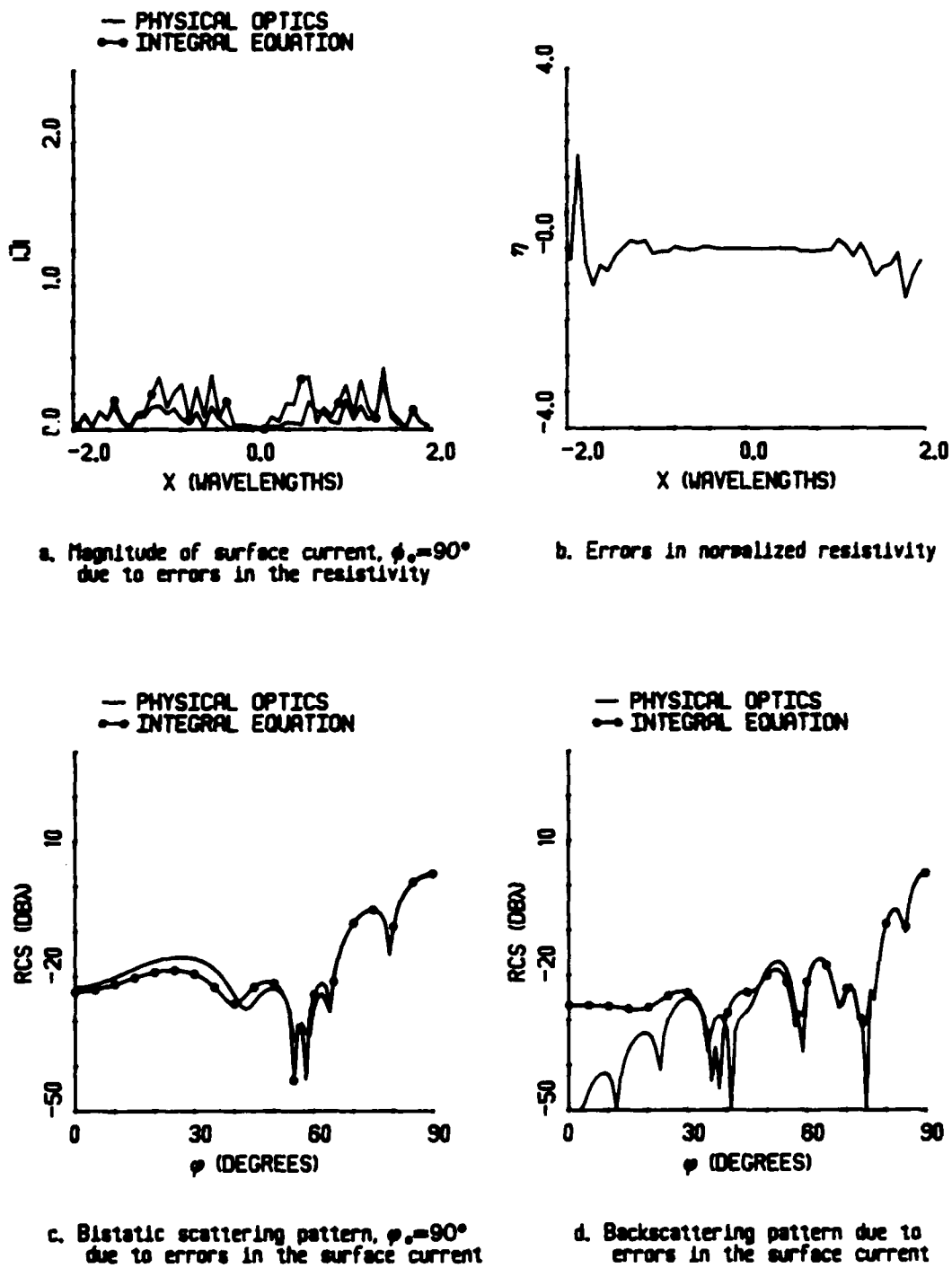
Figure 5.3 — Isolated E-polarized error contributions when the 4λ wide strip has a 40dB $\bar{n}$=12 Taylor resistive taper and random errors with σ_k=0.3

a. Magnitude of induced surface current density on strip, $\phi_o = 90°$

b. Normalized resistivity on strip

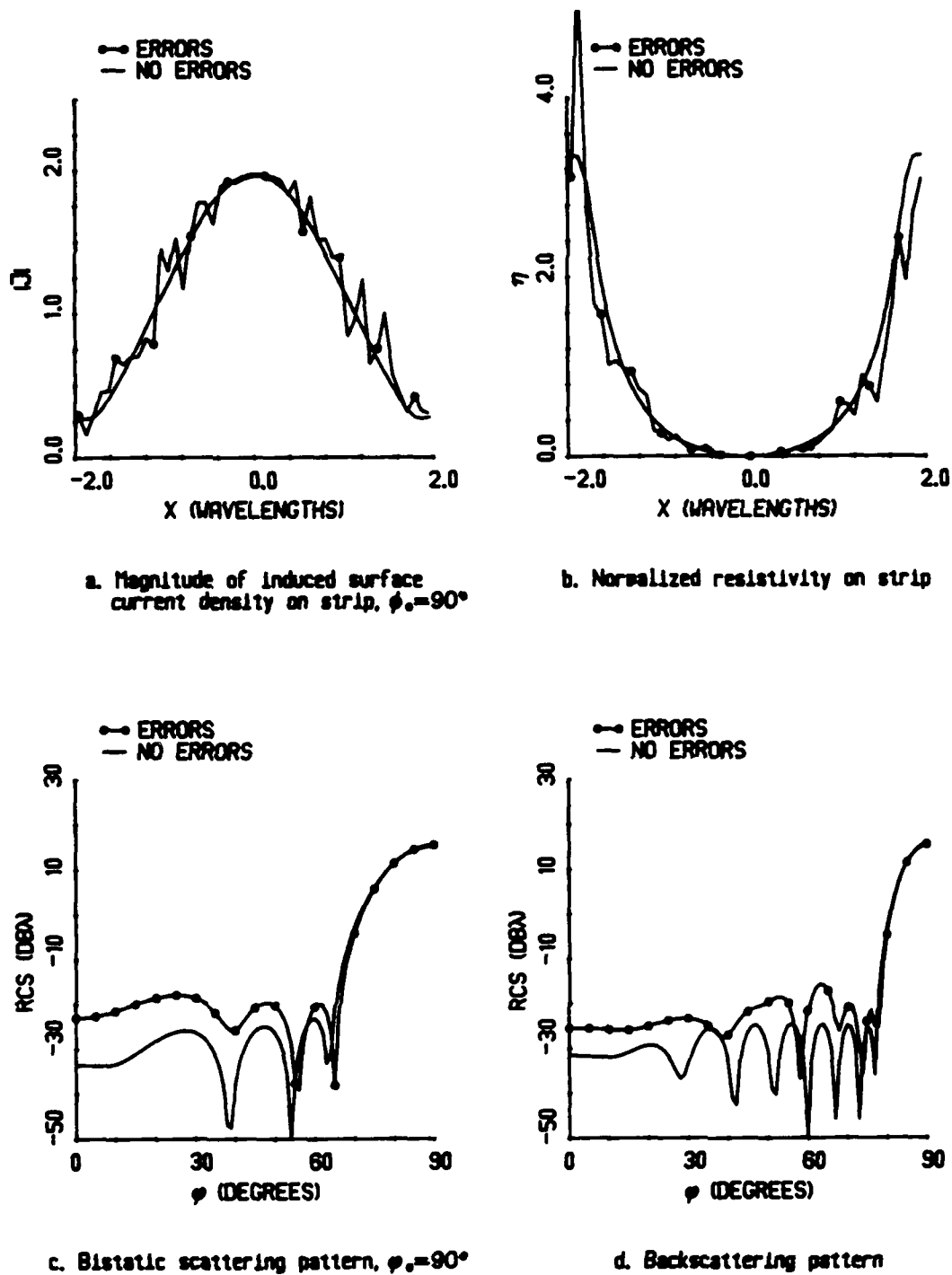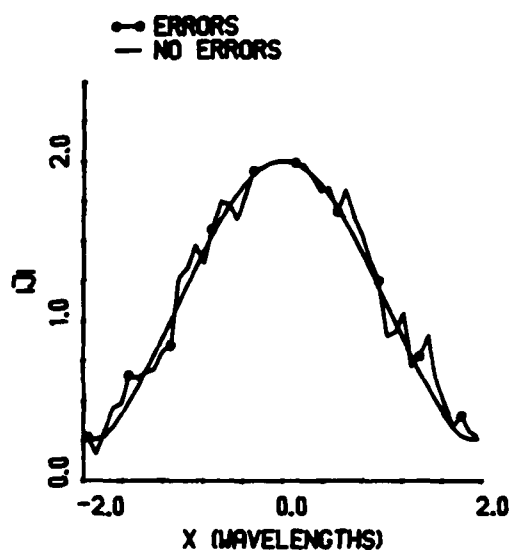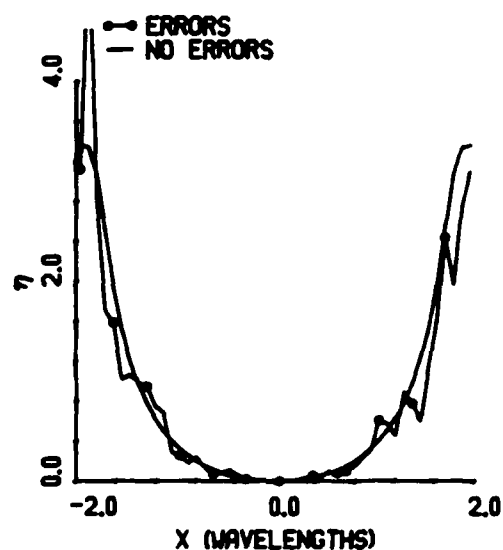c. Bistatic scattering pattern, $\varphi_o = 90°$

d. Backscattering pattern

Figure 5.4 — Error and no-error plots calculated from the E-polarized integral equation when the 4λ wide strip, has a 40dB $\bar{n}=12$ Taylor resistive taper and random errors with $\sigma_k = 0.1$

a. Magnitude of induced surface
current density on strip. ϕ_o=90°

b. Normalized resistivity on strip

c. Bistatic scattering pattern. ϕ_o=90°

d. Backscattering pattern

Figure 5.5 — Error and no-error plots calculated from the E-polarized integral equation
when the 4λ wide strip has a constant resistive taper ($\eta = 2.0$) and random errors with

$$\sigma_k=0.3$$

a. Magnitude of induced surface current density on strip. $\phi_o=90°$

b. Normalized resistivity on strip
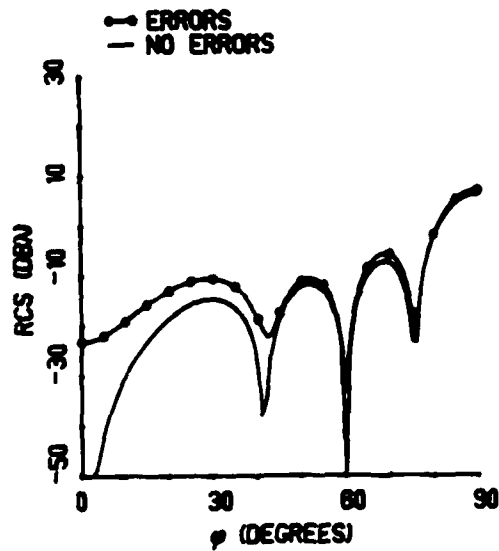
c. Bistatic scattering pattern. $\phi_o=90°$
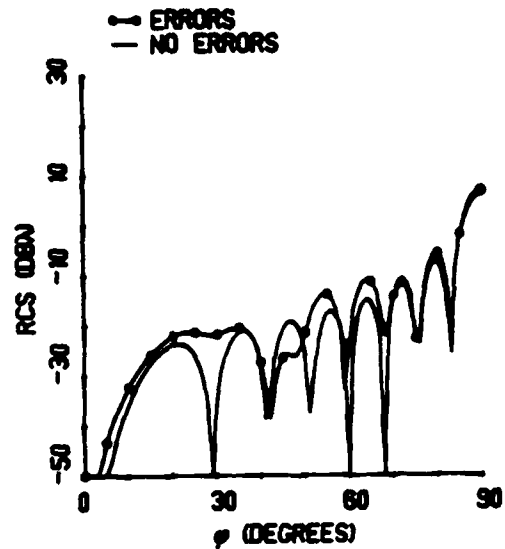
d. Backscattering pattern

Figure 5.6 — Error and no-error plots calculated using the E-polarized PO equation when the 4λ wide strip has a constant resistive taper ($\eta = 2.0$) and random errors with $\sigma_k=0.3$

a. Magnitude of surface current, $\phi_o=90°$ due to errors in the resistivity

b. Errors in normalized resistivity

c. Bistatic scattering pattern, $\varphi_o=90°$ due to errors in the surface current

d. Backscattering pattern due to errors in the surface current
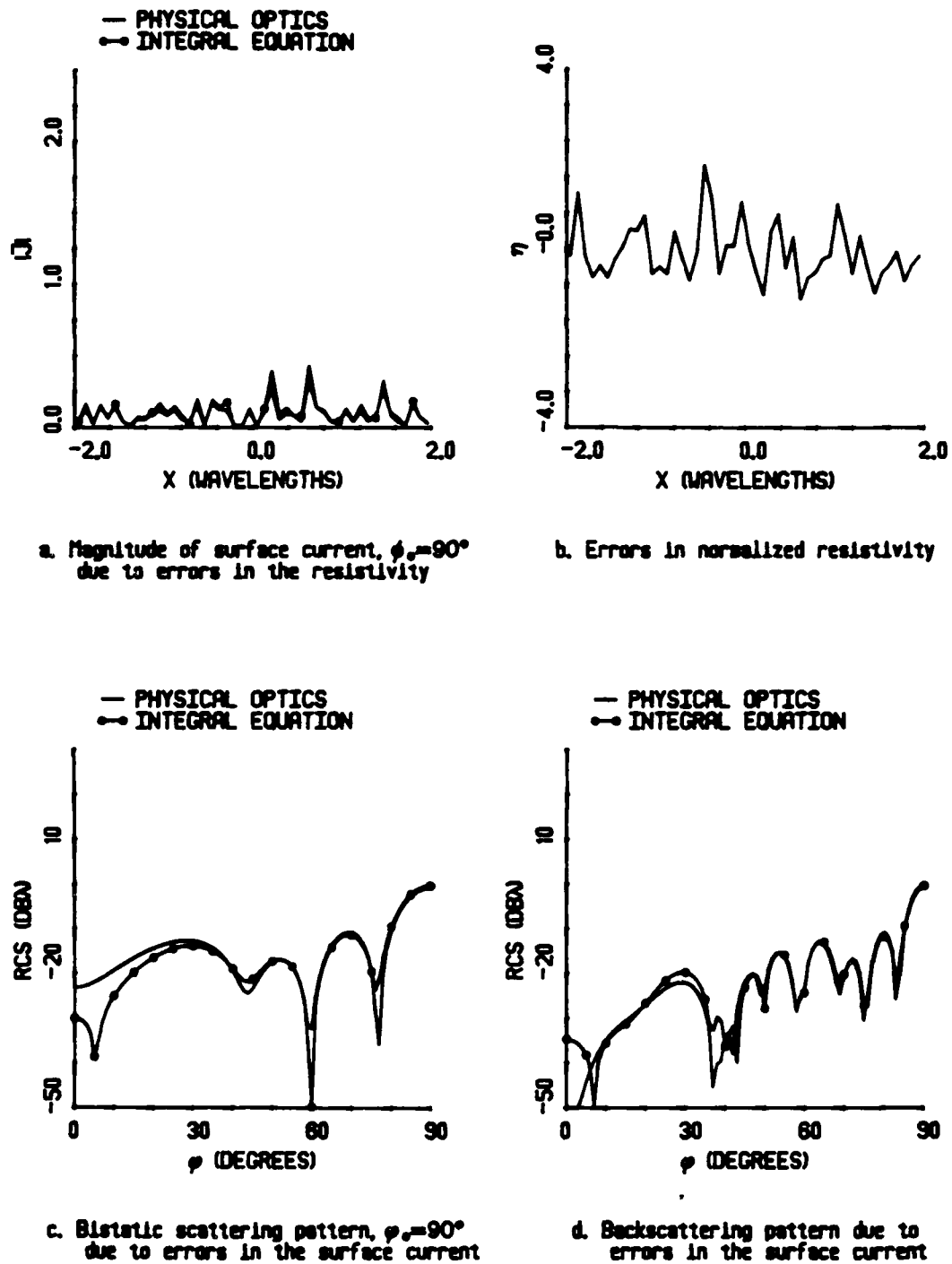
Figure 5.7 — Isolated error contributions when the 4λ wide strip has a constant resistive taper ($\eta = 2.0$) and random errors with $\sigma_k=0.3$

a. Magnitude of induced surface current density on strip, $\phi_o = 90°$

b. Normalized resistivity on strip

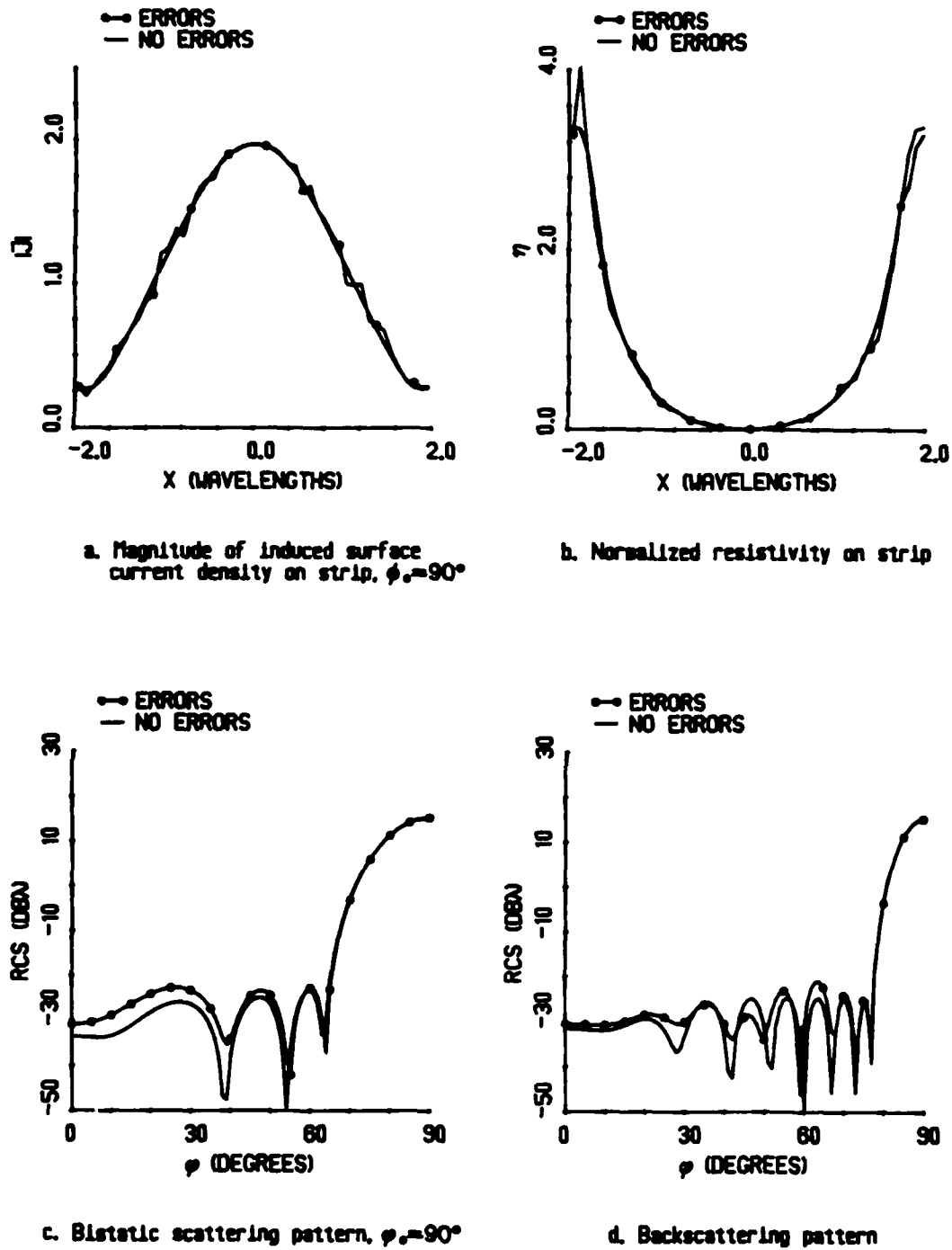c. Bistatic scattering pattern, $\varphi_o = 90°$
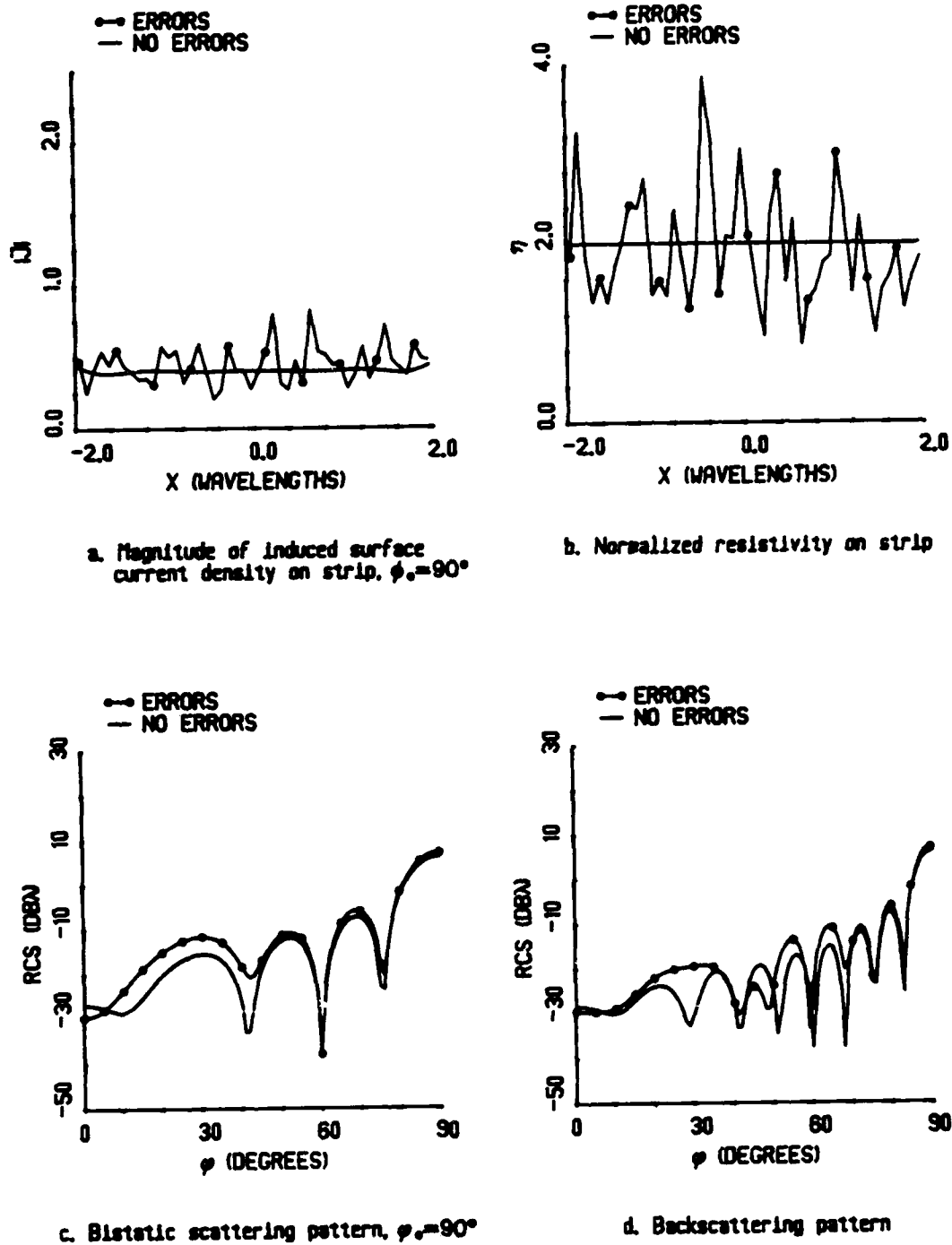
d. Backscattering pattern
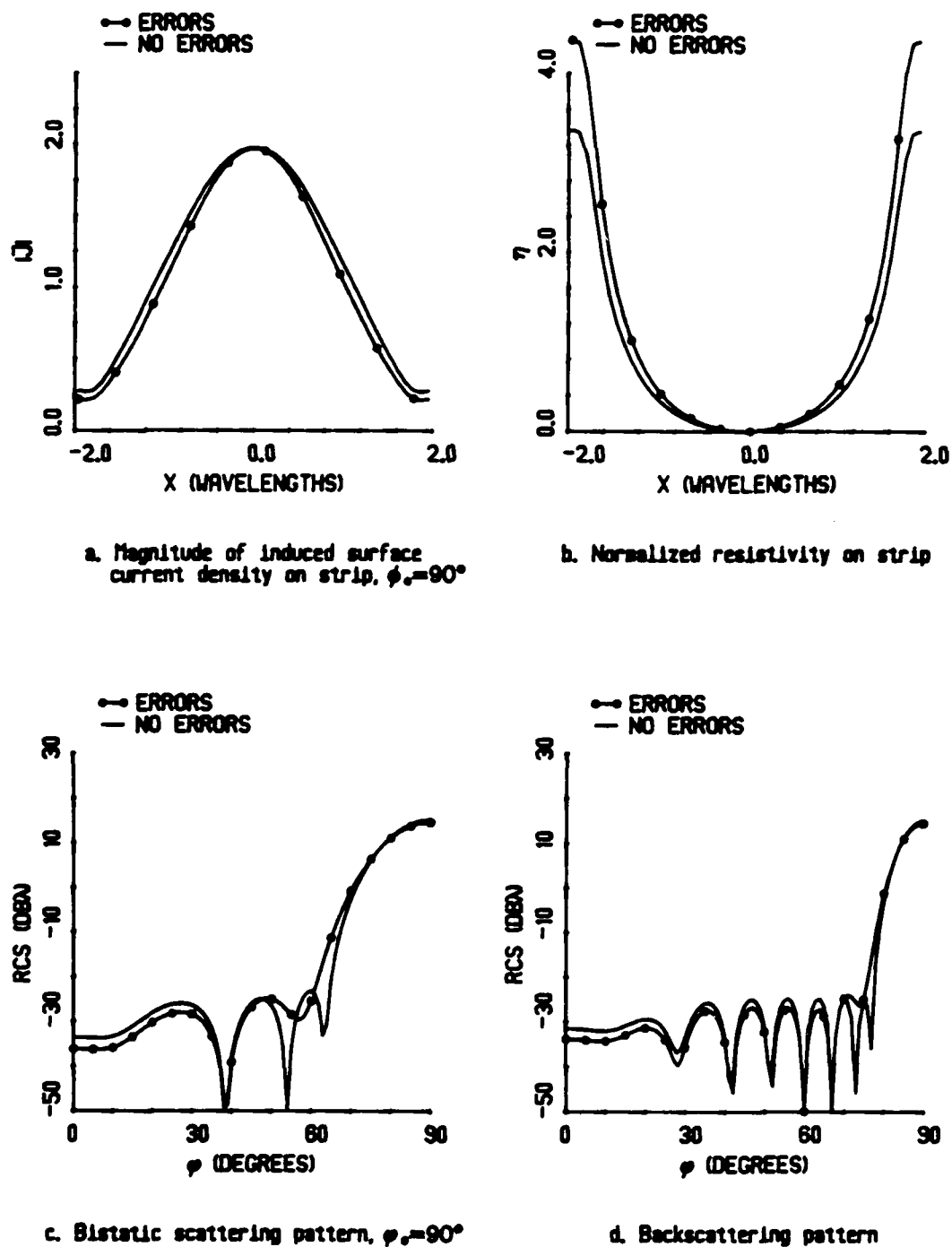
Figure 5.8 — Error and no-error plots calculated from the E-polarized integral equation when the 4λ strip has a 40dB $\bar{n}=12$ Taylor resistive taper and correlated errors with

$$e_c(x) = .2\eta_o(x)$$
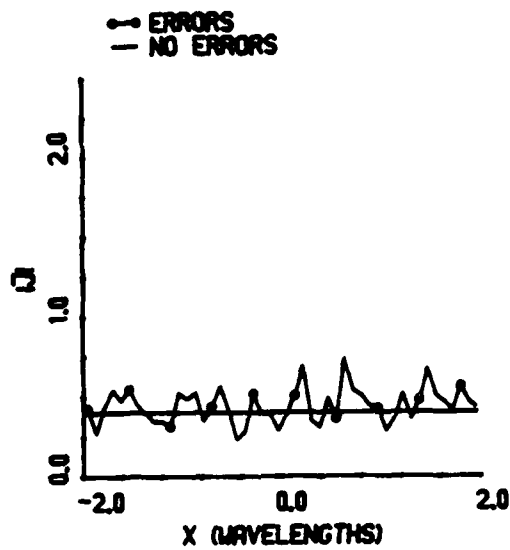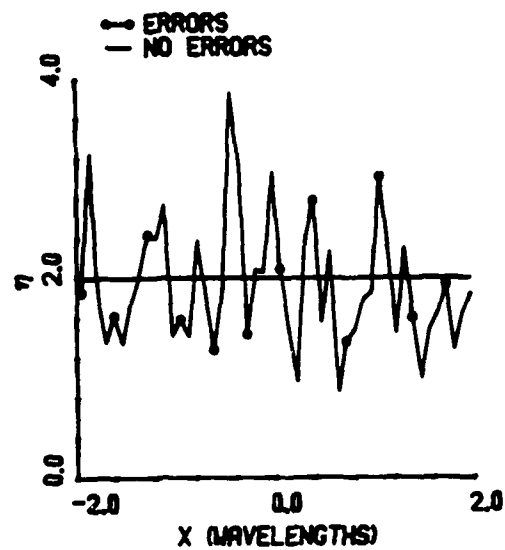
a. Magnitude of induced surface
current density on strip, $\phi_o=90°$

b. Normalized resistivity on strip

c. Bistatic scattering pattern, $\varphi_o=90°$

d. Backscattering pattern

Figure 5.9 — E-polarised integral equation error and no-error plots when the 4λ strip has a 40dB $\bar{n}=12$ Taylor resistive taper and correlated errors with $e_c(x) = .1\cos\left[2\pi\left(\frac{4x}{2}\right)\right]\eta_o(x)$

ERRORS ●━●
NO ERRORS ━

ERRORS ●━●
NO ERRORS ━

X (WAVELENGTHS)

X (WAVELENGTHS)

a. Magnitude of induced surface current density on strip, ϕ_o=90°

b. Normalized resistivity on strip

ERRORS ●━●
NO ERRORS ━

ERRORS ●━●
NO ERRORS ━

RCS (DBλ)

RCS (DBλ)

φ (DEGREES)

φ (DEGREES)

c. Bistatic scattering pattern, φ_o=90°

d. Backscattering pattern

Figure 5.10 — E-polarized PO error and no-error plots when the 4λ strip has a 40dB $\bar{n}$=12 Taylor resistive taper and correlated errors with $e_c(x) = .1\cos\left[2\pi\left(\frac{4x}{2}\right)\right]\eta_o(x)$

a. Magnitude of surface current, $\phi_e{=}90°$
   due to errors in the resistivity

b. Errors in normalized resistivity

c. Bistatic scattering pattern, $\varphi_e{=}90°$
   due to errors in the surface current

d. Backscattering pattern due to
   errors in the surface current
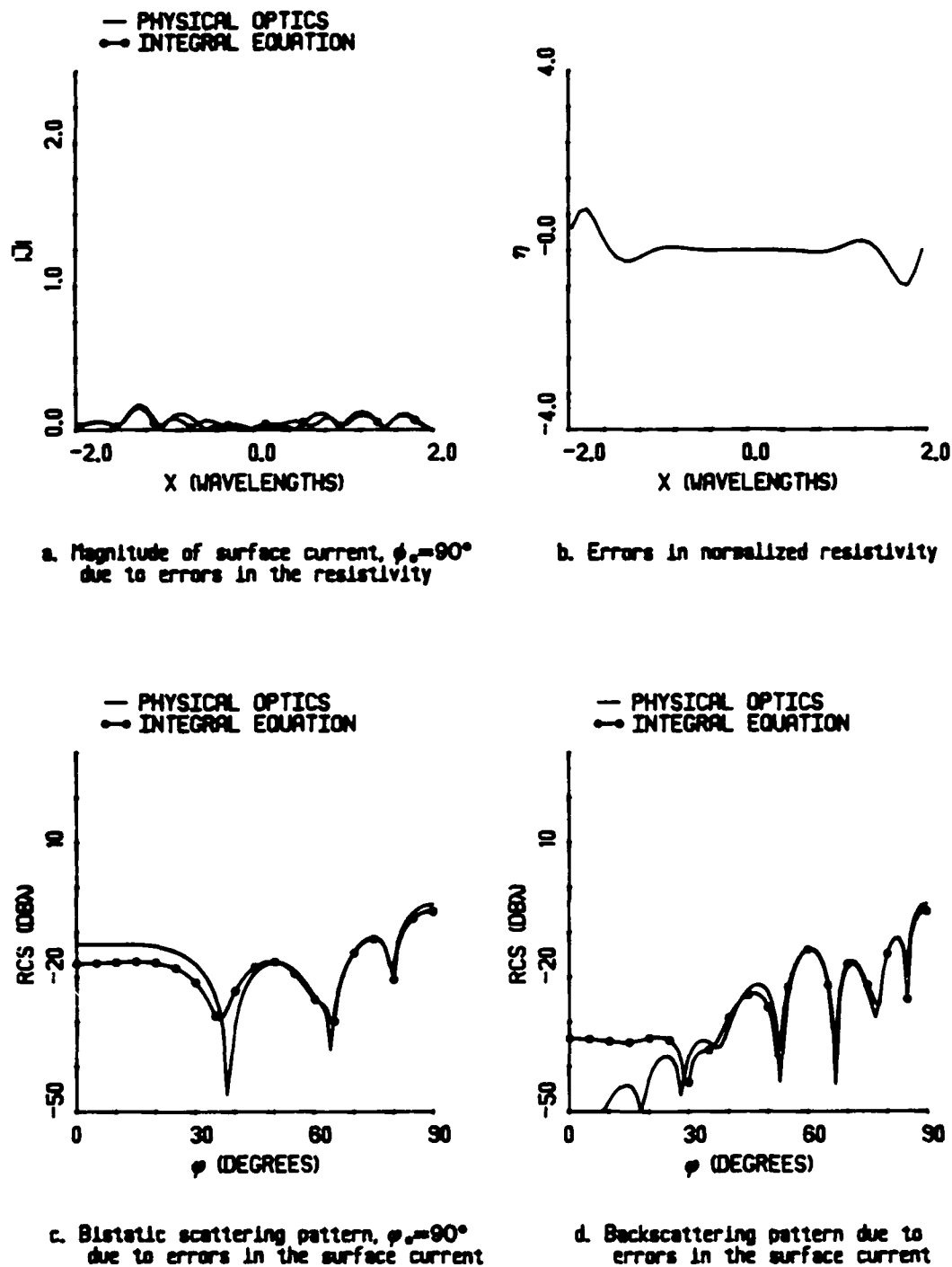
Figure 5.11 — Isolated error contributions when the 4λ strip has a 40dB $\bar{n}{=}12$ Taylor

resistive taper and correlated errors with $e_c(x) = .1\cos\left[2\pi\left(\frac{4x}{2}\right)\right]\eta_o(x)$

a. Magnitude of induced surface
current density on strip, $\phi_o = 90°$

b. Normalized resistivity on strip

c. Bistatic scattering pattern, $\varphi_o = 90°$

d. Backscattering pattern
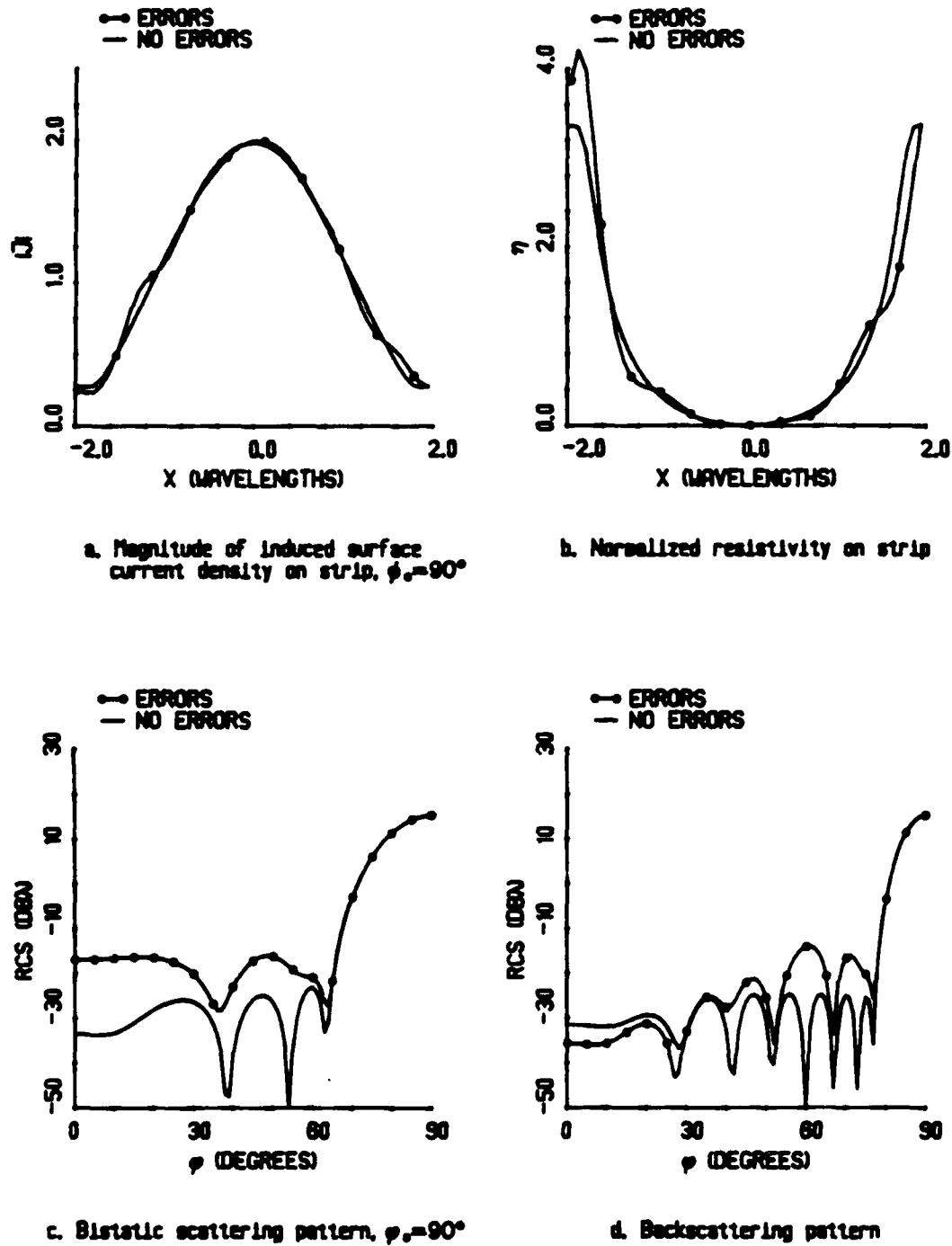
Figure 5.12 — E-polarized integral equation plots when the 4λ strip has a 40dB $\bar{n}=12$
Taylor taper and $e_c(x) = .1\cos\left[2\pi\left(\frac{4x}{2}\right)\right]\eta_o(x)$ correlated and $\sigma_k = .3$ random errors
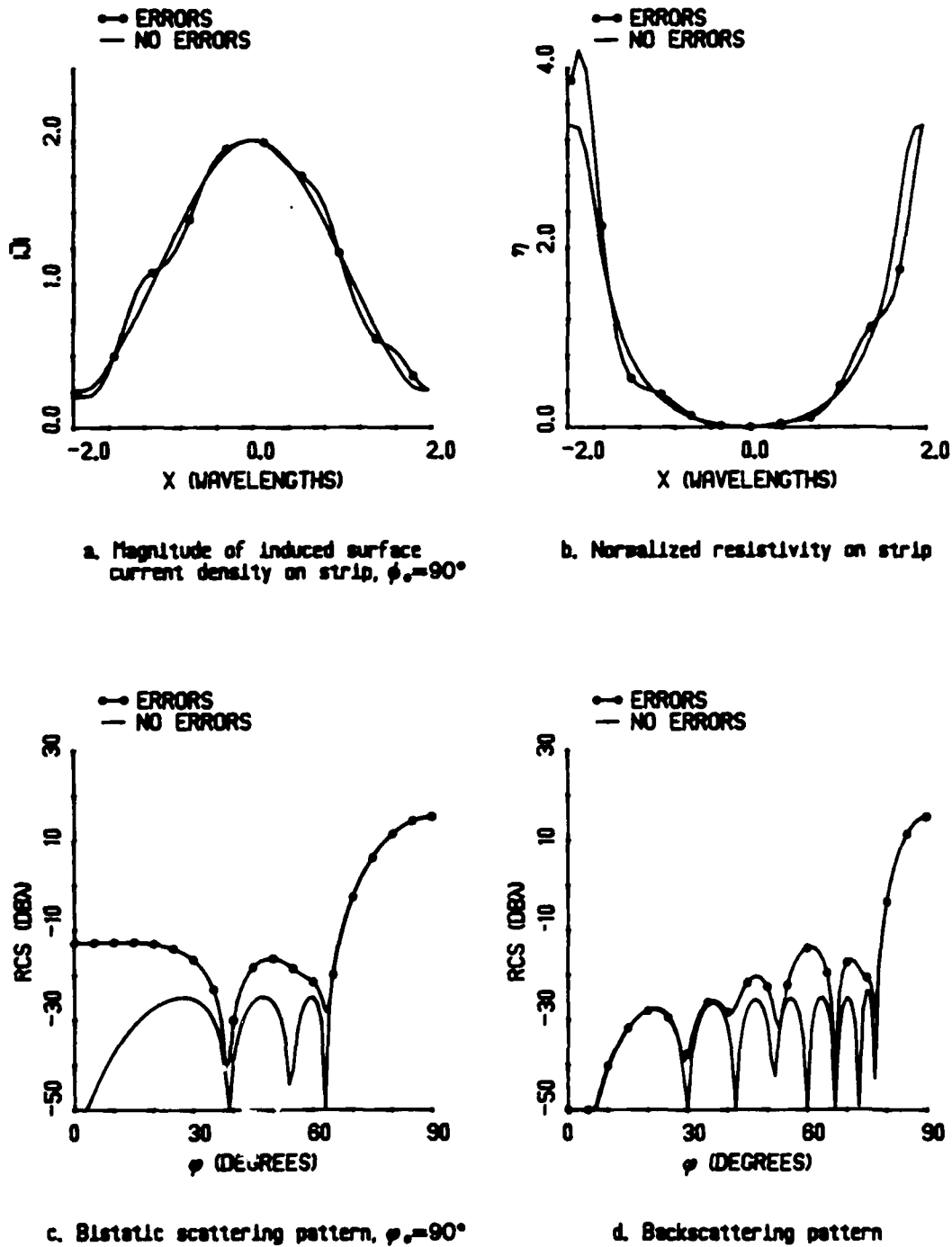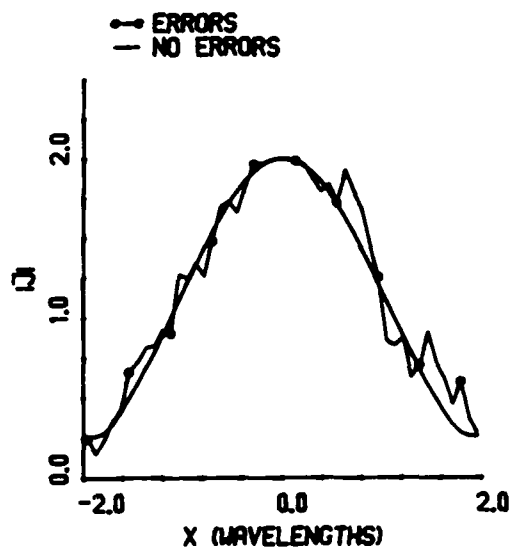
a. Magnitude of induced surface
current density on strip, ϕ_o=90°
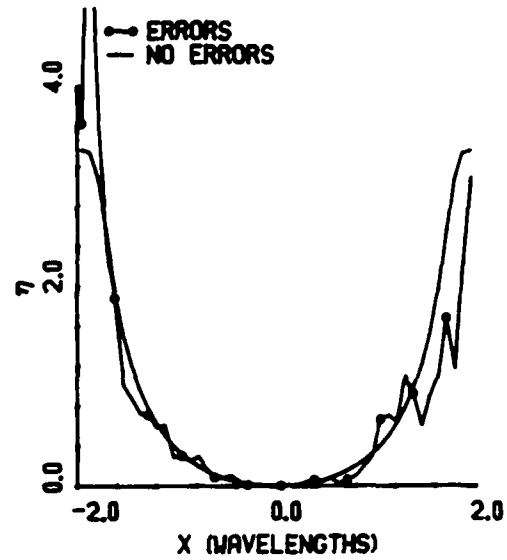
b. Normalized resistivity on strip

c. Bistatic scattering pattern, φ_o=90°

d. Backscattering pattern

Figure 5.13 — E-polarized PO equation plots when the 4λ strip has a 40dB $\bar{n}$=12 Taylor taper and $e_c(x) = .1\cos\left[2\pi\left(\frac{4x}{2}\right)\right]\eta_o(x)$ correlated and σ_k =.3 random errors

— PHYSICAL OPTICS
•—• INTEGRAL EQUATION

a. Magnitude of surface current, ϕ_o=90°
   due to errors in the resistivity

b. Errors in normalized resistivity

— PHYSICAL OPTICS
•—• INTEGRAL EQUATION

— PHYSICAL OPTICS
•—• INTEGRAL EQUATION

c. Bistatic scattering pattern, φ_o=90°
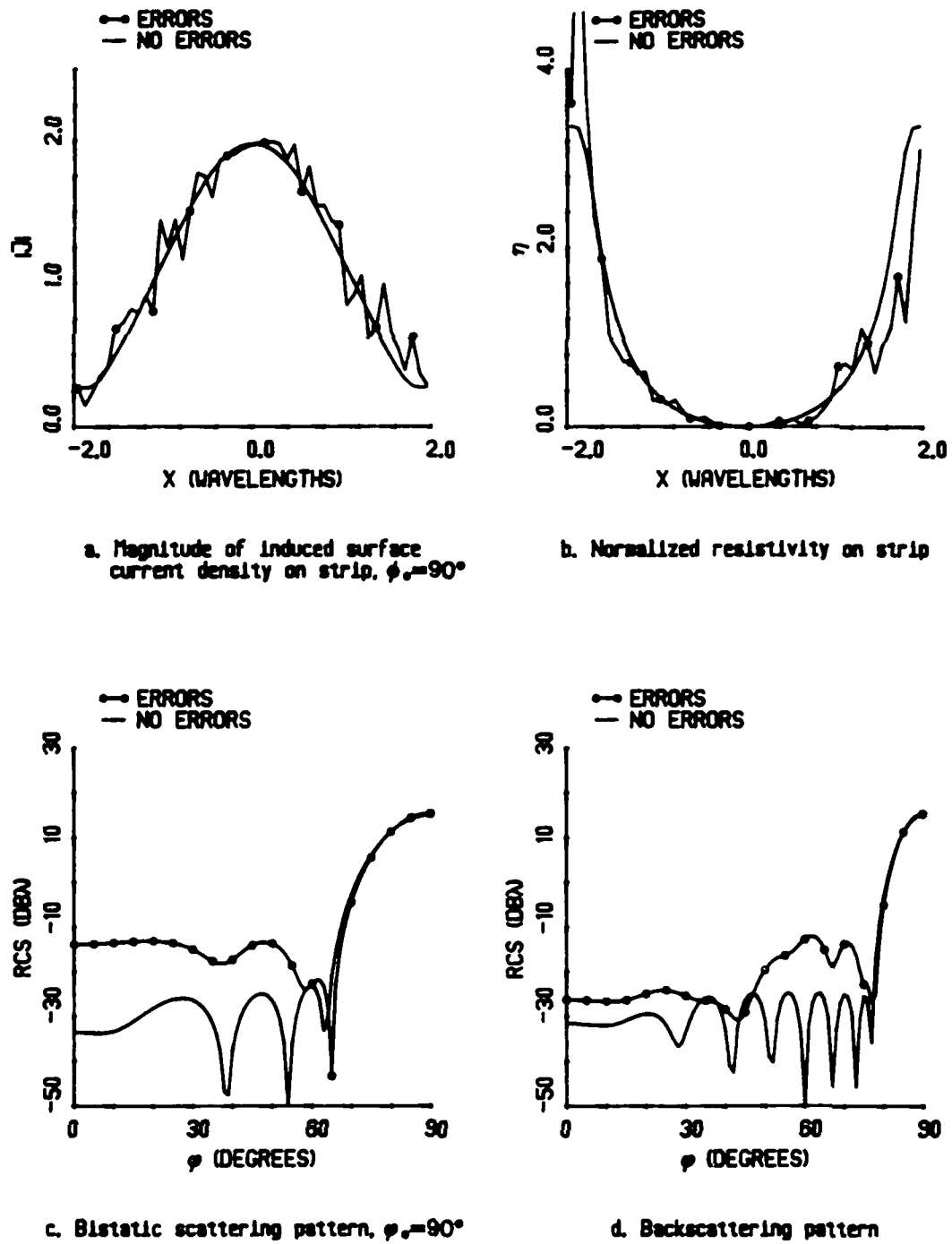   due to errors in the surface current

d. Backscattering pattern due to
   errors in the surface current

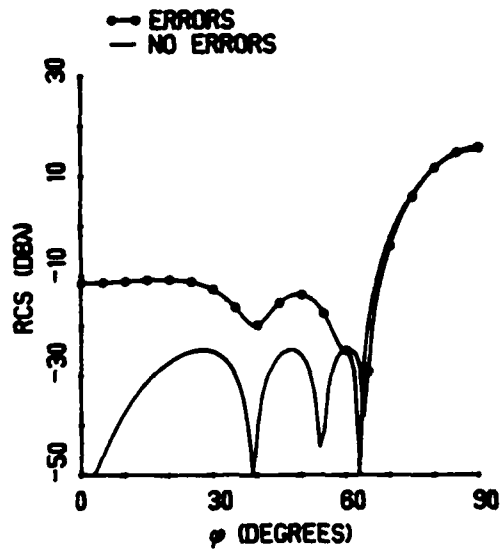Figure 5.14 — Isolated error contributions when the 4λ strip has a 40dB $\bar{n}$=12 Taylor

taper and $\epsilon_c(x) = .1\cos\left[2\pi\left(\frac{4x}{2}\right)\right]\eta_o(x)$ correlated and σ_k =.3 random errors
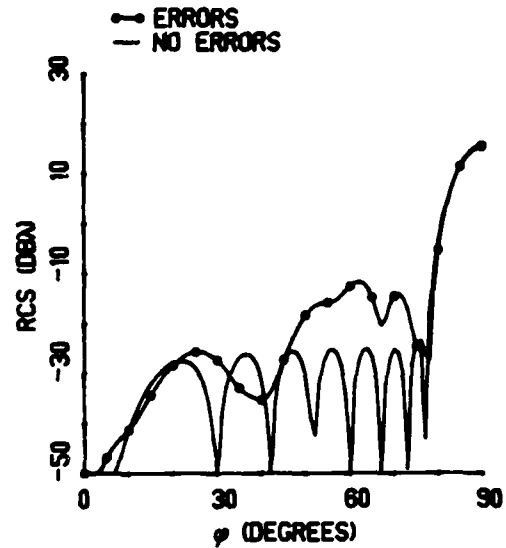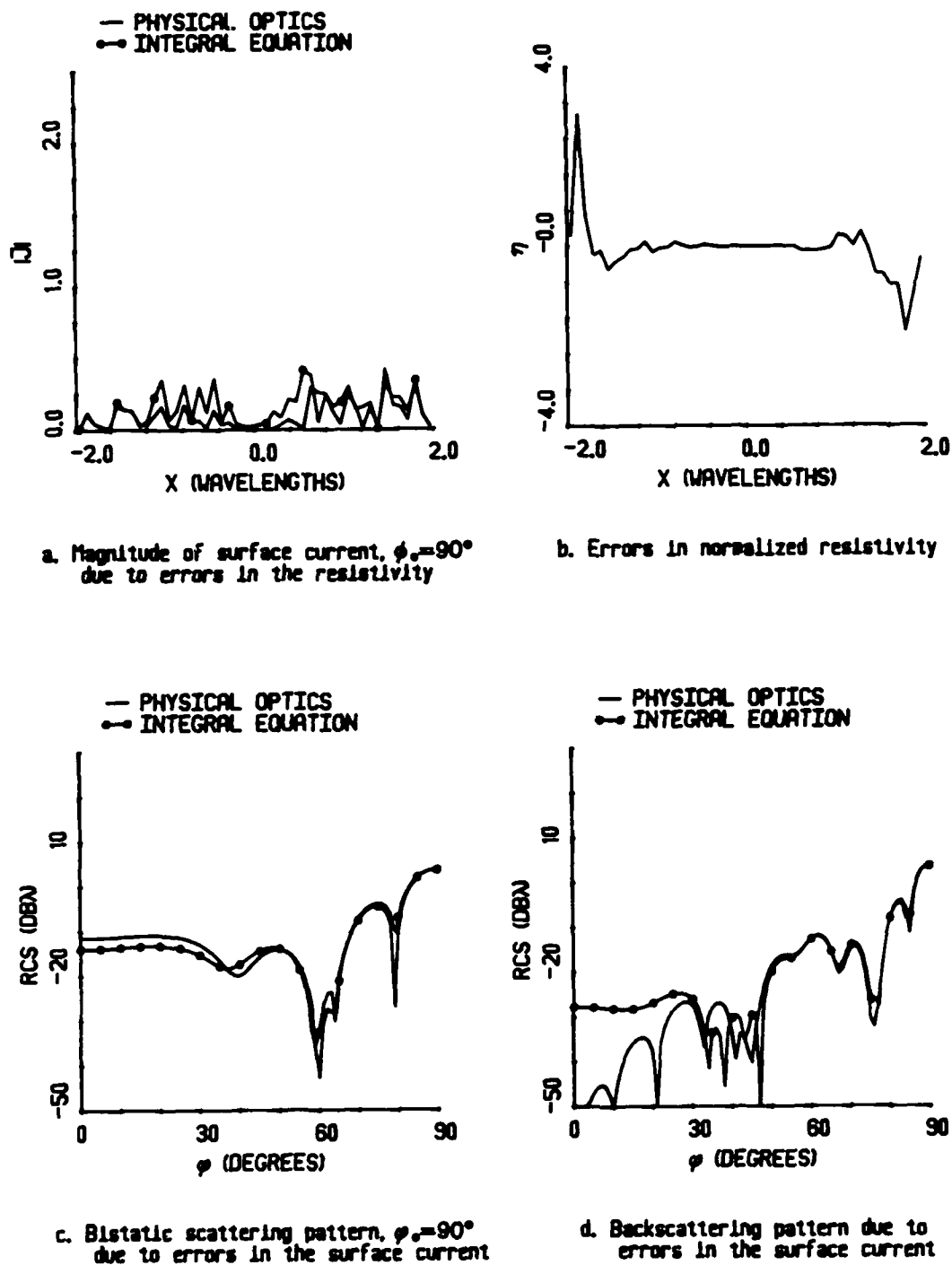
Figure 5.8 shows the first example of a correlated error using the E-polarized integral equation. The strip is 4λ wide with a 40dB $\bar{n}=12$ Taylor resistive taper and a correlated error given by (5.2-2) with c=0.2 and q=0. This error produces an even steeper resistive taper that reduces the sidelobes to a lower level than the no-error taper.

Another example of a correlated error appears in Figures 5.9 to 5.11. The strip is 4λ wide with a 40dB $\bar{n}=12$ Taylor resistive taper and a correlated error given by (5.2-3) with c=.1 and q=4. Figure 5.9 shows the integral equation error and no-error results, while Figure 5.10 shows the same results for PO. The PO and integral equation error terms appear alone in Figure 5.11.

Section 5.1 mentions that in array theory random errors primarily alter the sidelobe level away from the main beam and correlated errors primarily alter the sidelobe level near the main beam. The same phenomena appears in the figures presented here. For instance, the random errors in Figures 5.1 and 5.2 raise the sidelobe level uniformly everywhere, but the correlated errors in Figure 5.9 and 5.10 raise the sidelobe level near the main beam. When these errors are combined, the error scattering patterns closely resemble the correlated error patterns near the main beam, while they closely resemble the random error patterns far from the main beam. Figure 5.12 shows the E-polarization integral equation and Figure 5.13 shows the PO results for the combined errors. Figure 5.14 shows error plots of the combined random and correlated errors.

CHAPTER VI

EXPERIMENTAL MEASUREMENT OF THE BISTATIC SCATTERING PATTERNS OF RESISTIVE SHEETS

The theory presented in the previous chapters is more convincing when demonstrated experimentally. Such an experiment has three main parts: building the strip, measuring the resistive taper, and measuring the far field scattering patterns. Each of these parts has difficulties to over-come. For instance, accurately building a low sidelobe resistive taper requires facilities that are not available, and even if the facilities for building the strip were available, accurately measuring the resistive taper has limitations as discussed in Chapter 4. Finally, bistatic scattering measurement facilities are not available at the University of Michigan.

The first part of this chapter tells how the perfectly conducting and resistive sheets were constructed for the experiment. Next, the experimental set-up is described and the potential errors in the experiment discussed. Finally, the experimental and theoretical results are compared and discussed.

6.1 Construction of the Strips

There were three alternatives to constructing a tapered resistive strip: 1) build it in-house, 2) pay a contractor to build it, and 3) ask a contractor to donate a tapered resistive sheet. The first alternative was very unattractive because the Radiation Laboratory does not have the facilities to accurately build a tapered resistive strip. Had this alternative been pursued, the strip would have been built by spraying resistive paint on a substrate that had a dielectric constant close to that of free space. Such an archaic technique would

131

probably have proven frustrating and inaccurate. The second alternative was unattractive because of the cost. Unfortunately, a graduate student's budget could not quite match the $50,000+ price tag for buying a tapered resistive strip built to specifications. The final alternative proved most attractive. Southwall Technologies, Inc. provided a strip that has an $\frac{1}{3}x^4 + 2x^2 + 5$ (x in inches) taper with one edge at a resistivity approximately equal to 0 and the other a resistivity of $\eta > 4.0$. Although this taper is not symmetric about the center of the strip and does not correspond to any of the synthesized Taylor tapers in Chapter 3, it actually worked quite well for the purposes of this thesis after a few minor adjustments.

Three samples were prepared for the bistatic measurements:

1) perfectly conducting

2) substrate

3) tapered resistive

Each is 16 inches square or about 4λ square at a frequency of 3 GHz.

6.1.1 Perfectly Conducting Sheet

The perfectly conducting strip was cut from a 0.032 inch thick aluminum sheet. Aluminum has a dc conductivity of $\sigma = 3.54 \times 10^7$ mhos/m which corresponds to a very low value of resistivity. It can safely be assumed that $\eta = 0.0$ on this sheet. This target serves as a comparison to the tapered sheet and as a calibration target.

6.1.2 Substrate Sheet

A 16×16 inch uniform substrate sheet was made of kaptan. The sheet had to be pieced together in four parts, because the available pieces of substrate were too small to cut a single 16×16 inch sheet. Two of the pieces are $13\frac{1}{2} \times 8$ inches and the other two are $2\frac{1}{2} \times 8$ inches. They were butted together and joined by Scotch tape to form the 16×16 inch sheet.

The dielectric constant of Kaptan is approximately real and the substrate thickness is 0.007 inches. The corresponding high value of η results in a very low RCS. The styrofoam support and Scotch tape have a very low RCS relative to the metal plate and do not have any noticeable impact on the measurements. The styrofoam and tape can have an effect on the substrate sheet measurements, though. The effects of the styrofoam support may

be virtually eliminated by measuring the bistatic pattern of the support and background and subtracting this measurement from the bistatic pattern of the target, support, and background. Since the tape has a relatively low dielectric constant and has a much smaller area than the substrate sheet, it is assumed to have little effect on the main beam of the scattered field.

6.1.3 Tapered Resistive Sheet

Southwall Techologies sent the tapered sheet in a roll about 6 feet long and 14 inches wide. The taper was not symmetric about the center. Instead, the taper starts at perfectly conducting at one edge and gradually increases to a very high resistivity at the other end. The taper is given by the equation

$$R = \frac{1}{3}x^4 + 2x^2 + 5 \tag{6.1-1}$$

where x is in inches and R in Ω. Figure 6.1 shows a graph of this taper with $x=0\lambda$ at the center of the sheet and extending 2λ on either side of the center. The sheet was constructed by sputter depositing indium tin oxide on one side of the kaptan substrate.

This thesis is concerned with symmetrical resistive tapers of strips. To get this symmetry, two 16 inch long pieces were cut from the 6 foot roll. Each piece was 14 inches wide, so it had to be trimmed to 8 inches wide. A thin clear line marked the $x=1\lambda$ position on the strip. Both strips were trimmed to 4 inches on either side of the center line. These two pieces were layed flat with the perfectly conducting sides touching. The back (kaptan side) of the pieces were joined with Scotch tape while the front (metal deposited side) of the pieces were joined with $\frac{1}{4}$ inch copper tape. The resultant sheet was 16 inches square with a symmetrical resistive taper. A photograph of the tapered sheet appears in Figure 6.2. In the picture, the taper runs horizontally while the copper tape runs vertically.

6.1.4 Mounting the Sheets

A 16 inch square of styrofoam was cut from a larger $1\frac{1}{2}$ inch thick piece of styrofoam using a "hot" wire. Three sides were beveled and sanded to reduce the specular scattering. A small $6 \times 2 \times 1\frac{1}{2}$ piece of styrofoam served as a support for the larger square piece.

The sheets were mounted on the styrofoam using double sided Scotch tape. This tape had little effect on the scattering patterns of the tapered sheet and perfectly conducting
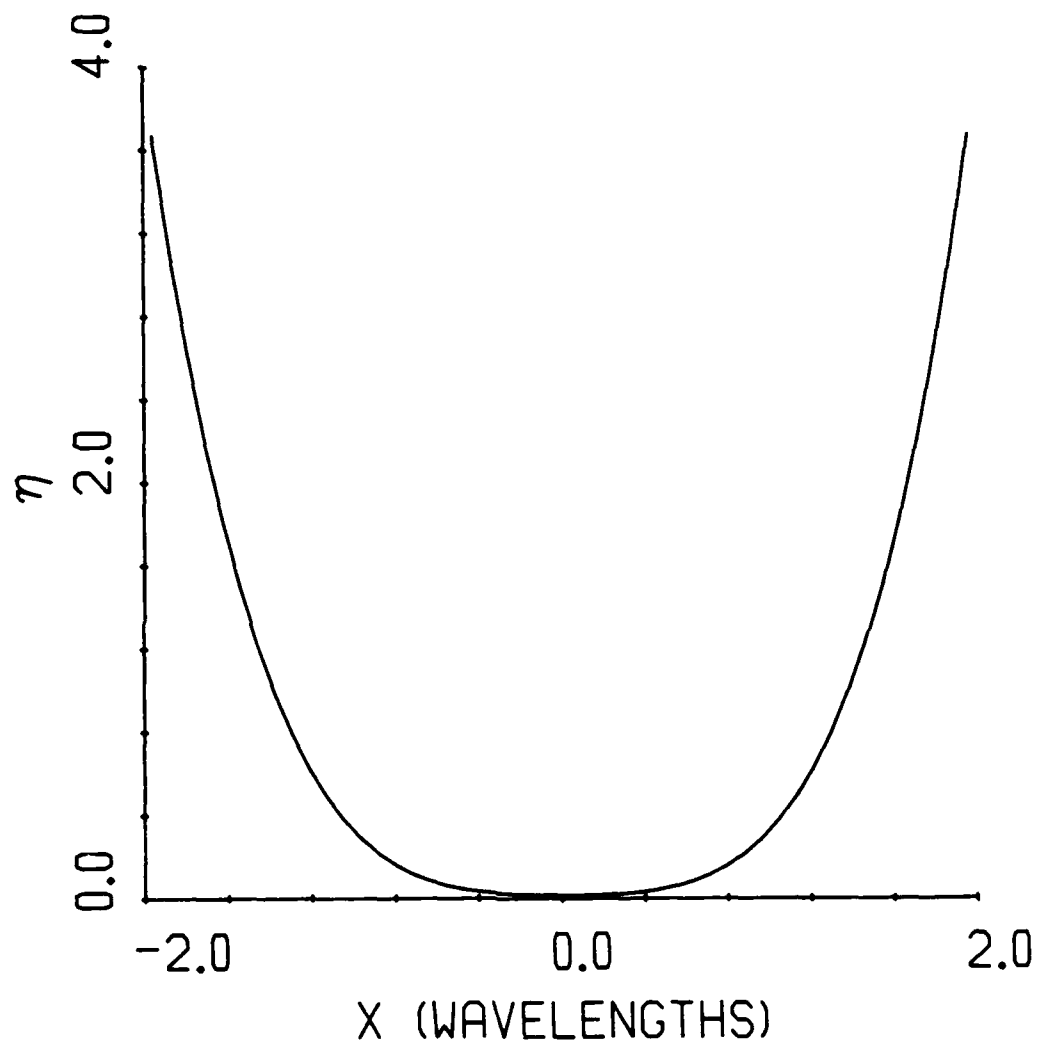
Figure 6.1 — Graph of the resistive taper of the $4\lambda \times 4\lambda$ sheet in the x-direction.
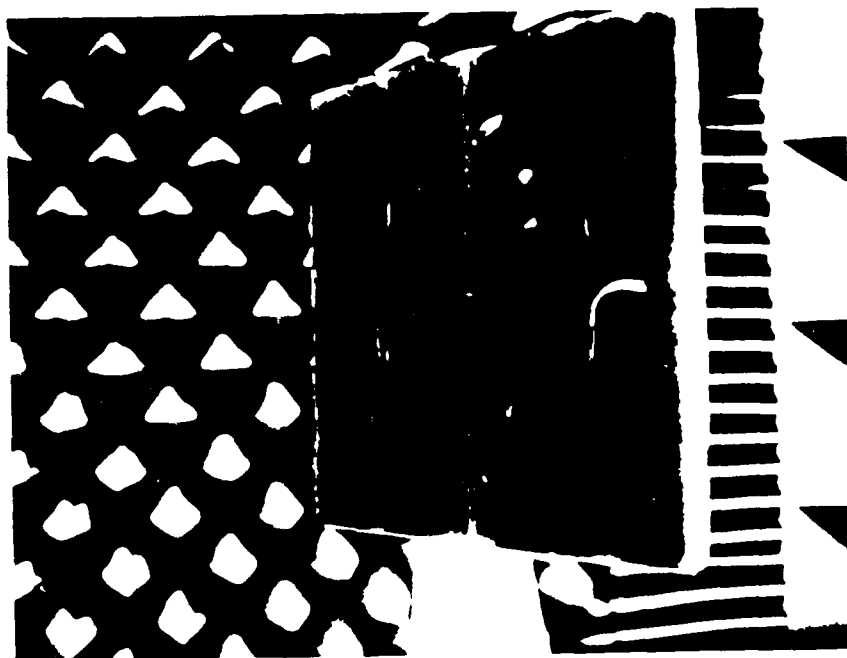
Figure 6.2 -- Photograph of the experimental tapered sheet after it had been cut and taped together to form a 16 inch square. Note that the sheet is most conductive at the center.

sheet, and an unknown effect on the substrate sheet. The aluminum sheet proved to be very heavy and the double sided tape could not firmly hold it against the styrofoam support. In order to firmly attach the metal sheet to the support. the corners of the sheet were securely taped to the styrofoam.

Since the resistive sheets and styrofoam support were light-weight and the mount turned very smoothly, a small piece of masking tape behind the styrofoam support was sufficient to hold it to the styrofoam mount in the chamber. On the other hand, the metal sheet was very heavy and required a lot of masking tape to firmly hold the sheet and styrofoam support to the mount. The tape has a very low scattering return relative to the metal sheet and is also subtracted from the measurements with the background. Consequently, the extra tape should not have interfered with accurate bistatic measurements.

6.2 Bistatic Scattering Measurements of the Sheets

The experiments were performed at the Rome Air Development Center (RADC) measurement facility at Ipswich, MA. This facility has a bistatic measurement range suited for the purposes of this thesis.

The range consists of a large rectangular aneochoic chamber with a 6 inch diameter styrofoam cylinder mount close to one side of the chamber (see diagram in Figure 6.3). This mount holds the sheet and styrofoam support (photograph in Figure 6.4). A boom rotates about the center of the mount. Both the mount at one end of the boom and the transmitting antenna at the other end move with the boom (see picture in Figure 6.5). In this way, the incident angle of the transmitted energy is always the same. The transmitting antenna is a 2 foot parabolic dish and is 105 inches away from the target. A stationary receiving horn is located in one of the walls of the chamber. As the boom rotates the transmitting antenna and the target, the receiving horn detects the scattered energy from the target. The scattered signal passes from the horn to a receiver, computer, and recording apparatus (picture of instrumentation in Figure 6.6). An absorber covered window in the same wall as the receiving horn allows access to the interior of the chamber to align the target and bistatic angle with a theodolite.

6.2.1 Alignment

theodolite

transmitting dish

rotating boom

105°

receiving horn

target on mount

equipment

aenochoic chamber

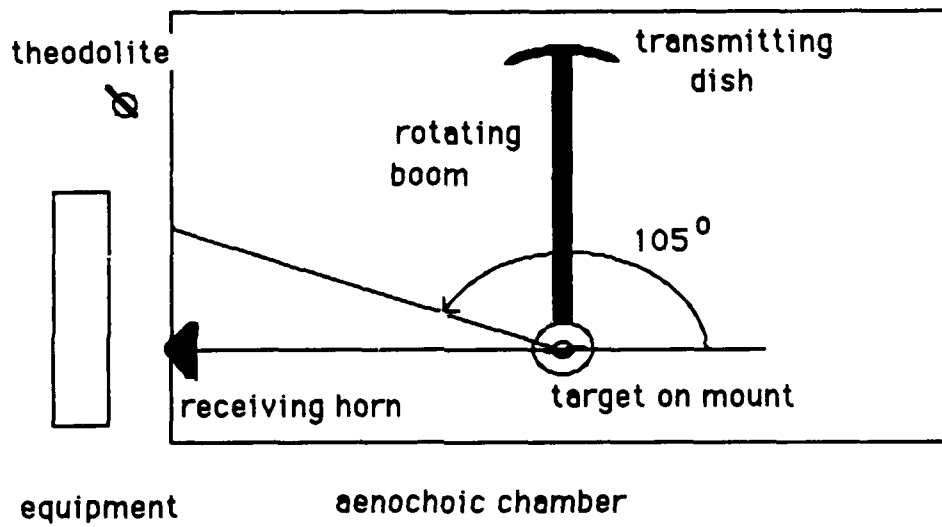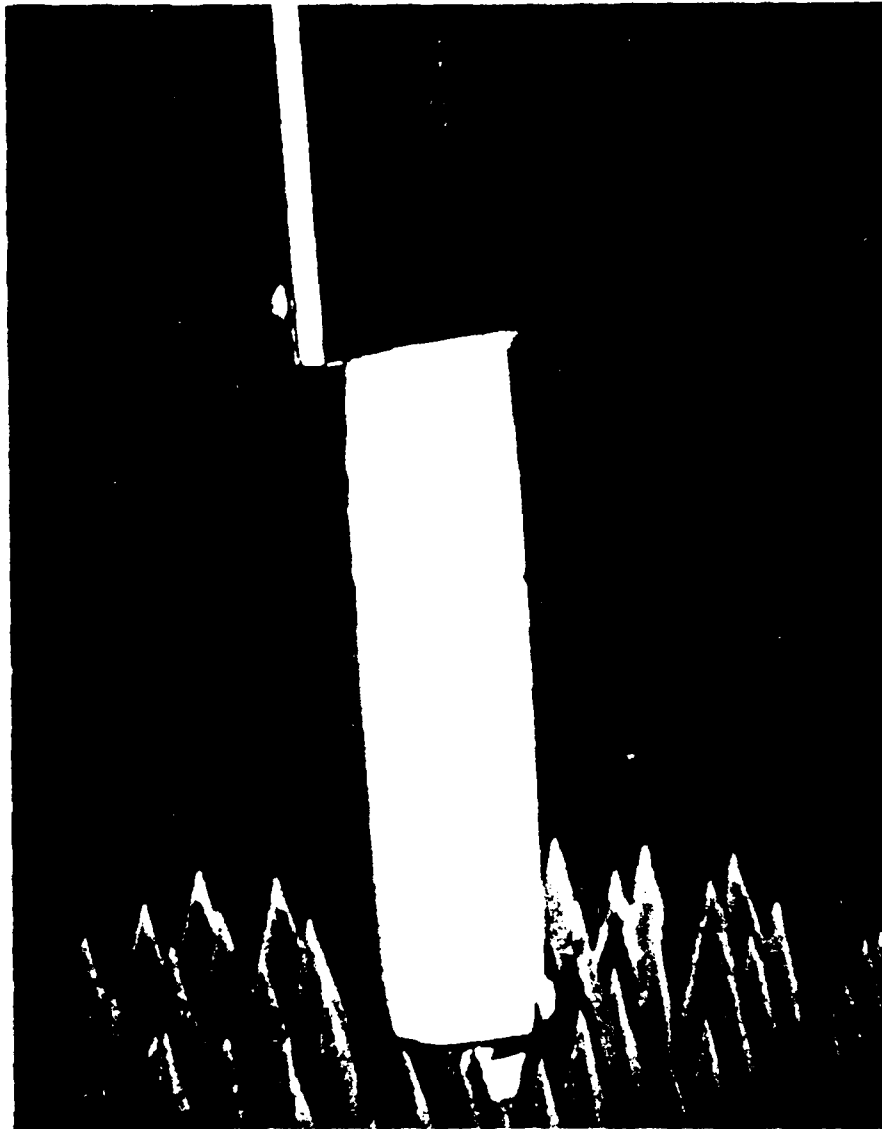Figure 6.3 — Diagram of the RADC bistatic scattering measurement range at Ipswich, MA.

138

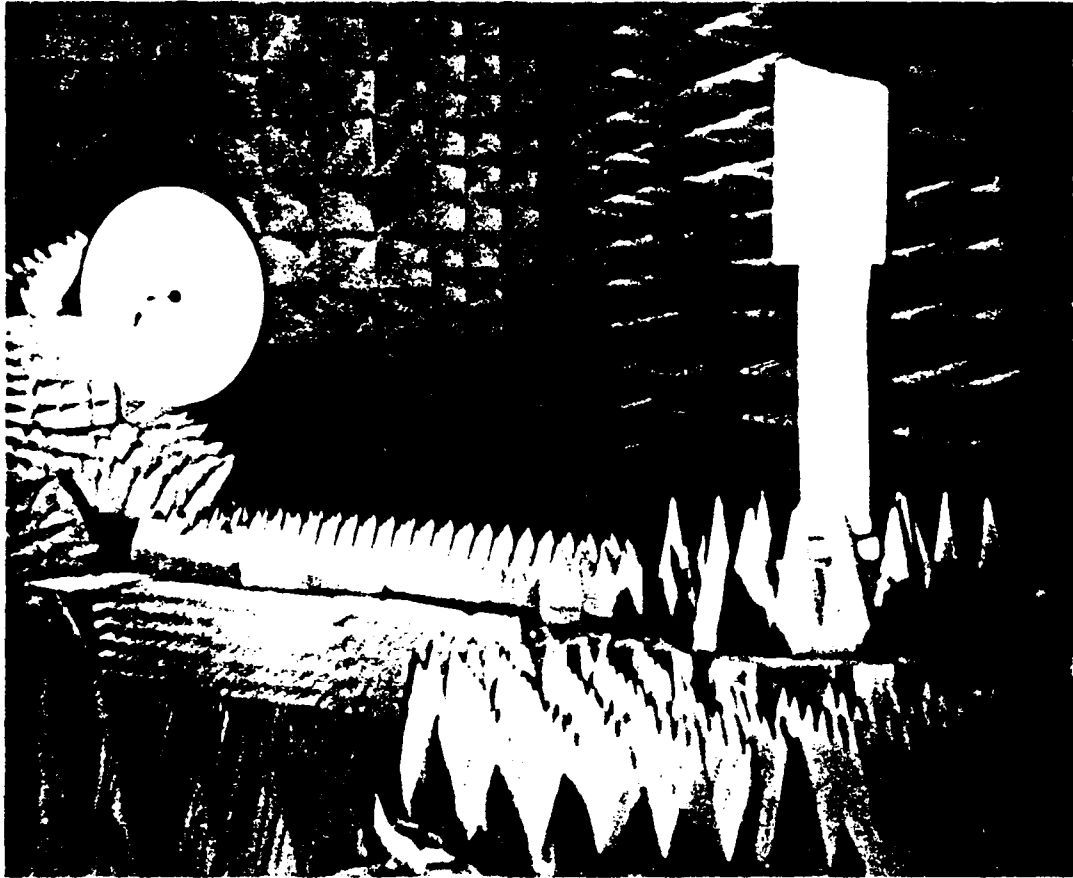Figure 6.4 — Picture of the tapered resistive sheet on top of the styrofoam mount inside the aenochoic chamber

Figure 6.5 — Picture inside of the aenochoic chamber with the transmitting antenna to the left and the resistive sheet on the support to the right.

Figure 6.6 — Photograph of the equipment outside the aenochoic chamber

A theodolite was used to align the targets and set the bistatic scattering angles. The straight edges on the sheets made this process easy. First, the theodolite was made level with the ground. Then, the test object was examined through the viewing scope to see if it was aligned both edge-on and at normal incidence. Alignment was corrected by either repositioning the sheet on the styrofoam support or placing small styrofoam wedges under the styrofoam support.

The theodolite was also used to set the bistatic scattering angle. Since the target and transmitting antenna rotated together while the receiving antenna is stationary, the angle of incidence is measured between the target and the boom. The mount could be rotated independent of the boom to get the desired bistatic angle.

One final alignment was the polarization of the waveguide feed to the parabolic transmitting dish. This was done by setting a level on the waveguide and turning the waveguide until the desired side was parallel to the ground. The alignment was checked with the theodolite.

6.2.2 Transmitting Antenna

The transmitting antenna is a 2 foot parabolic dish. This means that the test object is not in the far field[9] of the antenna when the frequency is 3 GHz. The test object is 16 inches square, and the separation distance is 105 inches. The $\frac{2D^2}{\lambda}$ distance in this case is 128 inches.

A parabolic dish was used instead of a smaller horn because the dish has a much smaller beamwidth. The smaller beam width reduces the coupling between the transmitting antenna and the receiving antenna. Increasing the antenna size also increases the distance to the far field. The trade-off fell in favor of the larger antenna. Violating the far field criterion in this case may be viewed as a correlated quadratic phase error across the test object. This type of error manifests itself in the far field by filling in nulls close to the main beam.

6.2.3 Frequency Selection

The measurements were done at 3.029GHz for several reasons. First, the strip is 4λ wide, which is the same size as the theoretical results presented in the previous chapters.

---

[9] The accepted far field definition is $\frac{2D^2}{\lambda}$ for most objects. It assumes an approximately constant amplitude variation and a 22.5^o phase variation across the test object. This criterion is not strict enough for test objects with low sidelobes, though

Second, errors such as bumps in the sheets and far field separation between the target and antennas are less of a problem at S band than at X band, for example. Third, the measurement range was already configured for S band measurements. Fourth, 3 GHz was the center frequency of the equipment in use. Finally, at this frequency, the target was almost in the far field of the transmitting antenna.

6.2.4 Experimental Procedure

The metal, substrate, and tapered resistive sheets were measured for two bistatic angles of incidence, $30°$ and $90°$, and two polarizations, E and H. It seemed easiest to measure all the targets at H-polarization first, then measure them again at E-polarization. The sequence for each target went as follows:

1. Mount the target on the styrofoam support and place the target and support on the mount.

2. Use the theodolite to align the target and the bistatic angle of incidence at $90°$.

3. Take the measurement of the sheet, support, and background and record the data.

4. Use the theodolite to align the target and the bistatic angle of incidence at $30°$.

5. Take the measurement of the sheet, support, and background and record the data.

6. Remove the target.

7. Take the measurement of the background and support and record the data.

8. Use the theodolite to align the styrofoam support to a bistatic angle of incidence at $90°$.

9. Take the measurement of the background and support and record the data.

10. Have the computer subtract the corresponding support plus background measurement from the target, support, and background measurement and plot the results.

11. Repeat the process for the next target.

An 8 inch diameter metal sphere was also measured after measuring all the targets at E-polarization. The sphere serves as an extra calibration standard to judge how well the measurements were taken.

Once all the targets were measured, the polarization of the transmitting antenna and receiving horn was switched to E-polarization. Again after measuring the targets at this polarization, the 8 inch sphere was also measured.

6.2.5 Potential Errors in the Measurements

Errors are bound to creep into any experiment. One of the problems with bistatic scattering measurements is the relative infancy of the subject. Backscattering measurements have been done for many years and is a mature area of work, but not so with bistatic measurements. Even recent review information in the literature on scattering measurements contain almost no mention of bistatic scattering measurements [Knott, Shaeffer, and Tuley, 1985; Ulaby,...;and Dybdal, 1987].

Several problems peculiar to bistatic scattering measurements done today are

1. Lack of good target calibration information.

2. Measurements are limited in angular extent because of coupling between the transmitting and receiving antennas.

3. Few bistatic measurement ranges, consequently few published results.

These problems will gradually disappear as research in the area increases.

Some potential errors in the bistatic measurements of the metal and resistive sheets are

1. The resistive strips were not perfectly flat. They were for the most part flat but had a few bumps that were $\leq \frac{1}{4}$ inch high, which is well within the Rayleigh criterion for smoothness [Beckmann and Spizzichino, 1987]

$$\text{bumps} < \frac{\lambda}{8 sin\phi_o} \tag{6.1-2}$$

2. The polarization of the transmitting antenna is only accurate to within $\pm 1^o$.

3. The target was not in the far field of the transmitting antenna.

4. The center of the transmitting antenna was a few inches below the center of the sheets.

5. The metal sheet was not perfectly square and the resistive sheets had to be joined together with tape.

6. Equipment errors.

7. Target alignment errors.

6.3 Comparison of theoretical and experimental results

This section compares the measured bistatic scattering patterns to the theoretical patterns. Although some equipment problems prevent an exact over-lay of the theoretical and measured patterns, the tapered sheet did result in much lower sidelobes then the perfectly conducting sheet.

6.3.1 Calibration

The metal plate has a well known scattering pattern and serves as the calibration target. The theoretical results are plotted to the same dB scale as the experimental results. An error in the experimental measurements caused an $8°$ shift in the data as well as a slight squeezing together of the data points by about 5% . These errors were adjusted for the calibration target, then the same adjustments were used for the tapered resistive sheet.

6.3.2 Matching the Theoretical Strip Results to the Experimental Plate Results

The experimental bistatic scattering measurements were made on square plates whereas the theoretical calculations were done for strips. By keeping the bistatic scattering pattern of interest in the x-y plane, the relative scattering patterns of the plate and strip are the same. A correction factor is needed to match the theoretical and experimental patterns. This factor is obtained through assuming a PO current in the z-direction.

In the x-y plane the bistatic RCS of a plate with an E-polarized incident field is given by

$$\sigma_{Eplate}(\phi) = \lim_{r \to \infty} 4\pi r^2 \left| \frac{E^s(\phi)}{E^i(\phi_o)} \right|^2$$

$$= \lim_{r \to \infty} 4\pi r \left| \frac{\frac{-jkZ_o e^{-jkr}}{4\pi r} \int_{-a}^{a} \int_{-b}^{b} J(x')e^{jkx' \cos \phi} dy' dx'}{E_o e^{jkx \cos \phi_o}} \right|^2 \quad (6.3\text{-}1)$$

where 2a is the width and 2b the length of the sheet. Assuming the current is constant in the z-direction, this formula reduces to

$$\sigma_{Eplate}(\phi) = \frac{k^2}{4\pi} \left| \int_{-a}^{a} \int_{-b}^{b} J(x')e^{jkx' \cos \phi} dy' dx' \right|^2$$

$$= \frac{b^2 k^2}{\pi} \left| \int_{-a}^{a} J(x')e^{jkx' \cos \phi} dx' \right|^2 \quad (6.3\text{-}2)$$

$$= \sigma_{Estrip}(\phi) + 20 \log(b) + 9.03 \text{ dBsm} \quad (6.3\text{-}3)$$

The RCS given by (2.5-4) and (6.3-2) are identical except for a constant.

H-polarization has a similar result

$$\sigma_{Hplate}(\phi) = \frac{b^2 k^2 \sin^2 \phi}{\pi} \left| \int_{-a}^{a} J(x')e^{jkx' \cos \phi} dx' \right|^2 \tag{6.3-4}$$

$$= \sigma_{Hstrip}(\phi) + 20 \log(b) + 9.03 \text{ dBsm} \tag{6.3-5}$$

In the x-y plane, the bistatic RCS of a plate is found by multiplying the RCS of a strip by $\frac{4b^2 k}{\pi}$.

6.3.1 Theory vs. Experiment

The adjustments mentioned in 6.3.1 are applied to the experimental data, then the experimental data is overlayed on the theoretical results shown in the following figures.

Figure 6.7 shows the experimental and theoretical bistatic patterns from a 4λ by 4λ metal plate at 3.024 GHz and an E-polarized incident field at an angle of 90°. The experimental and theoretical results agree very well. Figure 6.8 shows the bistatic scattering patterns when the incident field impinges at an angle of 60°. The lobe at 120° is due to reflection and the lobe at 240° is due to forward scattering. H-polarized results for the metal plate appear in Figures 6.9 and 6.10.

Figures 6.11 and 6.12 show the E-polarized and H-polarized bistatic scattering patterns of the tapered resistive sheet when the field is incident at 90°. The theoretical and experimental curves align well at the main beam, but the sidelobes differ by 5 dB or more. Differences in the sidelobe level occur because of several factors. First, the mounting and construction of the sheet induces unwanted errors. The metal tape running down the center of the sheet and wrinkles in the sheet add small errors, but can be enough to affect the low sidelobes. Second, even though the sheet alignment was done with a theodolite, so some error in alignment of the sheet impacts the sidelobe level. Third, background subtraction becomes more difficult for low sidelobes, since the low sidelobes are closer to the scattering levels of the background. Fourth, coupling between the transmitting and receiving antennas plays a more critical role in the sidelobe region. Notice how the oscillations in all the experimental patterns increase from left to right (from receiving and transmitting antennas facing the same way to receiving and transmitting antennas facing each other). The
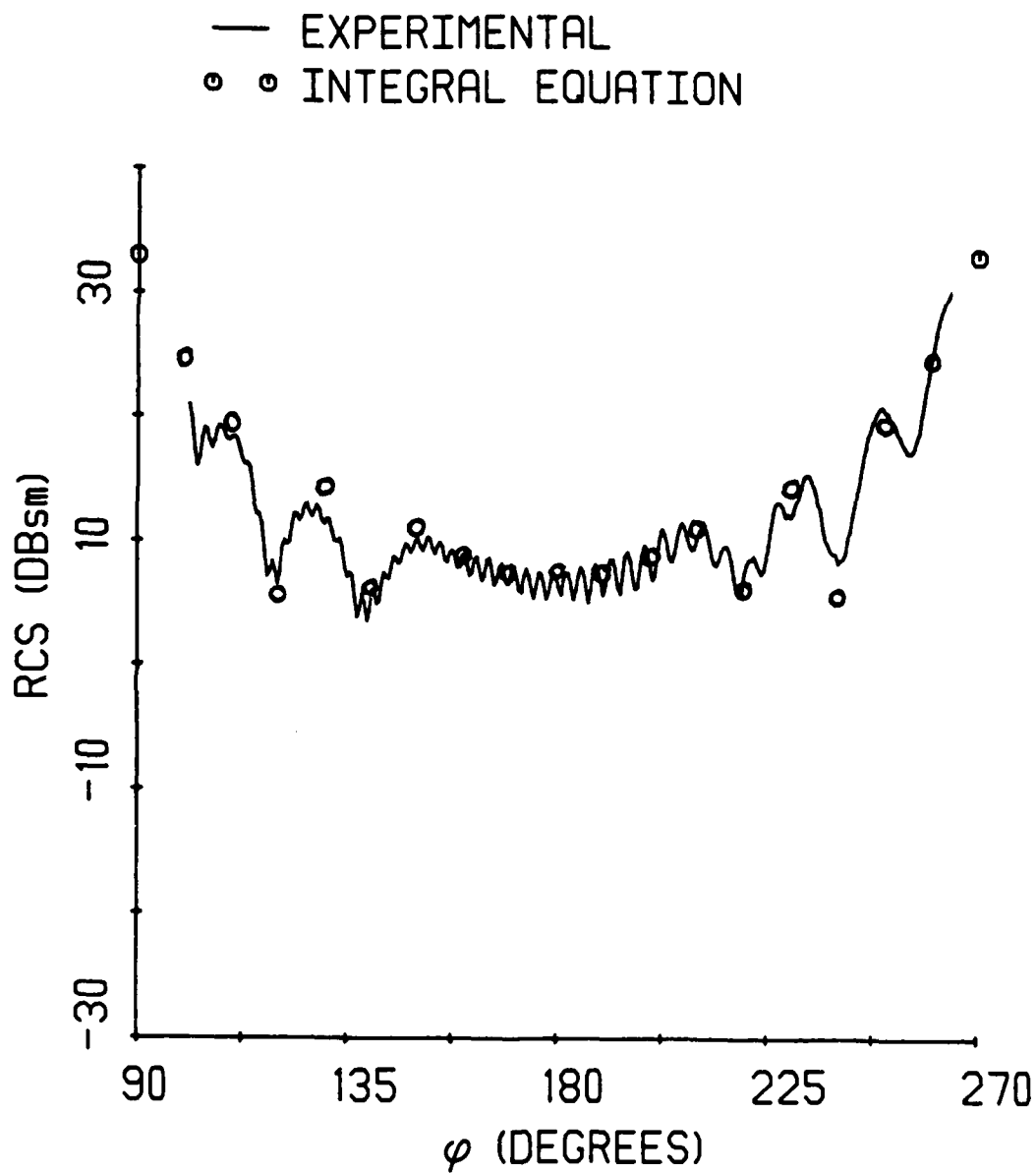
Figure 6.7 — Comparison of the experimental and theoretical bistatic scattering patterns from a 4λ by 4λ metal plate due to an E-polarized wave incident at 90°.

Figure 6.8 — Comparison of the experimental and theoretical bistatic scattering patterns from a 4λ by 4λ metal plate due to an E-polarized wave incident at 60°.
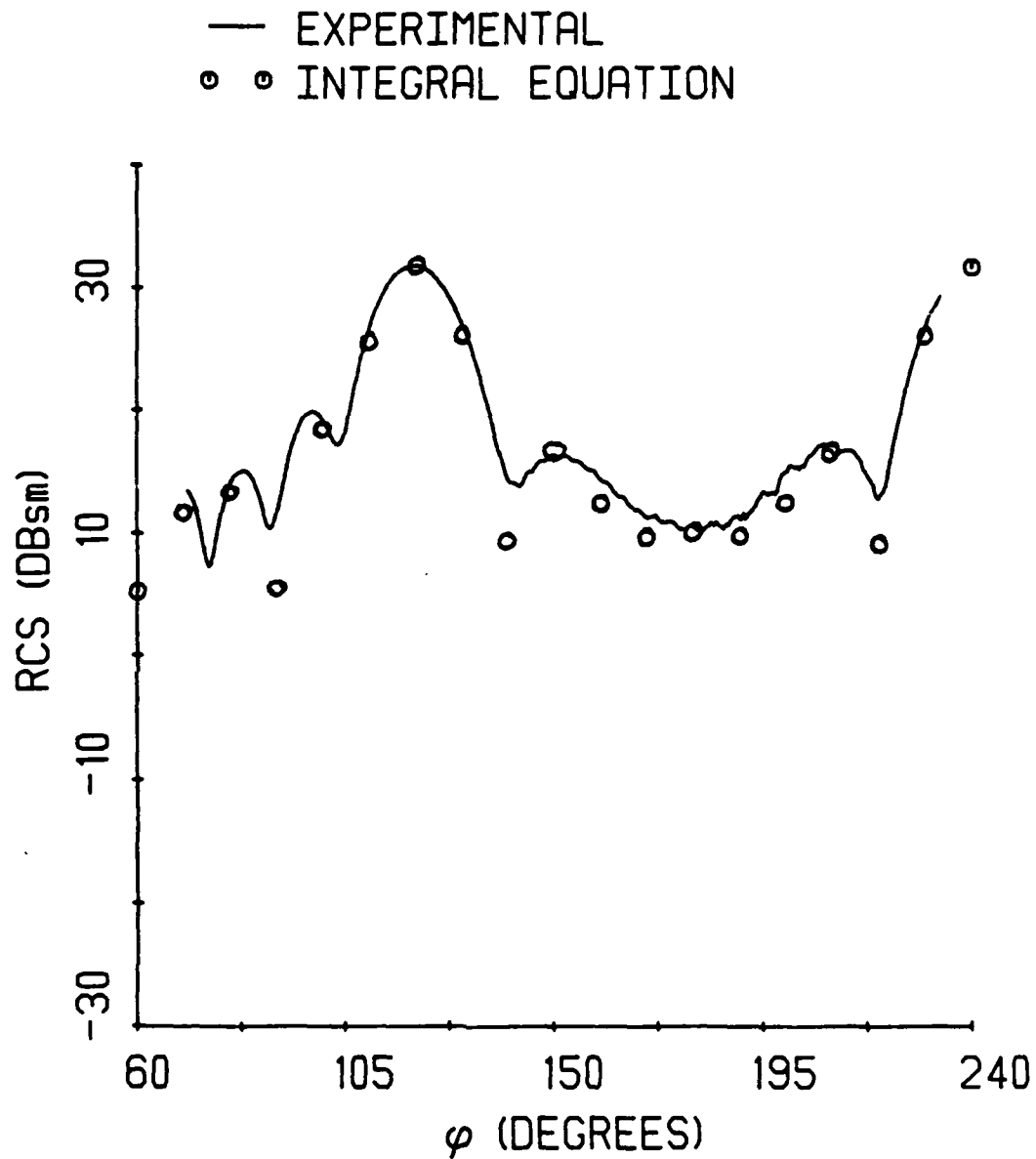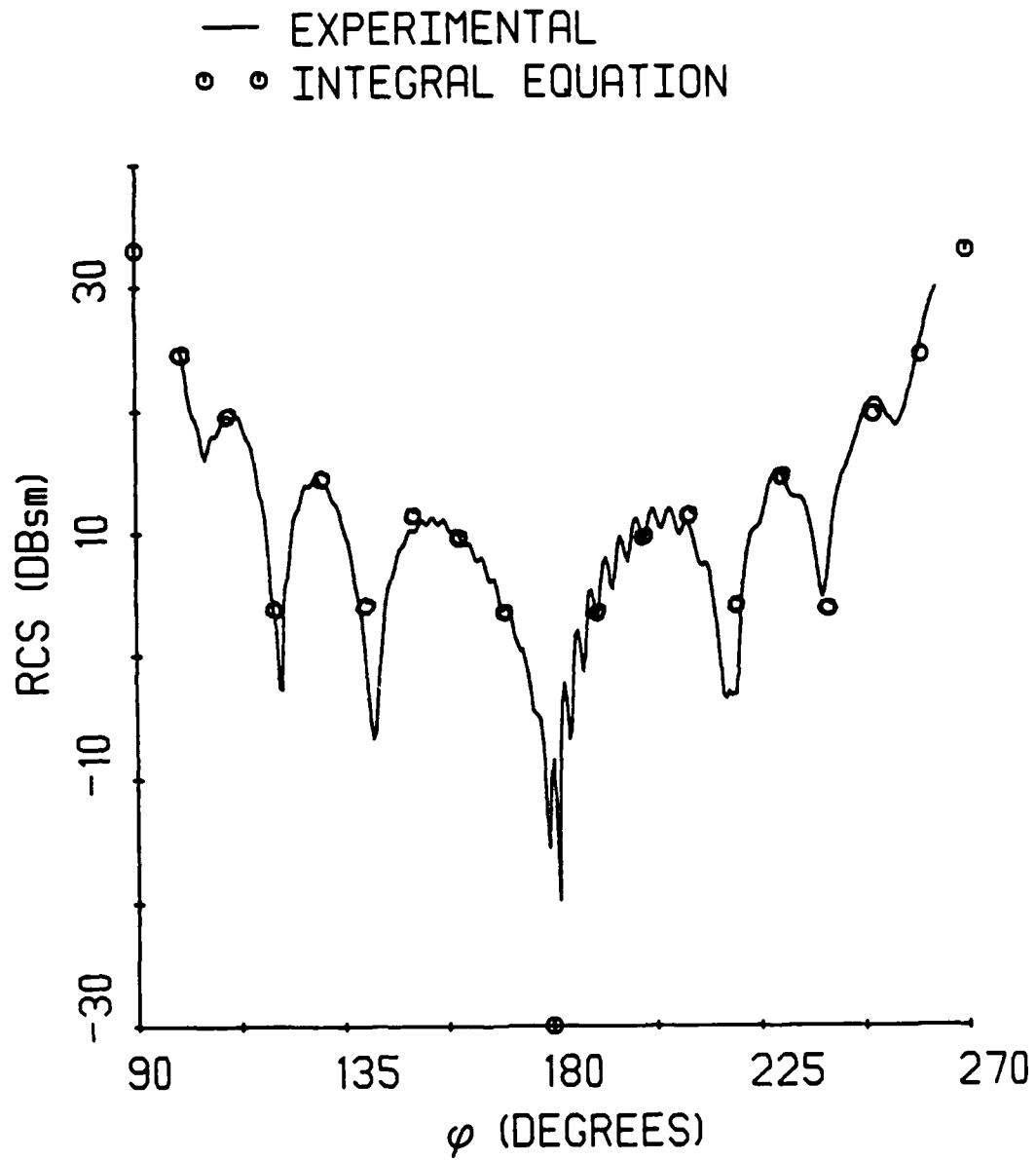
Figure 6.9 — Comparison of the experimental and theoretical bistatic scattering patterns from a 4λ by 4λ metal plate due to an H-polarized wave incident at $90°$.

Figure 6.10 — Comparison of the experimental and theoretical bistatic scattering patterns from a 4λ by 4λ metal plate due to an H-polarized wave incident at 60°.

Figure 6.11 — Comparison of the experimental and theoretical bistatic scattering patterns from a 4λ by 4λ tapered resistive sheet due to an E-polarized wave incident at 90°.

Figure 6.12 — Comparison of the experimental and theoretical bistatic scattering patterns from a 4λ by 4λ tapered resistive sheet due to an H-polarized wave incident at 90°.
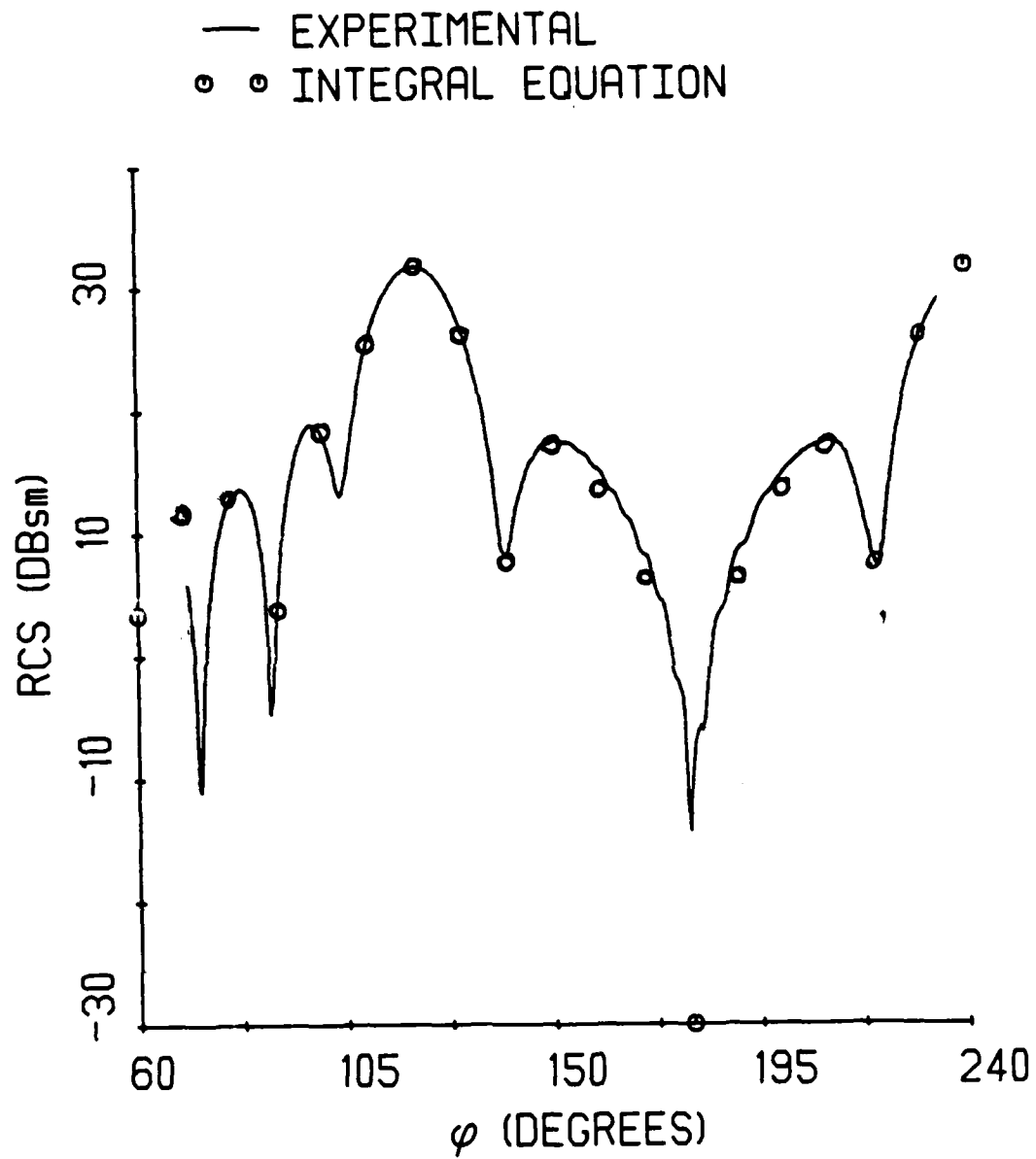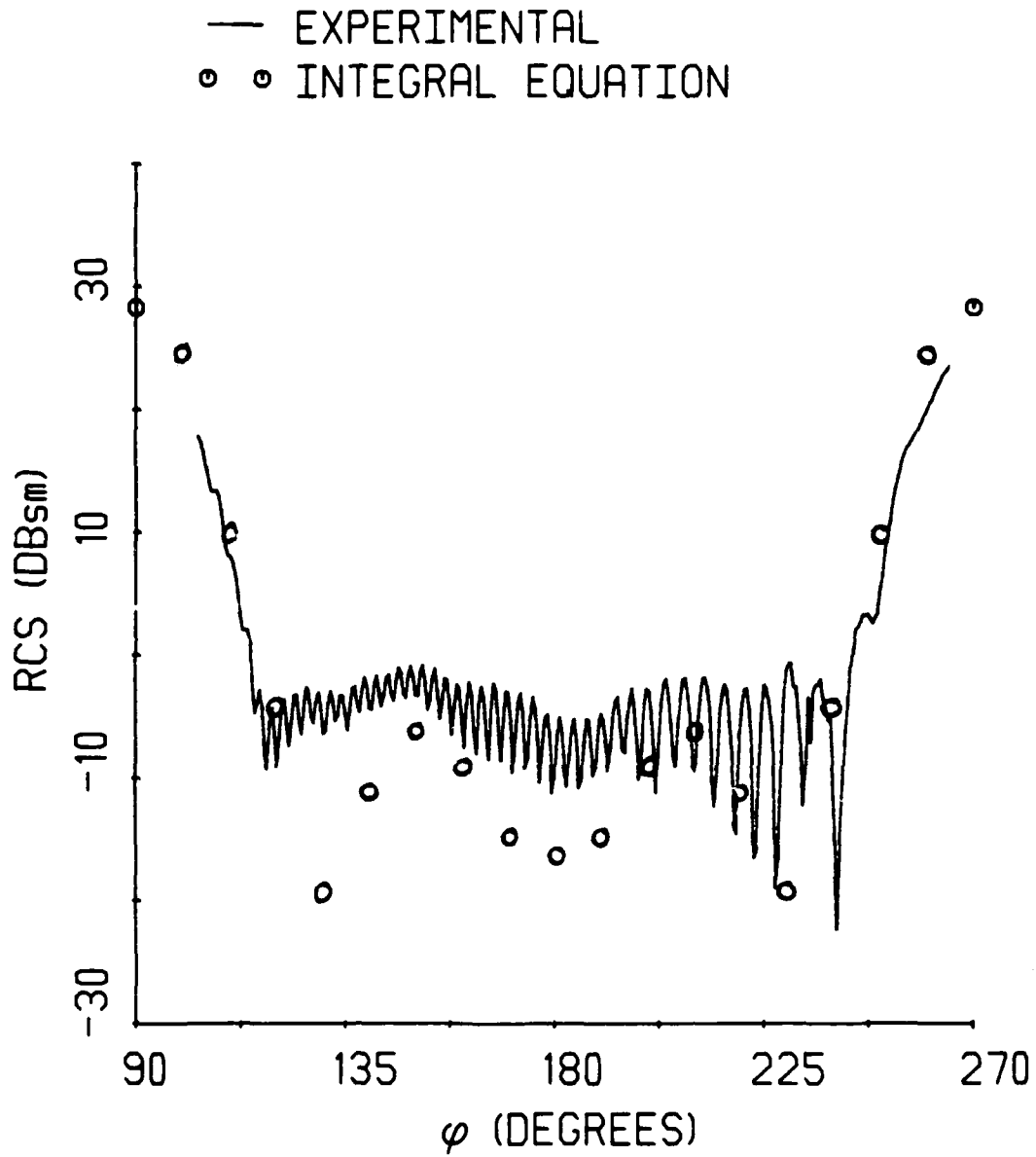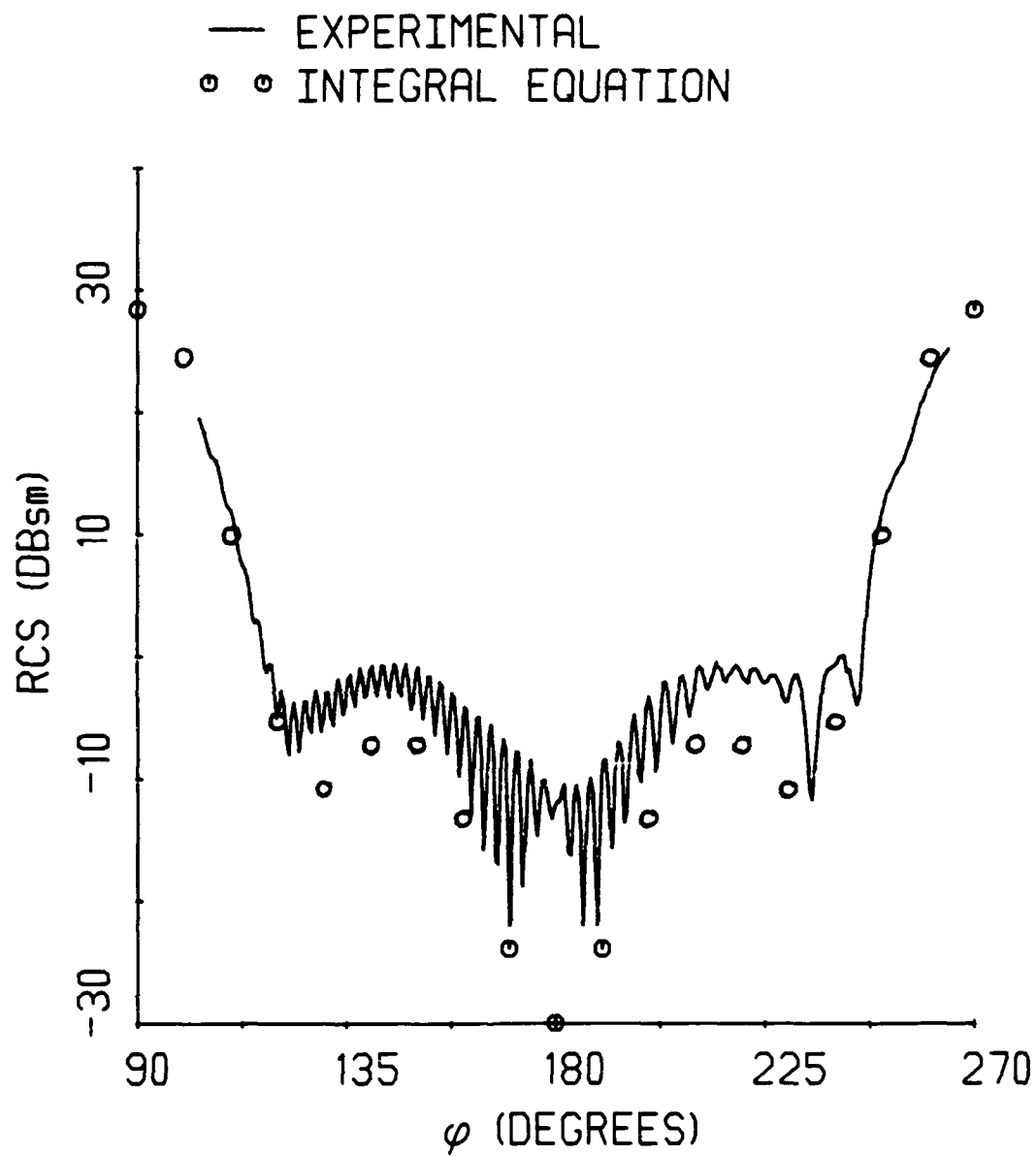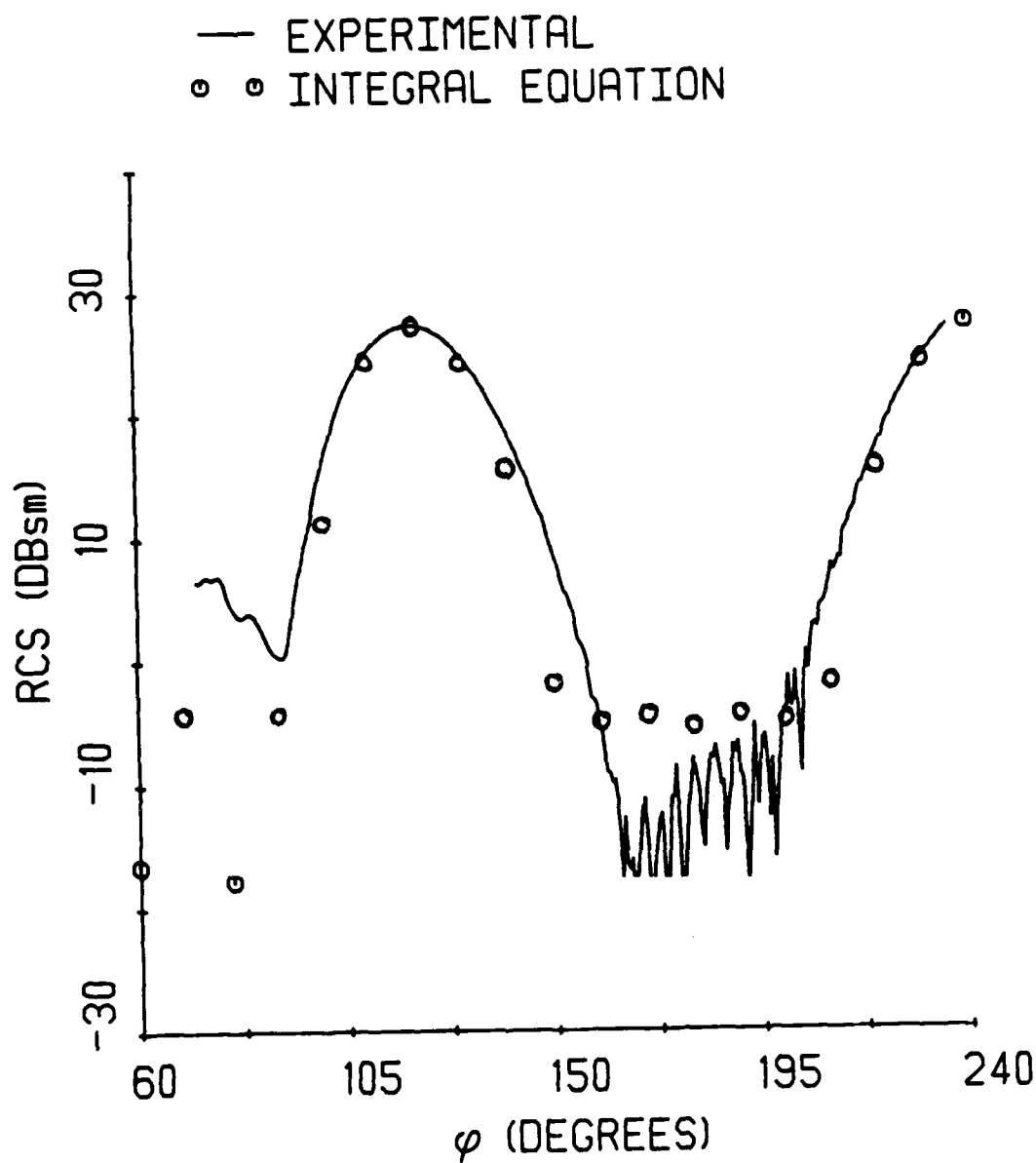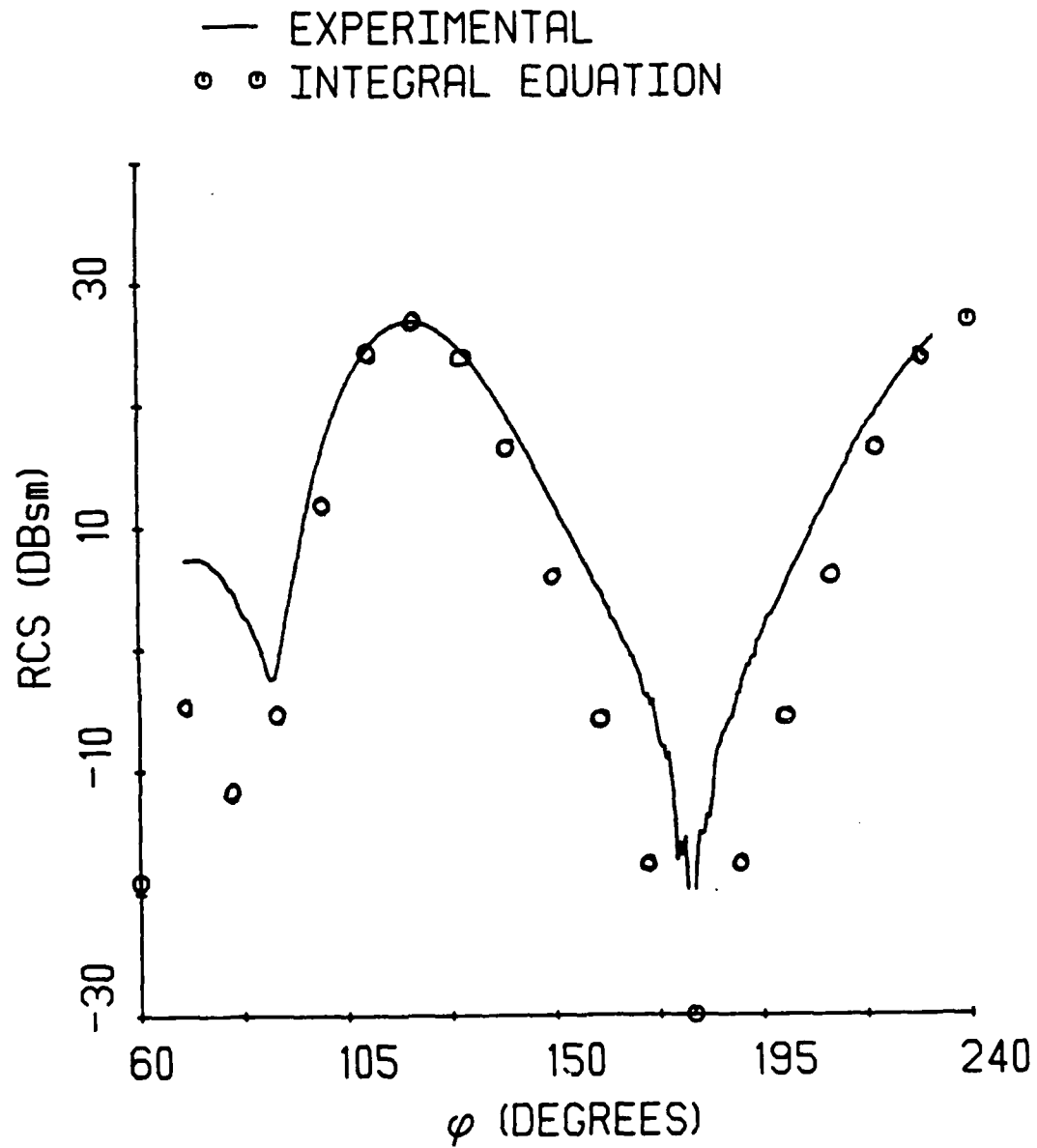
Figure 6.13 — Comparison of the experimental and theoretical bistatic scattering patterns from a 4λ by 4λ tapered resistive sheet due to an E-polarized wave incident at $60°$.

Figure 6.14 — Comparison of the experimental and theoretical bistatic scattering patterns from a 4λ by 4λ tapered resistive sheet due to an H-polarized wave incident at 60°.

oscillations are due to coupling between the receiving and transmitting antennas and are especially dominant in the low sidelobe regions. Fifth, manufacturing errors in the resistive sheet cause the theoretical taper to differ from the actual taper. Chapter IV discusses some of the potential resistive measurement errors. Errors also occur in the metal deposition process. Sixth, the bulging of the scattering mainbeams of the resistive sheet may be due in part to the small separation distance between the transmitting and receiving antennas. A smaller antenna would alleviate this problem, but would also contribute more to the coupling problem, because the smaller antenna has a broader beamwidth.

Figures 6.13 and 6.14 show the E-polarized and H-polarized bistatic scattering patterns of the tapered resistive sheet when the field is incident at 60°. The agreement between theory and experiment is worse for a 60° incidence angle. The theoretical sidelobe level near 65° is about 10 dB lower than the measured sidelobe level. Both the H-polarized theoretical and experimental patterns show a deep null at 180°. On the other hand, the E-polarized theoretical sidelobes are 10 dB higher than the experimental ones between 165° and 205°.

The experimental results from the tapered sheet do show a reduction in the sidelobe level. Better results are possible if some of the errors mentioned above are reduced.

CHAPTER VII

CONCLUSIONS

This thesis examines ways of eliciting a desired scattering response from a strip by tapering the surface resistivity on the strip.

7.1 Summary

Both the theoretical and experimental models of the strip consist of a very thin deposit of metal on a substrate with a dielectric constant close to that of free space. A resistive taper is formed by varying the amount of metal deposited at different positions on the strip. Some of the techniques require a complex resistive taper. In other words both the dielectric constant of the substrate and the conductivity of the metal layer vary with position.

Two methods of calculating the surface current density and scattering patterns of the strip are PO and integral equation approaches. The integral equation approach results are more accurate, but more difficult to calculate than the PO results. Collocation with pulse basis functions forms a system of linear equations that are solved via PLU decomposition and backsubstitution, iteration, and conjugate gradient. The higher the resistivity, the fewer collocation points are necessary for an accurate solution. Since PO gives excellent results for resistive strips, it is used as a seed for the iterative methods. Unfortunately, it did not speed convergence and PLU decomposition and backsubstitution proved the most efficient method of solving the linear system of equations.

In the past, controlling scattering patterns of strips consisted of iterating between varying the resistive taper and looking at the scattering patterns until an acceptable taper was found. A more efficient way to get the desired response is to synthesize a resistive taper in

one step. This can be done by solving the PO and integral equations for the surface resistivity in terms of the surface current density. By substituting a current with a known far field response (e.g. low sidelobe antenna current taper) into the equations, a resistive taper can be found that gives the desired response. The integral equation synthesis technique gives a complex taper, while PO gives a real valued taper. Both tapers yield the desired low sidelobe response when calculating the scattering patterns with the integral equation approach. A real valued taper is preferred, so the PO approach is best.

It is also possible to synthesize a resistive taper that places nulls in the bistatic and backscattering patterns of a resistive strip. The resistive taper derived for nulling is complex and the nulls are much more sensitive to variations in the resistive taper. Consequently, the integral equation synthesis technique is used instead of the PO synthesis technique.

The dc surface resistivity of a sheet may be measured with a four point probe. This technique inserts a current into the resistive sheet via two probes and measures the voltage drop between two other probes. The surface resistivity is calculated with an analytical expression that uses the current, voltage drop, and a correction factor that takes the probe spacing and size of sheet into account. The correction factor assumes the surface resistivity is constant throughout the sheet and the measurement is done in the center of the sheet Measuring a resistive taper on a strip clearly violates both these assumptions. The impact of the taper and proximity of the edges is taken into account by numerically solving a partial differential equation for the voltage induced on the sheet.

It was not practical to build or buy a sheet with a resistive taper that gives rise to a desired low sidelobe current distribution. Southwall Technologies donated a tapered resistive sheet with a parabolic resistive taper across its width. Bistatic scattering patterns of the tapered sheet and a metal plate of the same size were measured at the RADC Ipswich measurement range and compared with theoretical results. The tapered sheet produced low sidelobes in the scattering pattern that agree very well with the theoretical results.

The building of the tapered resistive sheet has errors that keep the experimental and theoretical results from agreeing exactly. Errors in the resistive taper may be characterized as being either random or correlated. The errors cause the average sidelobe level of the desired pattern to go up. These errors and their impact can be statistically analyzed to

determine the tolerances necessary to manufacture a resistive taper for a given sidelobe level.

7.2 Future Work

This thesis only begins to adress the topic of controlling scattering patterns via the synthesis of a resistive taper. More complex shapes and impedance tapers are logical next steps. Also, the theoretical work on the measurement of a resistive taper needs to be expanded and looked at experimentally. Lack of facilities precluded the measurement of the backscattering patterns of the tapered resistive strip. It would be interesting to compare the theoretical and experimental results for backscattering. Other topics include multiple nulls in backscattering patterns, experimentally verifying the error theory, and better first guesses for the iterative methods.

BIBLIOGRAPHY

158

BIBLIOGRAPHY

M. Abramowitz and I.A. Stegen, Handbook of Mathematical Functions. Dover Publications, Inc., NY, 1972.

R.L. Burden and J.D. Faires, Numerical Analysis. Prindle, Weber, and Schmidt, Boston, 1985.

P. Beckmann and A. Spizzichino, The Scattering of Electromagnetic Waves from Rough Surfaces, Artech House, Inc., Norwood, MA, 1987.

W.M. Boerner, "Polarization utilization in electromagnetic inverse scattering" from Inverse Scattering Problems in Optics, Chapt. 7, Springer-Verlog, 1972.

J.P. Boyd, "Orthogonal rational functions on a semi-infinite interval," Journal of Computational Physics, Vol. 70, No. 1, May 1987, pp. 63-88.

E. Brookner, "Antenna array fundamentals," taken from course notes from Microwave Journal Intensive Course, Practical Phased-Array Systems, 1975.

O.M. Bucci and G. Franceschetti, "Rim loaded reflector antennas," IEEE Trans. Ant., Vol. AP-28, No. 3, May 1980, pp 297-305.

C.M. Butler, "General solutions of the narrow strip (and slot) integral equations," IEEE Trans. Ant. Prop., Vol. AP-33, No. 10, Oct 85, pp. 1085-1089.

B.R. Chawla, "RESIST: a time sharing computer program for designing diffused resistors," Proceedings of the IEEE, Jan 1972, pp. 151-152.

B.R. Chawla, "A boundary technique for calculation of distributed resistance," IEEE Trans Electron Devices, Vol. ED-17, No. 10, Oct 1970, pp. 915-925.

K.M. Chen and V.V. Liepa, "The minimization of the back scattering of a cylinder by central loading," IEEE Trans. Ant., Vol. AP-12, Sep 64 ,pp.576-582.

R.E. Collin and F.J. Zucker, Antenna Theory, Part I, McGraw Hill: New York, 1969.

R.B. Dybdal, "Radar Cross Section Measurements," Proc. IEEE, vol. 75, No. 4, Apr 1987, pp 498-516.

R.S. Elliot, Antenna Theory and Design. Prentice-Hall, Inc.: Englewood, NJ, 1981a.

R.S. Elliot, "Array pattern synthesis," IEEE Ant. Prop. Soc. Newsletter, Vol. 27, No. 5, Oct 85, pp. 5-9.

M. ElRayes, "Microwave dielectric spectrum of vegetation," Ph.D. dissertation, The University of Kansas, 1987.

J.H. Ferziger, Numerical Methods for Engineering Application, New York: John Wiley and Sons, 1981.

R.F. Harrington, Field Computation by Moment Methods, Malaber, FL: Robert E. Krieger Publishing Co., 1968.

R.F. Harrington and J.R. Mautz, "Control of radar scattering by reactive loading," IEEE Trans. Ant. Prop., Vol. AP-20, No. 5, Jul 1972, pp. 446-454.

R.F. Harrington and J.R. Mautz, "An impedance sheet approximation for thin dielectric shells," IEEE Trans. Ant. Prop., Vol. AP-20, No. 5, Jul 1975, pp. 531-534.

R.L. Haupt, "Reducing grating lobes due to subarray amplitude tapering," IEEE Trans. Ant. Prop., Vol. AP-33, No. 8, Aug 1985, pp. 846-850.

R.L. Haupt, "The validity of approximating currents on a resistive strip using physical optics," IEEE 1986 AP-S Int. Symp., pp. 137-140.

R.L. Haupt, "Specifying scattering sidelobes for a resistive strip," IEEE 1987 AP-S Int. Symp., pp. 137-140.

E.F. Knott, J.F. Shaeffer, and M.T. Tuley, Radar Cross Section. Artech House, Inc. Dedham, MA, 1985.

R.J. Mailloux, "Phased array theory and technology," Proc. IEEE, Vol. 70, No. 3, Mar 1982, pp. 246-291.

R.J. Mailloux, "Array grating lobes due to periodic phase, amplitude, and time delay quantization," Trans. Ant. Prop. Vol. AP-32, No.12, Dec 1984, pp. 1364-1368.

P.M.Morse and Feshback, Methods of Theoretical Physics, New York: McGraw Hill, 1953.

C.E. Pearson Handbook of Applied Mathematics, New York: Van Nostrand Reinhold Co., 1983.

L. Peters Jr., "End-fire echo area of long, thin bodies," IRE Trans Ant Prop, Vol AP-6, Jan 1958, pp 133-134.

S. Ray and R. Mittra, "Scattering from resistive strips and from metallic strips with resistive edge loading," IEEE 1983 AP-S International Symposium Digest, pp. 603-606.

J.H. Richmond, "Scattering by thin dielectric strips," IEEE Trans. Ant. Prop., Vol. AP-33, No. 1, Jan 1985, pp. 64-68.

J.H. Richmond, "Scattering by a dielectric of arbitrary cross section shape," IEEE Trans. Ant. Prop., Vol. AP-13, No.3 , May 1965, pp. 334-341.

J. Ruze, "Antenna tolerance theory - a review," Proc. IEEE, Vol. 54, No. 4, Apr 1966, pp. 633-640.

T.K. Sarkar and E. Arvas, "On a class of finite step iterative methods (conjugate directions) for the solution of an operator equation arising in electromagnetics," Vol. AP-33, No. 10, Oct 1985, pp. 1058-1066.

T.K. Sarkar, E. Arvas, and S.M. Rao, "Application of FFT and the conjugate gradient method for the solution of electromagnetic radiation from electrically large and small conducting bodies," IEEE Trans. Ant., Vol. AP-34, No. 5, May 1986, pp. 635-639.

J.K. Schindler, R.B. Mack, and P. Blacksmith, Jr., "The control of electromagnetic scattering by impedance loading," Procedings IEEE, Vol. 57, Aug 65, pp.993-1004.

T.B.A. Senior and V.V. Liepa, "Backscattering from tapered resistive strips," IEEE Trans. Ant. Prop., Vol. AP-32, No. 7, July 1984, pp. 747-751.

T.B.A. Senior, "Scattering by resistive strips," Radio Science, Vol. 14, No. 5, Sep-Oct 1979, pp. 911-924.

T.B.A. Senior, "Backscattering from resistive strips," IEEE Trans. Ant. Prop., Vol. AP-27, No. 6, Nov 1979, pp. 808-813,.

R.A. Shore and H. Steyskal, "Nulling in linear array patterns with minimization of weight perturbations," RADC-TR-82-32, (AD-A118695), Feb 1982.

F.M. Smits, "Measurement of sheet resistivities with the four-point probe," Bell System Technical Journal, Vol. 34, No. 1, May 1958, pp. 711-718.

M.A. Stuchly, M.M. Brady, S.S. Stuchly, and G. Gajda, "Equivalent circuit of an open-ended coaxial line in a lossy dielectric," IEEE Trans. Inst. and Meas., Vol. IM-31, No. 2, Jun 1982, pp. 116-119.

W.L. Stutzman and G.A. Thiele, Antenna Theory and Design, John Wiley and Sons: NY, 1981.

T.T. Taylor, "Design of line-source antennas for narrow beamwidth and low sidelobe," IRE Trans. Ant. Prop., Vol. AP-3, No. 1, 1955, pp. 16-28.

A Uhlir, Jr., "The potentials of infinite systems of sources and numerical solutions of problems in semiconductor engineering," Bell System Technical Journal, Vol. 34, No. 1 Jan 1955, pp. 105-128.

F.T. Ulaby, R.K. Moore, and A.K. Fung, Microwave Remote Sensing: Active and Passive, Vol II, Addison-Wesley Publishing Co., Reading, MA, 1982.

L.B. Valdes, "Effect of electrode spacing on the equivalent base resistance of point-contact transisters," Proceedings of the IRE, Vol.40, No. 11, 1952, pp. 1429-1434.

L.B. Valdes, "Resistivity measurements on germanium for transistors," Proceedings of the IRE, Vol. 42, No. 12, Feb 1984, pp. 420-427.

J. Walker, "The secret of a microwave oven's rapid cooking action is disclosed," Scientific American, Vol. 256, No. 2, Feb 1987, pp 134-138.

R.W. Wang, "Reduction of the edge diffraction of a circular ground plane using resistive edge loading," Ph.D. dissertation, The University of Michigan, 1985.

R.W. Wang and V.V. Liepa, "Reduction of the edge diffraction of a circular gound plane by using resistive edge loading," IEEE AP-S International Symposium Digest, 1985, pp. 769-771.

E. Yazgan "The radiation pattern of a surface loaded ellipsoidal reflector," IEEE Trans. Ant., Vol. AP-35, No. 3, Mar 1987, pp.347-349.

END

DATE
FILMED

9-88

DTIC